Article

# The type 2 cytokine Fc–IL-4 revitalizes exhausted CD8$^+$ T cells against cancer

https://doi.org/10.1038/s41586-024-07962-4

Received: 29 May 2023

Accepted: 20 August 2024

Published online: 25 September 2024

Open access

Check for updates

Bing Feng[1,2,11], Zhiliang Bai[3,11], Xiaolei Zhou[1,2], Yang Zhao[1], Yu-Qing Xie[1], Xinyi Huang[4], Yang Liu[1], Tom Enbar[1], Rongrong Li[1], Yi Wang[1,2], Min Gao[1], Lucia Bonati[1], Mei-Wen Peng[1], Weilin Li[1], Bo Tao[5], Mélanie Charmoy[6], Werner Held[6], J. Joseph Melenhorst[7], Rong Fan[3,5]✉, Yugang Guo[1,2,8,9,10]✉ & Li Tang[1,2]✉

Current cancer immunotherapy predominately focuses on eliciting type 1 immune responses fighting cancer; however, long-term complete remission remains uncommon[1,2]. A pivotal question arises as to whether type 2 immunity can be orchestrated alongside type 1-centric immunotherapy to achieve enduring response against cancer[3,4]. Here we show that an interleukin-4 fusion protein (Fc–IL-4), a typical type 2 cytokine, directly acts on CD8$^+$ T cells and enriches functional terminally exhausted CD8$^+$ T (CD8$^+$ $T_{TE}$) cells in the tumour. Consequently, Fc–IL-4 enhances antitumour efficacy of type 1 immunity-centric adoptive T cell transfer or immune checkpoint blockade therapies and induces durable remission across several syngeneic and xenograft tumour models. Mechanistically, we discovered that Fc–IL-4 signals through both signal transducer and activator of transcription 6 (STAT6) and mammalian target of rapamycin (mTOR) pathways, augmenting the glycolytic metabolism and the nicotinamide adenine dinucleotide (NAD) concentration of CD8$^+$ $T_{TE}$ cells in a lactate dehydrogenase A-dependent manner. The metabolic modulation mediated by Fc–IL-4 is indispensable for reinvigorating intratumoural CD8$^+$ $T_{TE}$ cells. These findings underscore Fc–IL-4 as a potent type 2 cytokine-based immunotherapy that synergizes effectively with type 1 immunity to elicit long-lasting responses against cancer. Our study not only sheds light on the synergy between these two types of immune responses, but also unveils an innovative strategy for advancing next-generation cancer immunotherapy by integrating type 2 immune factors.

Current cancer immunotherapy, exemplified by immune checkpoint blockade (ICB) and adoptive T cell transfer (ACT) therapies, primarily relies on inducing type 1 immunity to eliminate cancer cells. Despite the remarkable clinical success, the emergence of resistance and relapse suggests that boosting type 1 immunity alone may not be sufficient to elicit durable antitumour effects in most patients[5]. The absence of sustained response is partly attributed to the phenomenon whereby cancer-reactive T cells undergo exhaustion, ultimately becoming fully dysfunctional and failing to control cancer progression[6]. On chronic antigen stimulation, cancer-reactive CD8$^+$ T cells progressively differentiate into terminally exhausted (TCF-1$^-$TIM-3$^+$) CD8$^+$ T (CD8$^+$ $T_{TE}$) cells, a subset of T cells derived from progenitor exhausted (TCF-1$^+$TIM-3$^-$) CD8$^+$ T cells[7–9]. CD8$^+$ $T_{TE}$ cells possess greater cytotoxicity than the progenitor exhausted T cells and directly contribute to elimination of cancer cells[10]. However, these cells show survival deficiency and impaired proliferative capacity[11]. The challenge lies in maintaining this population of cells within the tumour microenvironment (TME) and preserving their effector function, as they show limited responsiveness to current immunotherapies[7–9,12,13].

In addition to the well-established role of type 1 immunity, recent findings suggest a beneficial character of type 2 immunity in promoting antitumour effects. T helper 2 ($T_H2$)-cell-mediated antitumour immunity has been shown to lead to the containment of cancer at the tissue level by remodelling blood vasculature and inducing cancer cell hypoxia and death[14]. Furthermore, the functionality of $T_H2$ cells, rather than $T_H1$ cells, within the infusion product of anti-CD19 chimeric antigen receptor (CAR)-T cells demonstrates a strong and positive correlation with ultra-long-term event-free survival (longer than 54 months) in patients with acute lymphoblastic leukaemia who were treated with CAR-T cell therapy[4]. Despite these insights, the exploration of whether and how type 1 and 2 immunity can be orchestrated for durable antitumour responses remains largely uncharted.

[1]Institute of Bioengineering, École Polytechnique Fédérale de Lausanne (EPFL), Lausanne, Switzerland. [2]Institute of Materials Science and Engineering, EPFL, Lausanne, Switzerland. [3]Department of Biomedical Engineering, Yale University, New Haven, CT, USA. [4]Institute of Chemical Sciences and Engineering, EPFL, Lausanne, Switzerland. [5]Department of Pathology, Yale University School of Medicine, New Haven, CT, USA. [6]Department of Oncology, University of Lausanne, Epalinges, Switzerland. [7]Lerner Research Institute, Cleveland Clinic, Cleveland, OH, USA. [8]State Key Laboratory of Advanced Drug Delivery and Release Systems, Zhejiang University, Hangzhou, China. [9]Jinhua Institute of Zhejiang University, Jinhua, China. [10]Present address: Institute of Drug Metabolism and Pharmaceutical Analysis, College of Pharmaceutical Sciences, Zhejiang University, Hangzhou, China. [11]These authors contributed equally: Bing Feng, Zhiliang Bai. ✉e-mail: rong.fan@yale.edu; yugang.guo@zju.edu.cn; li.tang@epfl.ch

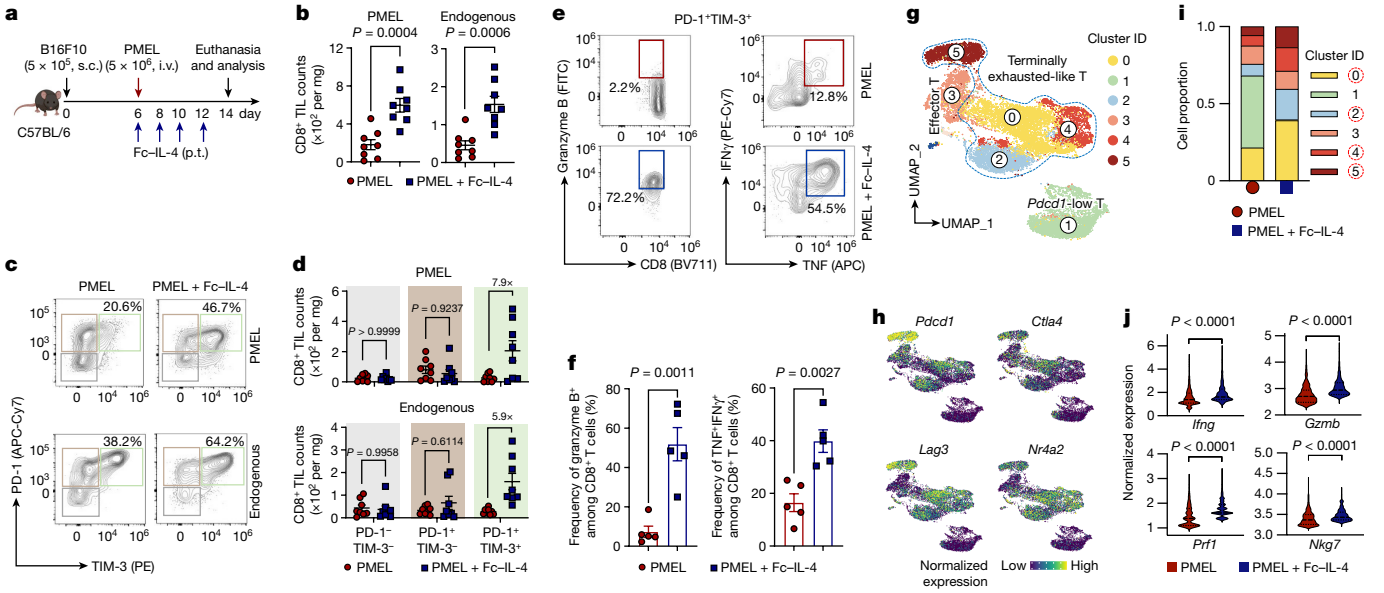


**Fig. 1 | Fc–IL-4 enriches functional CD8$^+$ $T_{TE}$ cells in the TME. a–f**, C57BL/6 mice bearing B16F10 tumours received ACT of PMEL T cells ($5 \times 10^6$, i.v.) followed by administration of Fc–IL-4 (20 μg, p.t.) or PBS every other day for four doses. Mice were euthanized on day 14 and the tumour tissues were collected for analysis by flow cytometry. Data are a single representative of two independent experiments. All data represent mean ± s.e.m. Shown are the experimental timeline (**a**), cell counts of PMEL or endogenous CD8$^+$ TILs (**b**) ($n = 8$ animals), representative flow cytometry plots showing the frequencies of tumour-infiltrating CD8$^+$ $T_{TE}$ cells (PD-1$^+$TIM-3$^+$) among PMEL or endogenous CD8$^+$ TILs (**c**), cell counts of three subpopulations among PMEL or endogenous CD8$^+$ TILs (**d**) ($n = 8$ animals), and representative flow cytometry plots (**e**) and frequencies (**f**) of granzyme B$^+$ and TNF$^+$IFNγ$^+$ among tumour-infiltrating CD8$^+$ $T_{TE}$ cells ($n = 5$ animals). **g–j**, C57BL/6 mice bearing B16F10 tumours received ACT of PMEL T cells ($5 \times 10^6$, i.v.) followed by administration of Fc–IL-4 (20 μg, p.t.) or PBS every other day for four doses in total. Mice were euthanized on day 14, tumour tissues were collected, and PMEL CD8$^+$ T cells were sorted for scRNA-seq ($n = 5$ animals). **g**, UMAP clustering of all the PMEL CD8$^+$ TILs. **h**, Indicated co-inhibitory gene marker expression on the UMAP. **i**, Comparison of cell proportion in each cluster. **j**, Comparison of functional gene expression in the terminally exhausted-like T cells. Statistical analyses are performed using two-sided unpaired Student's *t*-test. Schematic in **a** created using BioRender (https://Biorender.com).

## Fc–IL-4 enriches functional CD8$^+$ $T_{TE}$ cells

Interleukin-4 (IL-4), a prototypical type 2 cytokine, has been reported to prolong the survival of T and B lymphocytes[15,16]. Here we proposed that IL-4 could rejuvenate the tumour-infiltrating exhausted T cells for enhanced cancer immunotherapy. We first produced a recombinant fusion protein combining mouse IL-4 with mutant IgG2a Fc (Fc–IL-4), which showed comparable bioactivity to native IL-4 while greatly extending its circulating half-life (Extended Data Fig. 1a–e). To investigate the effects of Fc–IL-4 on intratumoural antigen-specific CD8$^+$ T cells, we intravenously (i.v.) transferred in vitro-activated PMEL T cells ($5 \times 10^6$), which recognize the gp100 tumour antigen, to mice bearing subcutaneous (s.c.) B16F10 melanoma tumours in combination with peritumoural (p.t.) administration of Fc–IL-4 or phosphate-buffered saline (PBS) as a control (Fig. 1a). Before transfer, the PMEL T cells showed an explicitly type 1 signature (Extended Data Fig. 1f). We found that combining type 1-centric ACT therapy and Fc–IL-4 markedly promoted CD45.2$^+$ immune cell infiltration into the TME compared to ACT alone (Extended Data Fig. 1g). Among the many tumour-infiltrating immune cells, the counts of CD8$^+$ T cells, including both transferred PMEL and endogenous T cells, showed the most prominent augmentation (Fig. 1b and Extended Data Fig. 1g).

By phenotyping the CD8$^+$ tumour-infiltrating lymphocytes (TILs), we discovered that the PD-1$^+$TIM-3$^+$ subset, identified as $T_{TE}$ cells (TCF-1$^-$TIM-3$^+$)[9,12], but not the other subsets, was substantially enriched (Fig. 1c and Extended Data Fig. 2a,b). Cell counts of the PD-1$^+$TIM-3$^+$ subset within the adoptively transferred PMEL and endogenous CD8$^+$ T cells were increased by 7.9- and 5.9-fold, respectively, in the combination therapy compared to ACT alone (Fig. 1d). Treatment with Fc–IL-4 also boosted the production of granzyme B, a pivotal cytotoxic molecule, and enhanced the polyfunctionality of both transferred and endogenous CD8$^+$ $T_{TE}$ cells (Fig. 1e,f and Extended Data Fig. 2c). To examine the antigen-dependency of TIL expansion induced by Fc–IL-4, mice were cotransferred with naive PMEL and OT1 (recognizing ovalbumin (OVA) antigen) T cells, followed by the challenge with B16F10 tumours without OVA antigen (Extended Data Fig. 2d). Only the antigen-specific PMEL CD8$^+$ $T_{TE}$ cells were expanded by Fc–IL-4 (Extended Data Fig. 2e–g), suggesting that Fc–IL-4 acts on CD8$^+$ $T_{TE}$ cells in an antigen-dependent manner. Fc–IL-4 had a negligible effect on induction of type 2 polarization in CD4$^+$ or CD8$^+$ T cells (Extended Data Fig. 2h–j).

To explore whether Fc–IL-4 alters the transcriptomic profiles of TILs, single-cell RNA sequencing (scRNA-seq) was performed on sorted tumour antigen-specific Thy1.1$^+$CD8$^+$ TILs from B16F10 tumours treated with ACT in combination with Fc–IL-4 or PBS control (Extended Data Fig. 3a). Integrated and unsupervised clustering of 15,983 single cells from the two conditions resolved six transcriptionally distinct clusters, showing negligible batch effect (Fig. 1g and Extended Data Fig. 3b). Despite intrinsic heterogeneities presented in these clusters (Extended Data Fig. 3c), cells in clusters 0, 2, 4 and 5 expressed high levels of co-inhibitory markers, including *Pdcd1*, *Ctla4*, *Lag3* and *Nr4a2*, indicating their intratumoural $T_{TE}$ signature (Fig. 1h). By contrast, cluster 1 cells showed attenuated expression of these exhaustion markers. The cell proportion of the Fc–IL-4 group in these clusters enriched in terminally exhausted-like cells (clusters 0, 2, 4 and 5) was found to be notably higher than that of PBS group, whereas the proportion in cluster 1 was extremely low, suggesting the increased $T_{TE}$ cells in the TME attributable to the Fc–IL-4 effects (Fig. 1i). Consistent with the flow cytometry results, *Ifng* and *Gzmb* expression were significantly higher in Fc–IL-4-treated cells, in addition to *Prf1* and *Nkg7* (Fig. 1j). The $T_{TE}$ cells in the Fc–IL-4 group also showed a significantly elevated expression of many functional modules including type 1 cytokines,

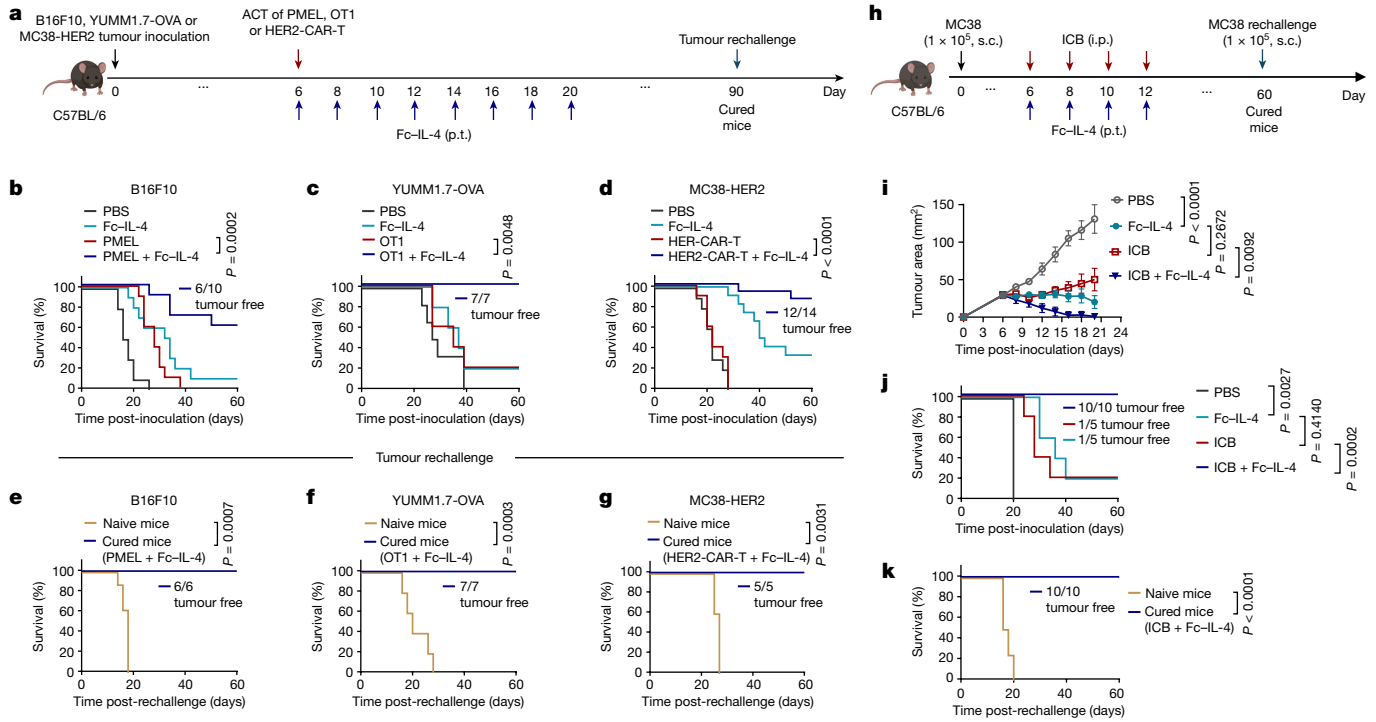


**Fig. 2 | Fc–IL-4 potentiates ACT and ICB immunotherapies for tumour clearance and durable protection in many syngeneic models. a–g**, C56BL/6 mice were inoculated (s.c.) with B16F10 ($5 \times 10^5$), YUMM1.7-OVA ($1 \times 10^6$) or MC38-HER2 ($5 \times 10^5$) cells and treated with ACT of activated PMEL T cells, OT1 T cells or HER2-CAR-T cells ($5 \times 10^6$, i.v.), respectively, on day 6 followed by administration of Fc–IL-4 (20 μg, p.t.) or PBS every other day for eight doses, or Fc–IL-4 alone. Cured mice receiving the combination treatment were rechallenged (s.c.) with B16F10 ($1 \times 10^5$), YUMM1.7-OVA ($5 \times 10^5$) or MC38-HER2 ($1 \times 10^5$) cells on day 90. Shown are the experimental timeline (**a**); Kaplan–Meier survival curves of mice bearing B16F10 (**b**) ($n = 10$ animals), YUMM1.7-OVA (**c**) ($n = 7$ animals) or MC38-HER2 (**d**) ($n = 14$ animals) tumours; and survival curves of naive or cured mice rechallenged with B16F10 (**e**) ($n = 6$ animals), YUMM1.7-OVA (**f**) ($n = 7$ animals) or MC38-HER2 (**g**) ($n = 5$ animals) cells. **h–k**, C56BL/6 mice were inoculated with MC38 cells ($1 \times 10^5$, s.c.) and received the combination treatment of ICB (anti-PD-1 (100 μg, i.p.) plus anti-CTLA-4 (100 μg, i.p.)) and Fc–IL-4 (20 μg, p.t.) every other day for four doses ($n = 10$ animals). Mice receiving injections of PBS, Fc–IL-4 or ICB only served as controls ($n = 5$ animals). Cured mice receiving the combination treatment were rechallenged with MC38 cells ($1 \times 10^5$, s.c.) on day 60. Shown are experimental timeline (**h**), average tumour growth curves (**i**) and Kaplan–Meier survival curves (**j**) of tumour-bearing mice, and survival curves of naive or cured mice that were rechallenged (**k**) ($n = 10$ animals). Data are pooled from two independent experiments. All data represent mean ± s.e.m. and are analysed by log-rank test (**b–g**, **j** and **k**) or one-way ANOVA and Tukey's test (**i**). Schematics in **a**,**h** created using BioRender (https://Biorender.com).

cytotoxicity and granzymes (Extended Data Fig. 3d). Collectively, these findings substantiate the idea that Fc–IL-4 selectively amplifies the $CD8^+$ $T_{TE}$ cell population while enhancing their effector function in the TME.

## Fc–IL-4 enhances type 1 immunotherapies

We next investigated whether Fc–IL-4 as a type 2 cytokine could enhance the antitumour efficacy of type 1-centric ACT and ICB therapies against solid tumours (Fig. 2). In the B16F10 mouse melanoma model (Fig. 2a), ACT of PMEL T cells ($5 \times 10^6$) alone modestly suppressed tumour growth without any curative responses. By contrast, combination treatment of ACT of PMEL T cells and Fc–IL-4 completely eradicated established tumours, leading to durable cures in 60% of tumour-bearing mice without lymphodepletion preconditioning (Fig. 2b and Extended Data Fig. 4a,b). Moreover, all mice with tumours cleared by the combination therapy further rejected a rechallenge with the identical B16F10 tumour cells 70 days post-treatment (Fig. 2e and Extended Data Fig. 4h), indicating a lasting antitumour memory effect. To further assess the robustness of this combinatory strategy, we established an OVA-expressing mouse melanoma model, YUMM1.7-OVA, with a high tumour burden (area greater than 40 $mm^2$ or volume greater than 100 $mm^3$) before the treatment. Co-administration of Fc–IL-4 and OVA-specific OT1 T cells resulted in complete tumour eradication and durable cures in 100% of the tumour-bearing mice, whereas treatments with Fc–IL-4 or ACT alone achieved only limited tumour reduction (Fig. 2c and Extended Data Fig. 4c,d). As in the B16F10 model, 100% of cured mice by combination therapy rejected the secondary challenge of YUMM1.7-OVA cells (Fig. 2f and Extended Data Fig. 4i).

We next extended this combinatory strategy to CAR-T cell therapy in a s.c. mouse MC38 colon adenocarcinoma model that expressed human epidermal growth factor receptor 2 (HER2) (Fig. 2a). ACT of HER2-targeting mouse CAR-T (HER2-CAR-T) cells alone (Extended Data Fig. 4e) failed to induce tumour regression (Fig. 2d), consistent with the clinical challenge of CAR-T cell therapy against solid tumours. By contrast, ACT using CAR-T cells adjuvanted by Fc–IL-4 led to remarkable tumour clearance with eventually a curative response rate of 86% (Fig. 2d). Notably, administration of Fc–IL-4 alone effectively inhibited tumour progression and cleared roughly 33% tumours (Fig. 2d and Extended Data Fig. 4f,g), suggesting that Fc–IL-4 also acted on endogenous T cells for enhanced antitumour immunity. Mice cured by the combination therapy rejected subsequent rechallenge of MC38-HER2 tumour cells completely (Fig. 2g and Extended Data Fig. 4j) and, to a partial extent, parental MC38 tumour cells without a HER2 antigen (Extended Data Fig. 4k–m), suggesting the induction of immune memory in both transferred and endogenous T cells (Extended Data Fig. 4n).

Lymphodepletion preconditioning was deemed unnecessary for the combination therapy of ACT and Fc–IL-4 to achieve curative responses, therefore excluding the potential toxic effects associated

with lymphodepletion. Fc–IL-4 demonstrated a highly favourable safety profile without any overt toxicities in all treated mice receiving Fc–IL-4 alone or combination therapies (Extended Data Fig. 4o–q).

We also assessed the therapeutic efficacy of combining Fc–IL-4 with ICB therapy in the s.c. MC38 model (Fig. 2h). Whereas ICB therapy using anti-PD-1 plus anti-CLTA-4 antibodies achieved modest tumour suppression, the co-administration of Fc–IL-4 and ICB led to robust and enduring clearance of established tumours in all treated mice, without notable toxicities (Fig. 2i,j and Extended Data Fig. 4r). All mice cured by the combined treatment of Fc–IL-4 and ICB rejected the second challenge of MC38 tumour cells (Fig. 2k), underscoring the potency of Fc–IL-4 as an adjuvant agent for substantially bolstering ICB therapy.

Expanding beyond mouse tumour models, we proceeded to investigate the translational potential of a human version of Fc–IL-4 (hu.Fc–IL-4) in augmenting the efficacy of CD19-targeting human CAR-T (CD19-CAR-T) cells against human cancer (Extended Data Fig. 5a). In an ex vivo coculture assay, hu.Fc–IL-4 markedly enhanced the proliferation, cytotoxicity and effector function of the human CD19-CAR-T cells (Extended Data Fig. 5b–d). In a xenograft model of s.c. Raji lymphoma in immune-deficient Nod Scid Gamma (NSG) mice, CD19-CAR-T cells alone showed transient effects of tumour inhibition, whereas the combination therapy of CD19-CAR-T cells and hu.Fc–IL-4 resulted in complete tumour eradication in 75% of treated mice, leading to prolonged survival (Extended Data Fig. 5e–h). We next established a recurrent leukaemia tumour model by i.v. inoculating Nalm6 human leukaemic cancer cells into NSG mice, followed by a post-treatment rechallenge (Extended Data Fig. 5i). Although the treatment with CD19-CAR-T cells alone eliminated leukaemia cells from the initial inoculation, all surviving mice succumbed to the second challenge and died roughly 2 weeks after rechallenge (Extended Data Fig. 5j,k). By contrast, the combination therapy of hu.Fc–IL-4 and CD19-CAR-T cells not only completely cleared the initially inoculated leukaemia cells, but also conferred resistance to the second challenge, leading to prolonged survival in 80% of treated mice (Extended Data Fig. 5j,k). Notably, the treatment with hu.Fc–IL-4 markedly increased the expansion, effector function and cytotoxicity of CD19-CAR-T cells in the peripheral blood (Extended Data Fig. 5l–n). Taken together, these studies conducted in syngeneic and xenograft tumour models show the promise of Fc–IL-4 as a safe and potent type 2 cytokine therapy in enhancing the antitumour efficacy of ACT and ICB therapies.

## Fc–IL-4 directly acts on CD8$^+$ $T_{TE}$ cells

To determine the specific immune cells contributing to the enhanced efficacy, we selectively depleted CD8$^+$ T cells, CD4$^+$ T cells, natural killer cells or neutrophils and repeated the therapeutic study. The results demonstrated that only the depletion of CD8$^+$ T cells completely abrogated the therapeutic efficacy mediated by the combination therapy of ACT and Fc–IL-4, whereas deficiencies in other immune cells (CD4$^+$ T, natural killer, neutrophils) had negligible effects on the therapeutic outcome (Extended Data Fig. 6a).

To determine which subset of the exhausted CD8$^+$ T cells was responsible for the observed therapeutic effects, we exploited *Tcf7*$^{DTR\text{-}GFP}$ transgenic P14 T cells (where DTR is diphtheria toxin receptor and GPF is green fluorescent protein), which enabled targeted depletion of progenitors (TCF-1$^+$) by in vivo treatment with diphtheria toxin[9]. Mice bearing B16-gp33 tumours underwent lymphodepletion followed by ACT of *Tcf7*$^{DTR\text{-}GFP}$ transgenic P14 T cells (i.v.) recognizing gp33 tumour antigen (Fig. 3a). Selective depletion of progenitor exhausted CD8$^+$ T cells was validated in peripheral blood, tumour-draining lymph nodes and tumour tissues upon diphtheria toxin treatment (Extended Data Fig. 6b–f). Fc–IL-4 treatment notably increased the number of intratumoural CD8$^+$ $T_{TE}$ cells and boosted their effector function even in the absence of progenitor exhausted CD8$^+$ T cells, to the extent comparable to that in the mice without diphtheria toxin treatment (Fig. 3b–d). In the absence of progenitor exhausted cells, the combination therapy of ACT and Fc–IL-4 yielded comparable antitumour efficacy and curative response rates to those observed in mice with complete subsets (Fig. 3e), suggesting that CD8$^+$ $T_{TE}$ cells directly responded to Fc–IL-4 independently of the progenitor exhausted subset for the enhanced efficacy. Furthermore, we sorted ex vivo-induced PD-1$^+$TIM-3$^-$ and PD-1$^+$TIM-3$^+$ CD8$^+$ T cells and separately transferred these subsets into tumour-bearing mice. Consistently, treatment with Fc–IL-4 led to a noticeable enrichment of PMEL CD8$^+$ $T_{TE}$ cells showing enhanced effector function in mice receiving ACT of PD-1$^+$TIM-3$^+$ CD8$^+$ T cells only (Extended Data Fig. 6g,h).

To investigate whether Fc–IL-4 exerts a direct effect on CD8$^+$ T cells, we first measured the expression levels of IL-4 receptor subunit-α (IL-4Rα) and found that CD8$^+$ $T_{TE}$ cells expressed the highest level of IL-4Rα among various subsets (Extended Data Fig. 6i), suggesting Fc–IL-4 might directly signal through IL-4Rα expressed on CD8$^+$ TILs. We next generated IL-4Rα-knockout (KO) OT1 (OT1$^{IL\text{-}4R\alpha\text{-}KO}$) T cells using CRISPR (clustered regularly interspaced short palindromic repeats)–Cas9 gene editing technology (Fig. 3f and Extended Data Fig. 6j) and transferred them to mice bearing B16-OVA tumours following lymphodepletion. In contrast to wild-type (WT) OT1 CD8$^+$ $T_{TE}$ cells, treatment with Fc–IL-4 failed to enrich intratumoural OT1$^{IL\text{-}4R\alpha\text{-}KO}$ CD8$^+$ $T_{TE}$ cells or enhance their cytotoxicity or effector function, leading to substantially attenuated efficacy against B16-OVA tumours (Fig. 3g–j), providing evidence that Fc–IL-4 directly targets tumour-infiltrating CD8$^+$ $T_{TE}$ cells through IL-4Rα signalling.

To explain the mechanisms underlying the enrichment of CD8$^+$ $T_{TE}$ cells by Fc–IL-4, we used FTY720 to block T cell egress from lymphoid organs and found the enrichment of both transferred and endogenous CD8$^+$ $T_{TE}$ cells remained unaffected (Extended Data Fig. 6k), suggesting that Fc–IL-4-mediated enrichment of CD8$^+$ $T_{TE}$ cells within the TME was not attributable to increased recruitment of T cells from peripheral tissues. Furthermore, we found Fc–IL-4 showed negligible effect on the proliferative capacity of CD8$^+$ $T_{TE}$ cells (Extended Data Fig. 6l,m). By contrast, Fc–IL-4 markedly promoted the survival of CD8$^+$ $T_{TE}$ cells with upregulated Bcl-2 expression and mitigated T cell apoptosis (Fig. 3k,l). Using a mouse model with endogenous IL-4 neutralized by anti-IL-4 antibody, we further discovered that endogenous IL-4, typically present at a substantially lower concentration than the exogenously injected Fc–IL-4, had a negligible impact on the antitumour immunity of ACT with PMEL T cells or the expansion and effector function of tumour-infiltrating CD8$^+$ $T_{TE}$ cells (Extended Data Fig. 6n–s). Overall, these findings indicate that the exogenous type 2 cytokine Fc–IL-4 directly drives the enrichment of CD8$^+$ $T_{TE}$ cells primarily through enhancing their survival.

## Fc–IL-4 boosts glycolysis of CD8$^+$ $T_{TE}$ cells

Inspired by the previous report that IL-4 promotes glycolysis of B cells[15], we next examined whether Fc–IL-4 modulates the metabolic activity of CD8$^+$ $T_{TE}$ cells. We observed that Fc–IL-4 markedly elevated the glucose transporter-1 (Glut-1) expression and glucose uptake capacity in ex vivo-induced CD8$^+$ $T_{TE}$ cells, along with increased extracellular lactate level (Extended Data Fig. 7a–e). On T cell receptor (TCR) stimulation using a dimeric anti-CD3 antibody, Fc–IL-4 notably enhanced extracellular acidification rate (ECAR) of CD8$^+$ $T_{TE}$ cells, with elevated basal level, glycolytic capacity and glycolytic reserve (Fig. 4a,b). Fc–IL-4 showed negligible effects on the level of oxidative phosphorylation (Extended Data Fig. 7f,g) and therefore prominently increased the ratios of ECAR to oxygen consumption rate (OCR) (Extended Data Fig. 7h) for reprogrammed metabolism of CD8$^+$ $T_{TE}$ cells towards glycolysis. Furthermore, metabolomic analysis revealed distinctive metabolic profiles in Fc–IL-4-treated CD8$^+$ $T_{TE}$ cells (Extended Data Fig. 7i,j). Treatment with Fc–IL-4 triggered significant alterations in 41 metabolites, including upregulation of three key glycolytic metabolites: glyceraldehyde

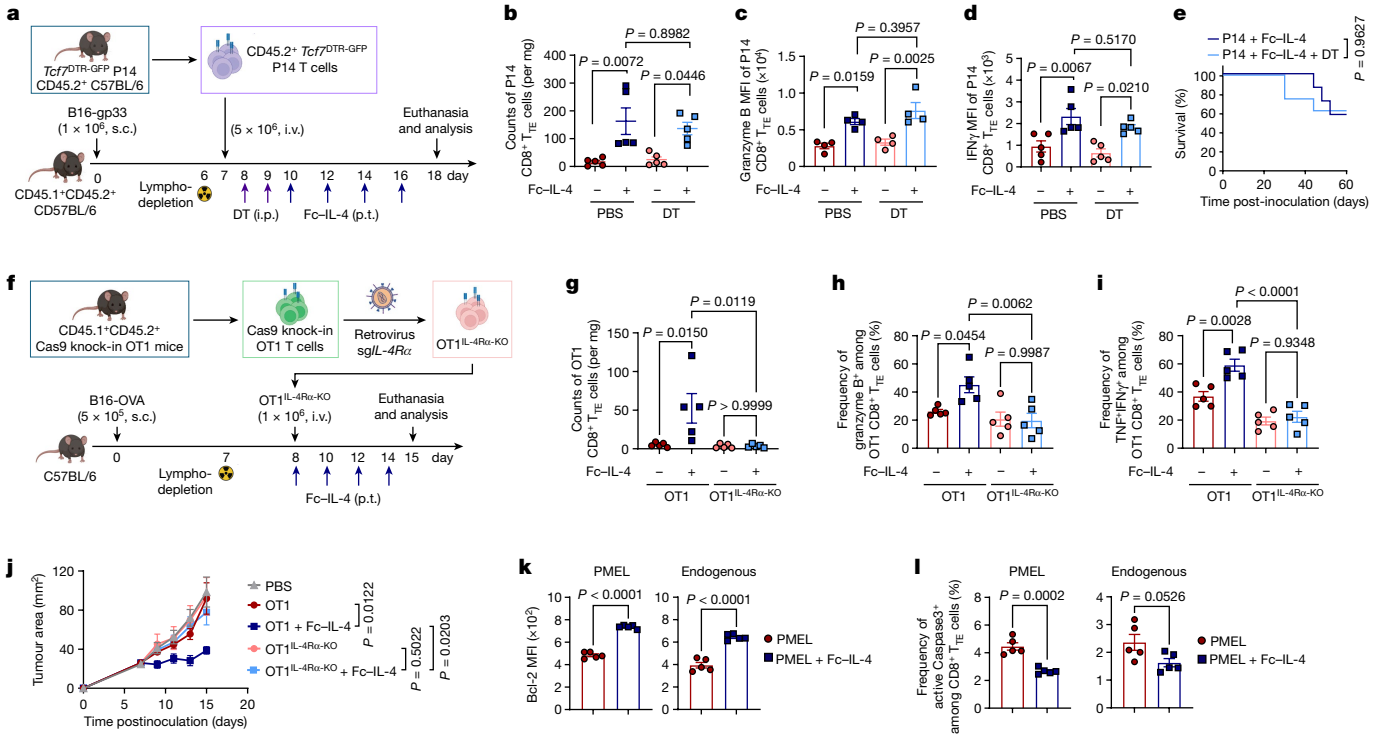


**Fig. 3 | Fc–IL-4 enhances the survival of CD8$^+$ $T_{TE}$ cells directly through IL-4Rα signalling. a**–**e**, CD45.1$^+$CD45.2$^+$ C57BL/6 mice bearing B16-gp33 tumours received ACT of activated CD45.2$^+$ *Tcf7*$^{DTR\text{-}GFP}$ P14 T cells ($5 \times 10^6$, i.v.) 1 day post-lymphodepletion, followed by the injection of diphtheria toxin (DT) (1 µg × 2, i.p.) and subsequent treatment of Fc–IL-4 (20 µg, p.t.) or PBS every other day for four doses. Shown are the experimental timeline (**a**), counts of tumour-infiltrating P14 CD8$^+$ $T_{TE}$ cells (*Tcf7*$^{DTR\text{-}GFP^-}$PD-1$^+$TIM-3$^+$) (**b**) ($n = 5$ animals), mean fluorescence intensity (MFI) of granzyme B (**c**) ($n = 4$ animals) and IFNγ (**d**) ($n = 5$ animals) of tumour-infiltrating P14 CD8$^+$ $T_{TE}$ cells, and Kaplan–Meier survival curves of mice ($n = 8$ animals) (**e**). **f**–**j**, Mice bearing B16-OVA tumours received ACT of activated WT OT1 or OT1$^{IL\text{-}4R\alpha\text{-}KO}$ T cells ($1 \times 10^6$, i.v.) 1 day after lymphodepletion followed by treatment with Fc–IL-4 (20 µg, p.t.) or PBS every other day for four doses ($n = 5$ animals). Shown are the experimental timeline (**f**), counts of tumour-infiltrating OT1 CD8$^+$ $T_{TE}$ cells (**g**), frequencies of granzyme B$^+$ (**h**) and TNF$^+$IFNγ$^+$ (**i**) among tumour-infiltrating OT1 CD8$^+$ $T_{TE}$ cells, and average tumour growth curves (**j**). **k**,**l**, Experimental setting was similar to that described in Fig. 1a except that BrdU (1 mg, i.p.) was injected 24 h before tumour tissue collection ($n = 5$ animals). Shown are Bcl-2 MFI (**k**) and frequencies of active Caspase-3$^+$ cells (**l**) among PMEL and endogenous CD8$^+$ $T_{TE}$ cells. Data are a single representative of two independent experiments. All data represent mean ± s.e.m. and are analysed by one-way ANOVA and Tukey's test (**b**–**d** and **g**–**j**), log-rank test (**e**) or two-sided unpaired Student's *t*-test (**k** and **l**). Schematics in **a**,**f** created using BioRender (https://Biorender.com).

3-phosphate, phosphoenolpyruvate and lactate (Fig. 4c and Extended Data Fig. 7k,l).

To further profile metabolic networks at the transcriptome level, we performed unsupervised single-cell clustering analysis on the basis of the 1,667 genes involved in Kyoto Encyclopedia of Genes and Genomes (KEGG) defining metabolic pathways. Compared to the PBS control group, antigen-specific PMEL T cells treated with Fc–IL-4 showed enrichment in clusters 0, 2 and 3, characterized by abundant expression of the glycolysis–gluconeogenesis gene module (Fig. 4d,e). We conducted a more detailed analysis of gene expression-based carbohydrate activities within the identified metabolic clusters (Extended Data Fig. 7m). These metabolic activities not only demonstrated higher percentages but also showed increased expression levels per single cell in clusters 0, 2 and 3, primarily enriched in the Fc–IL-4-treated group (Fig. 4f). Furthermore, blockade of glycolysis using 2-deoxy-D-glucose (2-DG) completely abrogated the effects of Fc–IL-4 in reinvigorating CD8$^+$ $T_{TE}$ cells (Fig. 4g,h and Extended Data Fig. 7n,o). Altogether, these findings highlight the role of Fc–IL-4 in modulating the metabolism of CD8$^+$ $T_{TE}$ cells by promoting glycolysis, a pivotal process for enriching functional CD8$^+$ $T_{TE}$ cells.

To explain the molecular mechanism driving the heightened glycolysis induced by Fc–IL-4, we next performed single-cell assay for transposase accessible chromatin (ATAC) and transcriptome coprofiling of ex vivo-induced CD8$^+$ $T_{TE}$ cells. Using uniform and high-quality data collected from both IL-4- and PBS-treated groups (Fig. 4i and Extended Data Fig. 8a), coprofiling of ATAC and transcriptome datasets showed distinct molecular profiles in the CD8$^+$ $T_{TE}$ cells between the two conditions, suggesting an intrinsic regulatory impact on this specific cell type treated with IL-4 (Fig. 4j and Extended Data Fig. 8b). Consistently, cells treated with IL-4 showed a considerable augmentation in cytotoxicity and survival markers, evident across both gene expression and chromatin accessibility layers (Extended Data Fig. 8c,d). We next performed a differential motif analysis using ATAC data to identify potential transcription factor binding sites within open chromatin regions. In IL-4-treated CD8$^+$ $T_{TE}$ cells compared to the PBS condition, Stat6 emerged as the most significantly enhanced motif, whereas Forkhead box protein O1 (Foxo1), a canonical negative regulator of mTOR[17,18], showed the highest degree of reduction (Fig. 4j). In addition, analysis of the signalling pathways regulated by differentially expressed genes (DEGs) in CD8$^+$ TILs showed a significant upregulation of mTOR, eIF4 and p70S6K, and PI3K/AKT, along with JAK–STAT signalling, NF-κB activation and glycolysis in mice receiving treatment of Fc–IL-4 as compared to PBS (Fig. 4k). Upstream regulator analysis based on the DEGs identified several functional molecules predicted to be upregulated in the Fc–IL-4 group, particularly NF-κB, Myc, Pi3k, Akt1 and Stat6 (Fig. 4l and Extended Data Fig. 8e), which were found to promote glycolysis[19,20].

Next, we focused on explaining the roles of STAT6 and the PI3K–AKT–mTOR axis in reinvigorating CD8$^+$ $T_{TE}$ cells by Fc–IL-4. Using flow cytometry and western blot analysis, we confirmed an elevation in the

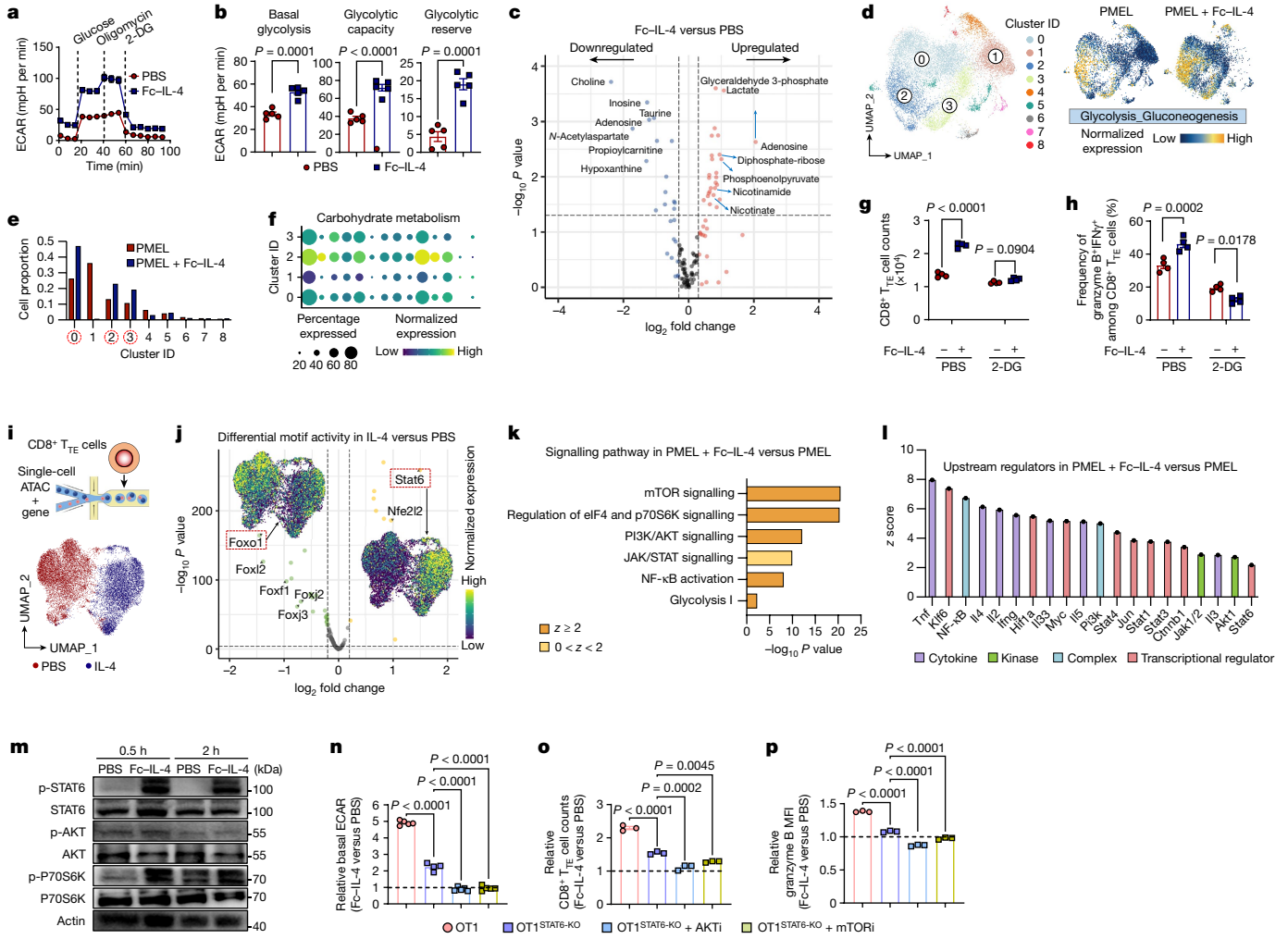


**Fig. 4 | Fc–IL-4 augments glycolytic metabolism of CD8$^+$ $T_{TE}$ cells through STAT6 signalling and PI3K–AKT–mTOR axis. a**,**b**, Real-time ECAR analysis (**a**) and average basal glycolysis, glycolytic capacity and reserve (**b**) of ex vivo-induced CD8$^+$ $T_{TE}$ cells ($n = 5$ biological replicates). mpH, milli-pH. **c**, Volcano plot of altered metabolites in ex vivo-induced CD8$^+$ $T_{TE}$ cells treated with Fc–IL-4 ($n = 4$ biological replicates) versus PBS ($n = 3$ biological replicates). **d**–**f**, Experimental setting as described in Fig. 1g. Shown are unsupervised UMAP clustering of PMEL CD8$^+$ TILs based on the 1,667 genes involved in KEGG-defining metabolic pathways (**d**), cell proportion in each cluster (**e**) and systematic expression comparison of carbohydrate metabolisms among top four clusters (**f**). **g**,**h**, T cell counts (**g**) and frequencies of granzyme B$^+$IFNγ$^+$ (**h**) among ex vivo-induced CD8$^+$ $T_{TE}$ cells with or without 2-DG ($n = 4$ biological replicates). **i**,**j**, Schematic illustration of single-cell ATAC and gene coprofiling of IL-4 versus PBS-treated ex vivo-induced CD8$^+$ $T_{TE}$ cells and a joint ATAC–gene UMAP (**i**), and volcano plot showing differentially active motifs (**j**). **k**,**l**, Experimental setting as described in Fig. 1g. Shown are signalling pathways regulated by DEGs (**k**) and top 20 ranked upstream regulators predicted from DEGs (**l**) in PMEL CD8$^+$ TILs. **m**, Western blot analysis of indicated proteins in ex vivo-induced CD8$^+$ $T_{TE}$ cells ($n = 3$ biological replicates). **n**–**p**, Relative basal glycolysis (**n**) ($n = 5$ biological replicates), T cell counts (**o**) and granzyme B MFI (**p**) ($n = 3$ biological replicates) in Fc–IL-4-treated ex vivo-induced OT1 and OT1$^{STAT6\text{-}KO}$ CD8$^+$ $T_{TE}$ cells (normalized by that in the PBS group) with or without indicated inhibitors. All data represent mean ± s.e.m. and are analysed by two-sided unpaired Student's *t*-test (**b** and **g**,**h**), two-tailed Mann–Whitney test (**j**), right-tailed Fisher's exact test (**k**) or one-way ANOVA and Tukey's test (**n**–**p**). Schematics in **i** created using BioRender (https://Biorender.com).

phosphorylation of STAT6, AKT and P70S6K following Fc–IL-4 treatment (Fig. 4m and Extended Data Fig. 9a–c). To further investigate the role of STAT6, we generated STAT6-KO OT1 (OT1$^{STAT6\text{-}KO}$) T cells (Extended Data Fig. 9d). Compared to WT OT1 T cells, only partial attenuation of the effects of Fc–IL-4 was observed in OT1$^{STAT6\text{-}KO}$ T cells, including the enhancement of glycolysis and increased cell counts and cytotoxicity of CD8$^+$ $T_{TE}$ cells (Fig. 4n–p and Extended Data Fig. 9e–i). By contrast, complete abrogation of Fc–IL-4-mediated benefits occurred when AKT or mTOR signalling was concurrently blocked alongside STAT6-KO (Fig. 4n–p and Extended Data Fig. 9e–i). Furthermore, co-inhibition of STAT6 along with either AKT or mTOR signalling using corresponding inhibitors yielded similar outcomes (Extended Data Fig. 9j–m). The regulatory motif activities of Stat5a/b, also downstream molecules of IL-4/IL-4Rα, showed negligible alteration in IL-4 condition compared to PBS (Extended Data Fig. 9n). Blocking STAT5 signalling had minimal effects on glycolytic metabolism, survival or cytotoxicity of CD8$^+$ $T_{TE}$ cells treated with Fc–IL-4 (Extended Data Fig. 9o–u). Altogether, these results indicate that Fc–IL-4 enhances glycolysis, survival and effector function of CD8$^+$ $T_{TE}$ cells through STAT6 signalling and the PI3K–AKT–mTOR axis.

## Fc–IL-4 promotes glycolysis and NAD$^+$ through LDHA

To identify key enzymes for IL-4-induced glycolysis enhancement, we analysed single-cell ATAC and transcriptome coprofiling datasets. Among several glycolytic enzyme genes with alterations in chromatin accessibility, *Ldha* showcased the most pronounced upregulation after IL-4 treatment (Fig. 5a and Extended Data Fig. 10a,b). Elevated lactate dehydrogenase A (LDHA) expression in Fc–IL-4-treated CD8$^+$ $T_{TE}$ cells was further validated through western blot and flow cytometry

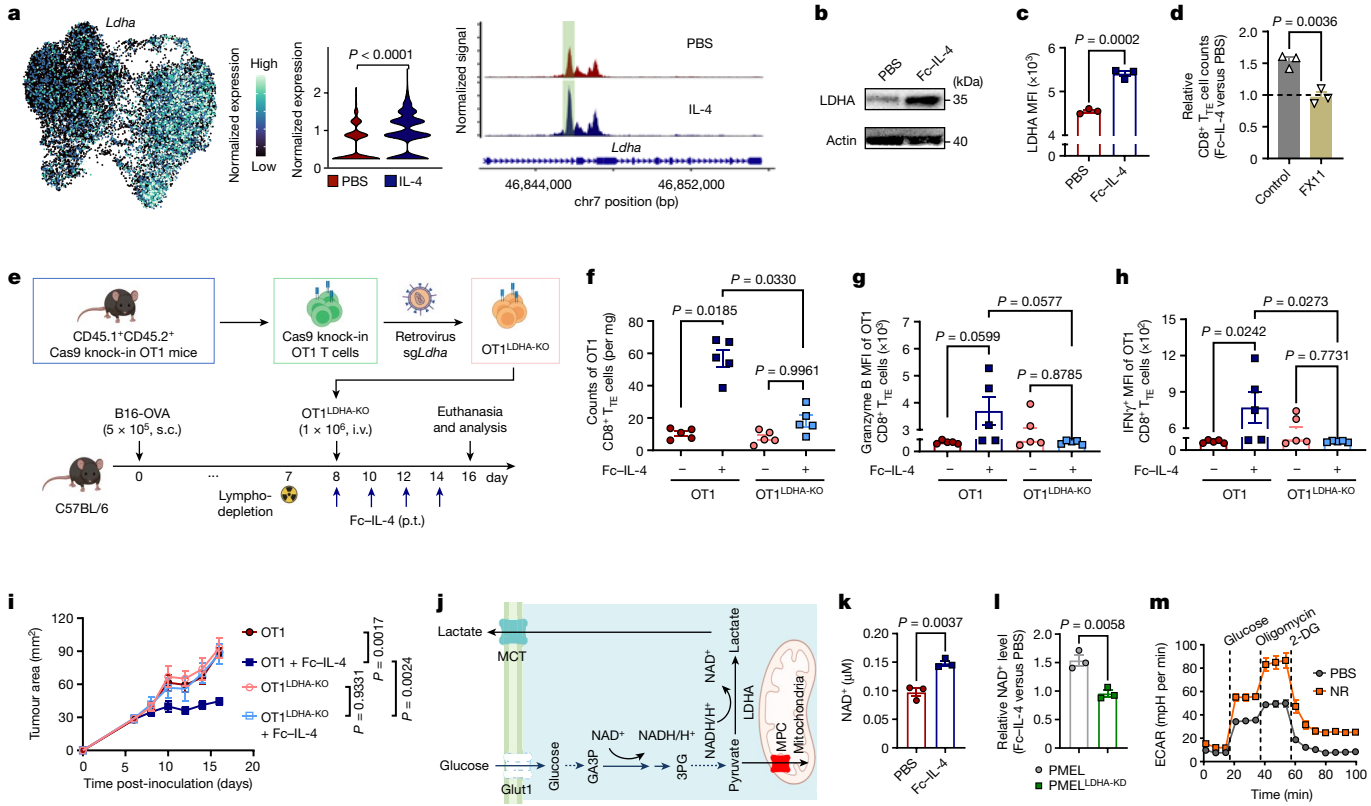


**Fig. 5 | Fc–IL-4 promotes LDHA-mediated glycolysis and cellular NAD⁺ levels of CD8⁺ $T_{TE}$ cells. a**, Expression of *Ldha* on the joint UMAP in Fig. 4i and pseudo-bulk chromatin accessibility tracks in the genomic region of *Ldha*. The enhancer element predicted by ENCODE is highlighted in green. **b**,**c**, Western blot (**b**) and flow cytometry (**c**) analyses of LDHA expression in ex vivo-induced CD8⁺ $T_{TE}$ cells with or without treatment of Fc–IL-4 ($n = 3$ biological replicates). **d**, Relative counts of Fc–IL-4-treated ex vivo-induced CD8⁺ $T_{TE}$ cells normalized by those in the PBS group with or without FX11 ($n = 3$ biological replicates). **e**–**i**, Mice bearing B16-OVA tumours received ACT of activated WT OT1 or OT1$^{LDHA\text{-}KO}$ T cells ($1 \times 10^6$, i.v.) 1 day after lymphodepletion, followed by treatment with Fc–IL-4 (20 μg, p.t.) or PBS every other day for four doses ($n = 5$ animals). Shown are the experimental timeline (**e**), counts (**f**), granzyme B MFI (**g**) and IFNγ MFI (**h**) of tumour-infiltrating OT1 CD8⁺ $T_{TE}$ cells, and average tumour growth curves (**i**). **j**, Schematic illustration of LDHA-mediated NAD⁺/NADH recycling. **k**, Cellular NAD⁺ level of ex vivo-induced CD8⁺ $T_{TE}$ cells with or without treatment of Fc–IL-4 ($n = 3$ biological replicates). **l**, Relative NAD⁺ levels in Fc–IL-4-treated ex vivo-induced PMEL and PMEL$^{LDHA\text{-}KD}$ CD8⁺ $T_{TE}$ cells (normalized by those in the PBS group) ($n = 3$ biological replicates). **m**, Real-time ECAR analysis of ex vivo-induced CD8⁺ $T_{TE}$ cells with or without the treatment with nicotinamide riboside (NR) ($n = 5$ biological replicates). Data are a single representative of three independent experiments. All data represent mean ± s.e.m. and are analysed by two-sided unpaired Student's *t*-test (**a**, **c**, **d**, **k** and **l**) or one-way ANOVA and Tukey's test (**f**–**i**). Schematics in **e**,**j** created using BioRender (https://Biorender.com).

analyses (Fig. 5b,c), and such upregulation was found to rely on STAT6 signalling and PI3K–AKT–mTOR pathways (Extended Data Fig. 10c). Inhibition of LDHA using FX11, a specific LDHA inhibitor, attenuated the effects of Fc–IL-4 on enriching CD8⁺ $T_{TE}$ cells (Fig. 5d). We next knocked down (KD) LDHA expression in PMEL T cells using short hairpin RNA (Extended Data Fig. 10d,e). In contrast to the WT cells, LDHA-KD PMEL (PMEL$^{LDHA\text{-}KD}$) CD8⁺ $T_{TE}$ cells failed to respond to Fc–IL-4 with enhanced glycolysis, enrichment or effector function (Extended Data Fig. 10f–i). Conversely, LDHA overexpression in PMEL T cells (PMEL$^{LDHA\text{-}OE}$) markedly increased their cell enrichment, cytotoxicity and capacity for cancer cell lysis (Extended Data Fig. 10j–m). In addition, unlike WT OT1 T cells, adoptively transferred LDHA-KO OT1 (OT1$^{LDHA\text{-}KO}$) T cells did not show a response to in vivo Fc–IL-4 treatment involving increased counts of intratumoural CD8⁺ $T_{TE}$ cells in mice bearing B16-OVA tumours (Fig. 5e,f and Extended Data Fig. 10n), or enhanced cytotoxicity or effector function (Fig. 5g,h). The combination of ACT of OT1$^{LDHA\text{-}KO}$ T cells with Fc–IL-4 showed substantially diminished efficacy in controlling tumour growth compared to WT OT1 T cells with Fc–IL-4 (Fig. 5i). These results demonstrate that Fc–IL-4 induces the intratumoural enrichment of functional CD8⁺ $T_{TE}$ cells through LDHA.

LDHA plays a crucial role in maintaining NAD⁺–NADH recycling and facilitating NAD⁺ production for the glycolytic circuit (Fig. 5j), with NAD⁺ known to be essential for enhancing cell survival[21]. We found a marked reduction in the cellular NAD⁺ level in CD8⁺ $T_{TE}$ cells compared to progenitor exhausted CD8⁺ T cells (Extended Data Fig. 10o). Treatment with Fc–IL-4 significantly elevated the cellular NAD⁺ level in ex vivo-induced WT CD8⁺ $T_{TE}$ cells, but not in LDHA-deficient cells (Fig. 5k,l). In line with this observation, metabolomic analysis showed a substantial increase in many metabolites involved in nicotinate and nicotinamide metabolic pathways in CD8⁺ $T_{TE}$ cells following Fc–IL-4 treatment (Extended Data Fig. 7k and Extended Data Fig. 10p). Metabolite set enrichment analysis further revealed a notable upregulation of nicotinate and nicotinamide metabolism in cells treated with Fc–IL-4 compared to the PBS control (Extended Data Fig. 10q). Considering that nicotinate or nicotinamide could promote the generation of NAD⁺ through the salvage pathway, we supplemented ex vivo-induced CD8⁺ $T_{TE}$ cells with nicotinamide riboside, a NAD⁺ precursor, resulting in a significant increase in cellular NAD⁺ level (Extended Data Fig. 10r). As an alternative to the metabolic modulation mediated by Fc–IL-4, direct supplementation with nicotinamide riboside similarly promoted glycolytic metabolism in CD8⁺ $T_{TE}$ cells (Fig. 5m and Extended Data Fig. 10s), leading to enhanced T cell expansion, cytolytic activity and cancer cell-killing capacity (Extended Data Fig. 10t,u). Overall, these results indicate that Fc–IL-4 reinvigorates CD8⁺ $T_{TE}$ cells by boosting glycolysis and the cellular NAD⁺ level in a LDHA-dependent manner.

## Discussion

It remains a major challenge to induce long-standing response in patients with cancer receiving immunotherapy. Here, we show that harnessing the power of a type 2 cytokine, Fc–IL-4, enhances the durability of type 1 antitumour immunity mediated by ACT and ICB immunotherapy, leading to enduring tumour regression and antitumour immune memory in several syngeneic and xenograft tumour models. Fc–IL-4 specifically reinvigorates $CD8^+$ $T_{TE}$ cells, a subset of exhausted T cells with potent cancer cell-cytolytic activity within tumours, through enhancing their glycolytic metabolism and cellular $NAD^+$ level in a LDHA-dependent manner. Our findings highlight the remarkable potential of coordinating type 1 and 2 immunity for future development of cancer immunotherapy.

The role of type 2 immunity in antitumour immune responses remains enigmatic[22]. Whereas $T_H2$ cells have traditionally been regarded protumour[23], recent reports offer direct evidence suggesting that type 2 immunity may exert antitumour effects[14,24]. Transfer of tumour antigen-specific $T_H2$ cells has been shown to efficiently eradicate s.c. myeloma and induce durable protection in a manner independent of type 1 immunity[25]. In addition, type 2 innate lymphoid cells were found to respond to anti-PD-1 antibody therapy[26] and to release granzyme B for direct lysis of tumour cells[27], thereby contributing positively to the antitumour efficacy.

Depending on the source, local concentration and responding cells, type 2 cytokines may show pro- or antitumour properties. Endogenous IL-4 secreted by basophils and eosinophils in bone marrow acts on granulocyte–monocyte progenitors to induce protumorigenic myelopoiesis, driving the progression of non-small cell lung cancer (NSCLC)[22]. Conversely, engineered IL-4-secreting renal cancer cells show reduced progression as compared to native cancer cells and induce a systemic antitumour memory response[28]. Moreover, IL-4-deficient mice fail to generate effective antitumour immunity mediated by $T_H1$ and $CD8^+$ T cells on immunization with cancer vaccines[29]. Other type 2 immunity-related cytokines, including IL-5 (ref. 30) and IL-33 (ref. 31), have also shown promise in potentiating immunotherapy for cancer.

In the present study, exogenous Fc–IL-4 was administered directly to the tumour to achieve a high local concentration. The concentration of endogenous IL-4 at a physiological level (roughly $10^3$–$10^6$-fold lower)[32], by comparison, is typically too low to have direct effects on tumour-infiltrating $CD8^+$ $T_{TE}$ cells, and therefore immune suppressive effects by IL-4 may dominate[22]. Thus, correlating endogenous IL-4 levels with prognoses in cancer clinics remains a complex matter[33]. Although $T_H2$ function in pre-infused CAR-T cells with a 4-1BB costimulatory domain was found essential for ultra-long-term remission in patients with acute lymphoblastic leukaemia[4], the IL-4 signalling pathway was recently reported to drive exhaustion of CAR-T cells that rely on a CD28 domain for costimulation[34], suggesting that the impact of type 2 cytokines on CAR-T cell function may depend on the specific structure of CAR design of responding CAR-T cells. Nevertheless, revisiting the role of different components of type 2 immunity in antitumour therapy and exploring their synergies with type 1 immunity could provide new insights for designing next-generation immunotherapy.

Although intratumoural progenitor exhausted $CD8^+$ T cells ($PD\text{-}1^+TIM\text{-}3^-TCF\text{-}1^+$) are commonly considered the primary targets of ICB therapy[7], $CD8^+$ $T_{TE}$ cells ($PD\text{-}1^+TIM\text{-}3^+TCF\text{-}1^-$) remain underexplored for their therapeutic potential, partly because of their survival deficiency, impaired proliferative capacity and lack of responsiveness to ICB and most current immunotherapies. Although $CD8^+$ $T_{TE}$ cells possess compelling tumour-cytolytic abilities and can directly eliminate cancer cells, rejuvenating these cells for cancer immunotherapy poses a considerable challenge. Previously, we demonstrated that an IL-10–Fc fusion protein could enhance the proliferative capacity and effector function of $CD8^+$ $T_{TE}$ cells by promoting oxidative phosphorylation metabolism by means of the pyruvate–mitochondrial pyruvate carrier and STAT3 pathway[12]. In the present work, we find that Fc–IL-4 is another potent therapeutic reagent that directly acts on $CD8^+$ $T_{TE}$ cells, although the mechanism of action appears to be distinct. Fc–IL-4 enhances LDHA-dependent glycolytic metabolism and cellular $NAD^+$ levels of $CD8^+$ $T_{TE}$ cells through STAT6 signalling and the PI3K–AKT-mTOR axis. Instead of promoting proliferation, Fc–IL-4 improves the survival of functional $CD8^+$ $T_{TE}$ cells. Overall, leveraging the therapeutic potential of $CD8^+$ $T_{TE}$ cells is poised to provide a complementary therapeutic strategy to existing immunotherapies, potentially enhancing patients' response rate.

## Online content

Any methods, additional references, Nature Portfolio reporting summaries, source data, extended data, supplementary information, acknowledgements, peer review information; details of author contributions and competing interests; and statements of data and code availability are available at https://doi.org/10.1038/s41586-024-07962-4.


1. Wei, S. C. et al. Distinct cellular mechanisms underlie anti-CTLA-4 and anti-PD-1 checkpoint blockade. *Cell* **170**, 1120–1133 (2017).
2. Lee, E. H. J. et al. Antigen-dependent IL-12 signaling in CAR T cells promotes regional to systemic disease targeting. *Nat. Commun.* **14**, 4737 (2023).
3. Gao, S., Hsu, T. W. & Li, M. O. Immunity beyond cancer cells: perspective from tumor tissue. *Trends Cancer* **7**, 1010–1019 (2021).
4. Bai, Z. et al. Single-cell antigen-specific landscape of CAR T infusion product identifies determinants of CD19-positive relapse in patients with ALL. *Sci. Adv.* **8**, eabj2820 (2022).
5. Gocher, A. M., Workman, C. J. & Vignali, D. A. A. Interferon-γ: teammate or opponent in the tumour microenvironment? *Nat. Rev. Immunol.* **22**, 158–172 (2022).
6. Blank, C. U. et al. Defining 'T cell exhaustion'. *Nat. Rev. Immunol.* **19**, 665–674 (2019).
7. Im, S. J. et al. Defining $CD8^+$ T cells that provide the proliferative burst after PD-1 therapy. *Nature* **537**, 417–421 (2016).
8. Miller, B. C. et al. Subsets of exhausted $CD8^+$ T cells differentially mediate tumor control and respond to checkpoint blockade. *Nat. Immunol.* **20**, 326–336 (2019).
9. Siddiqui, I. et al. Intratumoral $Tcf1^+$ $PD\text{-}1^+$ $CD8^+$ T cells with stem-like properties promote tumor control in response to vaccination and checkpoint blockade immunotherapy. *Immunity* **50**, 195–211 (2019).
10. LaFleur, M. W. et al. PTPN2 regulates the generation of exhausted $CD8^+$ T cell subpopulations and restrains tumor immunity. *Nat. Immunol.* **20**, 1335–1347 (2019).
11. Horton, B. L., Williams, J. B., Cabanov, A., Spranger, S. & Gajewski, T. F. Intratumoral $CD8^+$ T-cell apoptosis is a major component of T-cell dysfunction and impedes antitumor immunity. *Cancer Immunol. Res.* **6**, 14–24 (2018).
12. Guo, Y. et al. Metabolic reprogramming of terminally exhausted $CD8^+$ T cells by IL-10 enhances anti-tumor immunity. *Nat. Immunol.* **22**, 746–756 (2021).
13. Zhao, Y. et al. IL-10-expressing CAR T cells resist dysfunction and mediate durable clearance of solid tumors and metastases. *Nat. Biotechnol.* https://doi.org/10.1038/s41587-023-02060-8 (2024).
14. Liu, M. et al. TGF-β suppresses type 2 immunity to cancer. *Nature* **587**, 115–120 (2020).
15. Dufort, F. J. et al. Cutting edge: IL-4-mediated protection of primary B lymphocytes from apoptosis via Stat6-dependent regulation of glycolytic metabolism. *J. Immunol.* **179**, 4953–4957 (2007).
16. Vella, A., Teague, T. K., Ihle, J., Kappler, J. & Marrack, P. Interleukin 4 (IL-4) or IL-7 prevents the death of resting T cells: Stat6 is probably not required for the effect of IL-4. *J. Exp. Med.* **186**, 325–330 (1997).
17. Hedrick, S. M., Michelini, R. H., Doedens, A. L., Goldrath, A. W. & Stone, E. L. FOXO transcription factors throughout T cell biology. *Nat. Rev. Immunol.* **12**, 649–661 (2012).
18. Chi, H. Regulation and function of mTOR signalling in T cell fate decisions. *Nat. Rev. Immunol.* **12**, 325–338 (2012).
19. Osthus, R. C. et al. Deregulation of glucose transporter 1 and glycolytic gene expression by c-Myc. *J. Bio. Chem.* **275**, 21797–21800 (2000).
20. Wang, X. et al. α-Ketoglutarate-activated NF-κB signaling promotes compensatory glucose uptake and brain tumor development. *Mol. Cell* **76**, 148–162 (2019).
21. Gomes, A. P. et al. Declining NAD+ induces a pseudohypoxic state disrupting nuclear-mitochondrial communication during aging. *Cell* **155**, 1624–1638 (2013).
22. LaMarche, N. M. et al. An IL-4 signalling axis in bone marrow drives pro-tumorigenic myelopoiesis. *Nature* **625**, 166–174 (2023).
23. Alam, A. et al. Fungal mycobiome drives IL-33 secretion and type 2 immunity in pancreatic cancer. *Cancer Cell* **40**, 153–167 (2022).
24. Dobrzanski, M. J., Reome, J. B. & Dutton, R. W. Therapeutic effects of tumor-reactive type 1 and type 2 CD8+ T cell subpopulations in established pulmonary metastases. *J. Immunol.* **162**, 6671–6680 (1999).
25. Lorvik, K. B. et al. Adoptive transfer of tumor-specific Th2 cells eradicates tumors by triggering an in situ inflammatory immune response. *Cancer Res.* **76**, 6864–6876 (2016).
26. Moral, J. A. et al. ILC2s amplify PD-1 blockade by activating tissue-specific cancer immunity. *Nature* **579**, 130–135 (2020).
27. Li, Z. et al. Therapeutic application of human type 2 innate lymphoid cells via induction of granzyme B-mediated tumor cell death. *Cell* **187**, 624–641 (2024).

28. Golumbek, P. T. et al. Treatment of established renal cancer by tumor cells engineered to secrete interleukin-4. *Science* **254**, 713–716 (1991).
29. Schüler, T., Qin, Z., Ibe, S., Noben-Trauth, N. & Blankenstein, T. T helper cell type 1-associated and cytotoxic T lymphocyte-mediated tumor immunity is impaired in interleukin 4-deficient mice. *J. Exp. Med.* **189**, 803–810 (1999).
30. Ikutani, M. et al. Identification of innate IL-5–producing cells and their role in lung eosinophil regulation and antitumor immunity. *J. Immunol.* **188**, 703–713 (2012).
31. Corria-Osorio, J. et al. Orthogonal cytokine engineering enables novel synthetic effector states escaping canonical exhaustion in tumor-rejecting $CD8^+$ T cells. *Nat. Immunol.* **24**, 869–883 (2023).
32. Eini, P., Majzoobi, M. M., Ghasemi Basir, H. R., Moosavi, Z. & Moradi, A. Comparison of the serum level of interleukin-4 in patients with brucellosis and healthy controls. *J. Clin. Lab. Anal.* **34**, e23267 (2020).
33. Goldstein, R. et al. Clinical investigation of the role of interleukin-4 and interleukin-13 in the evolution of prostate cancer. *Cancers* **3**, 4281–4293 (2011).
34. Stewart, C. M. et al. Identification of IL-4 as a key regulator of CAR T-cell exhaustion using functional genomics and correlates of the Zuma-1 clinical trial. *Blood* **140**, 4536–4537 (2022).

# Methods

### Animals

Six- to eight-week-old female CD45.2$^+$Thy1.2$^+$ C57BL/6 (C57BL/6J) mice, CD45.1$^+$ mice (B6.SJL-Ptprca Pepcb/BoyCrl) and NOD.Cg-*Prkdc*$^{scid}$ *Il2rg*$^{tm1Wjl}$/SzJ (NSG) mice were purchased from Charles River Laboratories. CD45.1$^+$CD45.2$^+$ mice were generated by crossing CD45.1$^+$ mice with CD45.2$^+$ C57BL/6 mice. TCR-transgenic Thy1.1$^+$ pmel-1 (PMEL) mice (B6.Cg-Thy1a/Cy Tg(TcraTcrb)8Rest/J) and TCR-transgenic OT-I mice (C57BL/6-Tg(TcraTcrb)1100Mjb/J), CD45.2$^+$ background Rosa26-Cas9 knock-in mice (B6J.129(Cg)-*Gt(ROSA)26Sor*$^{tm1.1(CAG-cas9*,-EGFP)Fezh}$/J) were originally purchased from the Jackson Laboratory and maintained at the EPFL's pathogen-free facility. OT1 mice were crossed with CD45.1$^+$ mice to generate CD45.1$^+$ OT1 mice. CRISPR–Cas9 knock-in CD45.2$^+$ mice were crossed with CD45.1$^+$ OT1 mice to generate CRISPR–Cas9 knock-in OT1 TCR-transgenic mice. *Tcf7*$^{DTR\text{-}GFP}$ P14 mice on a CD45.2 background were generated as described before[9] and maintained at the University of Lausanne's pathogen-free facility. All mice were housed in the EPFL Center of PhenoGenomics or a conventional animal facility of the University of Lausanne and were kept in individually ventilated cages, at 19–23 °C, with 45–65% humidity and with a 12 h dark–light cycle. Experimental procedures in mouse studies were approved by the Swiss authorities (Canton of Vaud, animal protocol IDs VD3206, VD3533, VD3902, VD3912, VD3915 and VD3040x2d) and performed in accordance with the guidelines from the Center of PhenoGenomics of the EPFL and the animal facility of the University of Lausanne.

### Cell lines and tumour models

B16F10 melanoma cells, MC38 mouse colon adenocarcinoma cells, Raji human lymphoma cells, CTLL-2, K562, human embryonic kidney 293T (HEK293T) and Phoenix-Eco cells were originally procured from the American Type Culture Collection. B16-OVA mouse melanoma cell lines were provided by D.J. Irvine (Massachusetts Institute of Technology). B16-gp33 and YUMM1.7-OVA mouse melanoma cell lines were provided by W. Held (University of Lausanne). HER2-transduced MC38 mouse colon cancer cell lines (MC38-HER2) were provided by P. Romero (University of Lausanne). Luciferase-positive Nalm6 cells (Nalm6-luciferase) were provided by S. Chen (Yale University). All cell lines were confirmed mycoplasma-free before use. All mouse tumour cells, HEK293 cells and Phoenix-Eco cells were cultured in complete DMEM (Thermo Fisher Scientific) supplemented with fetal bovine serum (FBS) (10% v/v, Thermo Fisher Scientific), HEPES (1% v/v, Thermo Fisher Scientific), penicillin/streptomycin (1% v/v, Thermo Fisher Scientific), sodium pyruvate (1% v/v, Thermo Fisher Scientific) and 2-mercaptoethanol (0.1% v/v, Thermo Fisher Scientific). Raji lymphoma cells and Nalm6-luciferase cells were cultured in complete RPMI medium (containing RPMI-1640, FBS (10% v/v), HEPES (pH 7.2–7.5, 1% v/v), penicillin/streptomycin (1% v/v) and sodium pyruvate (1% v/v)). CTLL-2 cells were cultured in complete RPMI medium (containing RPMI-1640, FBS (10% v/v), HEPES (pH 7.2–7.5, 1% v/v), penicillin/streptomycin (1% v/v), sodium pyruvate (1% v/v) and 2-mercaptoethanol (0.1% v/v)) supplemented with mouse IL-2 (50 ng ml$^{-1}$, PeproTech). B16F10, B16-gp33, B16-OVA, YUMM1.7-OVA, MC38 or MC38-HER2 tumour cells ($5 \times 10^5$, $1 \times 10^6$ or as indicated) were implanted s.c. into the right flanks of CD45.2$^+$Thy1.2$^+$ C57BL/6 WT mice or CD45.1$^+$CD45.2$^+$ C57BL/6J mice to establish the syngeneic tumour models. Raji lymphoma cells ($2 \times 10^6$) suspended in Matrigel (Corning) were implanted s.c. into the right flanks of NSG mice to establish the Raji lymphoma model. Nalm6-luciferase cells ($1 \times 10^6$) suspended in PBS were i.v. injected into NSG mice to establish the metastatic leukaemia model and the survivor mice from treatment were rechallenged with Nalm6-luciferase cells ($1 \times 10^6$, i.v.) to establish the recurrent leukaemia model. In rechallenge studies, the corresponding tumour cells ($1 \times 10^5$, $5 \times 10^5$ or as indicated) were s.c. implanted into the left flanks of cured mice 2 or 3 months after the initial tumour inoculation.

### Production of mouse and human Fc–IL-4 proteins

As reported previously, both mouse and human Fc–IL-4 fusion proteins were engineered by fusing IL-4 to the C terminus of mutant non-lytic IgG2a Fc[35] by a GS4 linker and then expressed by FreeStyle 293-F cells (Thermo Fisher Scientific) at the EPFL Protein Production and Structure Core Facility[12]. The supernatant of the cell culture medium containing the recombinant protein was filtered through a 0.22 μm membrane (Millipore) to remove cell debris. The recombinant protein was first captured with a HiTrap Protein A affinity chromatography column (Cytiva, 17-0403-01, 5 ml) on an AKTA Pure 25 (GE Healthcare) and then eluted with an elution buffer (0.05 M sodium citrate, 0.3 M sodium chloride, pH 3.3). The eluted protein was collected immediately in a neutralization buffer (1 M Tris HCl, pH 10.0) and then concentrated using the ultrafiltration method (molecular weight cut-off 10 kDa). The concentrated protein solution was further purified with a Superdex 200 Increase size-exclusion chromatography column (GE Healthcare). The purified protein was aliquoted and stored at −80 °C before use. The purity of the recombinant protein was confirmed with sodium dodecyl sulfate–polyacrylamide gel electrophoresis (SDS–PAGE) and the bioactivity was compared with that of commercial IL-4 (Biolegend).

### Preparation of PMEL, OT1 and *Tcf7*$^{DTR\text{-}GFP}$ P14 CD8$^+$ T cells

Spleens from PMEL, OT1 or *Tcf7*$^{DTR\text{-}GFP}$ P14 mice were cut into small pieces and then mechanically meshed through a 70 μm strainer (Fisher Scientific) to obtain a single-splenocyte suspension. ACK lysis buffer (2 ml per spleen, Thermo Fisher Scientific) was added to the above splenocyte pellets to lyse the red blood cells for 3 min at room temperature. After washing twice with cold PBS (Thermo Fisher Scientific) and filtering through a 70 μm strainer again, splenocyte pellets were then resuspended at a cell density of $1 \times 10^6$ per ml in complete RPMI medium (containing RPMI-1640, FBS (10% v/v), HEPES (pH 7.2–7.5, 1% v/v), penicillin/streptomycin (1% v/v), sodium pyruvate (1% v/v) and 2-mercaptoethanol (0.1% v/v)) supplemented with mouse IL-2 (10 ng ml$^{-1}$, PeproTech) and IL-7 (1 ng ml$^{-1}$, PeproTech), as well as human $gp100_{25–33}$, $OVA_{257–264}$ or LCMV $gp_{33–41}$ peptide (0.5 or 1 μM, GenScript) for PMEL, OT1 and P14 T cells, respectively. After 2 or 3 days of culture, live cells were collected by density gradient centrifugation against Ficoll-Paque PLUS (GE Healthcare). The enriched cells were cultured for another 3 days at a cell density of $0.5 \times 10^6$ per millilitre in complete RPMI medium supplemented with mouse IL-2 (10 ng ml$^{-1}$) and IL-7 (10 ng ml$^{-1}$) to obtain activated CD8$^+$ T cells with purity greater than 95% (flow cytometry analyses).

### Preparation of HER2-CAR-T cells

The spinoculation method was used for the preparation of HER2-CAR-T cells. Briefly, Phoenix-Eco cells were first transfected with HER2-CAR carrying plasmid and pCL-Eco packaging plasmid using the calcium phosphate method. After refreshing the supernatant 12 h after the transfection, the virus-containing supernatant for T cell transduction was collected every 24 h after the transfection until 72 h. Before the transduction, splenocytes from WT mice were stimulated with coated anti-mouse CD3 antibody (5 μg ml$^{-1}$, 17A2, BioXcell) and soluble anti-mouse CD28 antibody (5 μg ml$^{-1}$, PV-1, BioXcell) in the presence of IL-2 (10 ng ml$^{-1}$) for 1 day. The activated CD8$^+$ T cells were then isolated as described above for subsequent spin transduction. The above-collected virus-containing supernatant was dispensed into a non-tissue-culture-treated six-well plate, which was precoated with protamine (10 μg ml$^{-1}$, Sigma-Aldrich) overnight at 4 °C and then blocked with PBS containing FBS (v/v 1%) for 20 min before use. The plate loaded with virus-containing supernatant was centrifuged at a speed of 2,000*g* for 2 h at 32 °C to absorb virus particles on the bottom of the plate and the supernatant was then aspirated. Activated CD8$^+$ T cells suspended in the cell culture medium supplemented with mouse IL-2 (10 ng ml$^{-1}$) and

IL-7 (10 ng ml$^{-1}$) were immediately added to the plate and centrifuged at 300*g* for 15 min at 32 °C. The transduction was repeated once 24 h later and the cells obtained were cultured for another 2 or 3 days before use. The transduction efficiency was determined 48 h post-transduction. Untransduced T cells activated by coated anti-mouse CD3 and CD28 antibodies were used as a control.

### Preparation of human CD19-CAR-T cells

Primary T lymphocytes from healthy donors were provided by the Cleveland Clinic's BioRepository Core in accordance with the guidelines from Cleveland Clinic's BioRepository Review Committee. T cells from healthy donor peripheral blood mononuclear cells were purified by negative selection using a T cell isolation kit (Miltenyi) and subsequently activated with CD3/CD28 Dynabeads (Thermo Fisher Scientific) at a cell-to-bead ratio of 1:3. A lentiviral vector carrying a previously described CD19-specific CAR with 4-1BB/CD3ζ transgene was constructed[36] and was used to transduce the cells during the activation phase. It was washed out 3 days after the initiation of culture[37]. Cells were cultured in OpTmizer T Cell Expansion Basal Medium (Thermo Fisher Scientific) supplemented with GlutaMAX supplement (2 mM, Thermo Fisher Scientific), human serum AB (5%, Gemini Bioproducts), IL-7 (5 ng ml$^{-1}$, Miltenyi) and IL-15 (5 ng ml$^{-1}$, Miltenyi). Cell expansion was facilitated using a rocking platform (WAVE Bioreactor System) for a duration of 8 to 12 days, and the beads were then magnetically removed. Finally, CAR-T cells were collected and cryopreserved until the assays were performed.

### Preparation of IL-4Rα-KO OT1, STAT6-KO OT1 and LDHA-KO OT1 CD8$^+$ T cells

To prepare IL-4Rα-KO OT1 (OT1$^{IL\text{-}4R\alpha\text{-}KO}$), STAT6-KO OT1 (OT1$^{STAT6\text{-}KO}$) and LDHA-KO OT1 (OT1$^{LDHA\text{-}KO}$) CD8$^+$ T cells, CRISPR–Cas9 knock-in OT1 CD8$^+$ T cells were isolated from splenocytes of Cas9 knock-in OT1 TCR-transgenic mice using a CD8 negative selection kit (Miltenyi Biotec) and activated with coated anti-mouse CD3 antibody (5 μg ml$^{-1}$, 17A2, BioXcell) and soluble anti-mouse CD28 (5 μg ml$^{-1}$, PV-1, BioXcell) antibody in the presence of IL-2 (10 ng ml$^{-1}$) for 1 day. The activated CD8$^+$ T cells were then spin-transduced twice on days 2 and 3 with retroviruses containing scrambled control guide RNA (gRNA), IL-4Rα-targeting gRNA, STAT6-targeting gRNA or LDHA-targeting gRNA in a non-tissue-culture-treated six-well plate coated with protamine (10 μg ml$^{-1}$, Sigma-Aldrich) as described above. Transduced CD8$^+$ T cells were then expanded for another 3 days before in vitro or in vivo use. The pool of gRNAs targeting IL-4Rα (IL-4Rα-1, 5′–GCAGCAGCGGGGACTGACGA–3′; IL-4Rα-2, 5′–GACACCCTCAAACTTG TCAG–3′; and IL-4Rα-3, 5′– GGCCCCAGTACAGAATGTGG–3′), gRNAs targeting STAT6 (STAT6-1, 5′–CACCGTTGACTTTCCACAACGCC TA–3′; STAT6-2 5′–CACCGAGTTTACTACAGCCCTCGGA–3′; and STAT6-3, 5′–CACCGATAAAGCGCTGTGAGCGGAA–3′) gRNAs targeting LDHA (LDHA-1, 5′–GTTGCAATCTGGATTCAGCG–3′; LDHA-2, 5′–GTCATGGAAGACAAACTCAA–3′; and LDHA-3, 5′–GAAG TCTCTTAACCCAGAAC–3′) and a scrambled gRNA control (5′–GCGAGG TATTCGGCTCCGCG–3′) were designed using the publicly available online gRNA design tool CRISPick. The knockdown efficiency was evaluated at protein expression levels with flow cytometry or western blot.

### Preparation of LDHA-knockdown PMEL CD8$^+$ T cells

To prepare LDHA-knockdown PMEL (PMEL$^{LDHA\text{-}KD}$) CD8$^+$ T cells, shLDHA lentivirus particles were produced in HEK293T cells that were transfected with plasmids of pVSV-G, Delta 8.9 and pLKO.1 puro_shLDHA using the calcium phosphate method as described above. PMEL CD8$^+$ T cells were primed for 1 day as described above. Live activated PMEL CD8$^+$ T cells were collected by density gradient centrifugation against Ficoll-Paque PLUS, resuspended in the complete cell culture medium supplemented with mouse IL-2 (10 ng ml$^{-1}$) and IL-7 (10 ng ml$^{-1}$), and spin-transduced with shLDHA twice, on days 2 and 3. The pool of shLDHA was designed as follows: shLDHA1, 5′–GTTCCCAGTTAAGTC GTATAATCTCTTGAATTATACGACTTAACTGGGAACTTTTTTGGTACC–3′; shLDHA2, 5′–CGTGAACATCTTCAAGTTCATTCTCTTGAAATG AACTTGAAGATGTTCACGTTTTTTGGTACC–3′; shLDHA3, 5′–CGTCTCC CTGAAGTCTCTTAATCTCTTGAATTAAGAGACTTCAGGGAGACGTTTT TTGGTACC–3′. The PMEL$^{LDHA\text{-}KD}$ CD8$^+$ T cells obtained were expanded for another 3 days before in vitro or in vivo use. The knockdown efficiency was evaluated at gene and protein expression levels.

### Preparation of LDHA-overexpression PMEL CD8$^+$ T cells

To prepare LDHA-overexpression PMEL (PMEL$^{LDHA\text{-}OE}$) CD8$^+$ T cells, the retroviral particles were produced in Pheonix Eco cells that were transfected with the pMSGV plasmid containing a Thy1.1 reporter and the LDHA gene using the polyethylenimine (PEI) transfection method. Briefly, PEI (80 μg) was mixed with pMSGV plasmid (21.4 μg) and pCL-Eco plasmid (14.4 μg) in a total of 2 ml serum-free medium. The mixture was incubated at room temperature for 20 min, during which the medium in the T150 flask containing the Pheonix Eco cells was aspirated. The solution of the PEI–DNA complex was then added to the Pheonix Eco cells followed by an incubation at room temperature for 5 min and addition of RPMI medium (14 ml). Virus was collected 48 h later and stored at −80 °C until transduction. PMEL CD8$^+$ T cells were isolated and primed in T75 flasks coated with anti-CD3 and anti-CD28 antibodies for 24 h in complete RPMI cell culture medium supplemented with mouse IL-2 (10 ng ml$^{-1}$) and IL-7 (10 ng ml$^{-1}$), followed by transduction with the LDHA-overexpression retrovirus using the spinoculation method. The LDHA sequence used was National Center for Biotechnology (NCBI) reference sequence NM_010699.2. The PMEL$^{LDHA\text{-}OE}$ CD8$^+$ T cells obtained were expanded in vitro for another 3 days. The transduction efficiency was evaluated at gene and protein expression levels before use.

### Collection of tumour-infiltrating immune cells for analyses

CD45.2$^+$Thy1.2$^+$ C57BL/6 mice bearing B16F10 tumours received i.v. adoptive transfer of activated PMEL CD8$^+$ T cells ($5 \times 10^6$ per mouse), followed by p.t. administration of Fc–IL-4 (20 μg per mouse) or PBS control every other day for four doses. For the BrdU experiments, mice were intraperitoneally (i.p.) administered BrdU (1 mg per mouse, Sigma-Aldrich) 1 day before tumour tissue collection. Tumours were collected, weighed, mechanically minced and stirred at 1,000 r.p.m. in RPMI-1640 medium with collagenase type IV (1 mg ml$^{-1}$, Thermo Fisher Scientific), dispase 2 (100 μg ml$^{-1}$, Sigma-Aldrich), hyaluronidase (100 μg ml$^{-1}$, Sigma-Aldrich) and DNase I (100 μg ml$^{-1}$, Sigma-Aldrich) for 60 min at 37 °C for digestion. Red blood cells in the digested tumour samples were lysed with ACK lysing buffer for 3 min at room temperature. Tumour-infiltrating leukocytes were then enriched by density gradient centrifugation against Percoll (GE Healthcare), resuspended in PBS with bovine serum albumin (0.2%, w/v, Sigma-Aldrich), stained with the indicated antibodies and analysed by flow cytometry.

### Flow cytometry analyses

For surface marker staining, cells were first blocked with anti-mouse CD16/32 antibodies (BioLegend) and incubated with the indicated antibodies at 4 °C for 15 min, followed by live/dead staining using 4,6-diamidino-2-phenylindole (DAPI, Sigma-Aldrich) or Zombie Aqua Fixable Dye (BioLegend). Cells were then washed with PBS containing bovine serum albumin (0.2%, w/v) and resuspended in the same buffer for flow cytometry analyses. For intracellular cytokine staining, cells were first stimulated with Cell Stimulation Cocktail (protein transport inhibitors included, Invitrogen/Thermo Fisher Scientific) at 37 °C for 4–6 h. Cells were then processed as for surface marker staining, followed by live/dead staining using Zombie Aqua Fixable Dye. Next, cells were fixed and permeabilized with the Cytofix/Cytoperm Fixation/

Permeabilization Solution Kit (BD Biosciences) according to the manufacturer's instructions, followed by incubation with indicated antibodies for intracellular cytokine staining. Intracellular active caspase-3 staining was conducted similarly, except that pre-stimulation with the Cell Stimulation Cocktail was not applied. For BrdU and transcription factor staining, cells were first stained for surface markers and with Zombie Aqua Fixable Dye as described above. Next, cells were fixed and permeabilized with the Foxp3/Transcription Factor Staining Buffer Set (eBioscience) according to the manufacturer's instructions, followed by incubation with the indicated antibodies. For intracellular phosphorylated protein staining, cells were first stained for surface markers and with Zombie Aqua Fixable Dye as described above. Next, cells were fixed with a solution of paraformaldehyde (1.5%) at room temperature for 15 min and permeabilized with chilled methanol at 0 °C for 10 min. On complete removal of the paraformaldehyde solution and methanol, cells were incubated with the indicated antibodies for intracellular phosphorylated protein staining at room temperature for 30 min. Data were collected using an Attune NxT Flow Cytometer with Attune NxT Software v.3 (Invitrogen/Thermal Fischer Scientific). Analyses were performed using FlowJo v.10.6.1 (Tree Star). Gate margins were determined by isotype controls and fluorescence-minus-one controls.

**Antibodies and reagents for flow cytometry and western blot**

The following antibodies or staining reagents were purchased from BioLegend: CD16/32 (93, 101302), Thy1.1 (OX-7, 202529), Thy1.2 (30-H12, 105343), CD45.1 (A20, 110707), CD45.2 (104, 109814), CD8α (53-6.7, 100714), CD8β (YTS256.7.7, 126606), CD4 (RM4-5, 100526), NK1.1 (PK136, 108740), F4/80 (BM8,123108), CD3ε (17A2, 100306), CD19 (6D5,115520), CD44 (IM7, 103006), CD11c (N418, 117348), I-A/I-E (MHC-II, M5/114.15.2, 107643), Siglec-F (S17007L, 155508), CD80 (16-10A1, 104734), CD86 (GL-1, 105006), Foxp3 (MF-14, 126406), CD11b (M1/70, 101228), granzyme B (GB11, 515403), IFNγ (XMG1.2, 505826), TNF-α (MP6-XT22, 506308), IL-2 (JES6-5H4, 503822), IL-4Rα (I015F8, 144806), CD69 (H1.2F3, 104512), Gr-1 (RB6-8C5, 108423), CD107a (1D4B, 121626), CD95 (SA367H8, 152608), CD178 (MFL3, 106605), PD-1 (29F.1A12, 135216), TIM-3 (RMT3-23, 119706), TIM-3 (RMT3-23, 119737), HRP-actin (2F1-1, 643808), GATA3 (16E10A23, 653805), Tbet (4B10, 644827), anti-rabbit IgG (minimal cross-reactivity) antibody (Poly4064, 406414), anti-mouse IgG1 antibody (RMG1-1, 406617), STAT6 (16G12A08, 657902), Zombie Aqua Fixable Viability Kit (423102), human CD3 (OKT3, 317306), human CD4 (OKT4, 317416), human CD8 (SK1, 344724), human IFNγ (B27, 506516) and human TNF-α (MAb11, 502940). Anti-TCF-7/TCF-1(S33-966, 566693), anti-phospho-Akt (pT308) (J1-223.371, 558275), anti-phospho-Akt (pS473) (M89-61, 560404), anti-Akt (7/Akt/PKBα, 610836) and anti-active caspase-3 (C92-605.rMAb, 570334) were purchased from BD Biosciences. Anti-CD8 (YTS 169.4, BE0117), anti-CD4 (YTS 177, BE0288), anti-NK1.1 (PK136, BP0036), anti-Ly6G (NIMP-R14, BE0320), IgG (LTF-2, BP0090), anti-IL-4 (11B11, BE0045), anti-mouse CD3 (17A2, BE0002), anti-mouse CD28 (PV-1, BE0015-5), anti-mouse PD-1 (RMP1-14, BE0146) and anti-mouse CTLA-4 (9H10, BE0131) were purchased from BioXcell. Goat anti-rat IgG Fc secondary antibody (31226), eBioscience Cell Stimulation Cocktail (00-4970-03) and anti-phospho-STAT6 (Tyr641) (46H1L12, 700247) were purchased from Invitrogen. Anti-rabbit HRP-IgG (7074) and anti-Glut-1 (73015) were purchased from Cell Signalling Technology. Anti-P70S6K (14485-1-AP) and anti-LDHA (19987-1-AP) were purchased from Proteintech. Anti-phospho-P70S6K (pThr389) (ABIN7265266) was purchased from Antibodies-online. Anti-FMC63 scFv (CAR19) (FM3-HPY53) was purchased from ACRO Biosystems. Antibodies for surface staining were used at a 1:100 dilution, for intracellular staining at a 1:50 dilution and for western blot at a 1:1,000 dilution.

**scRNA-seq library preparation and sequencing**

CD45.2$^+$Thy1.2$^+$ C57BL/6 mice bearing B16F10 tumours received i.v. adoptive transfer of activated Thy1.1$^+$ PMEL CD8$^+$ T cells ($5 \times 10^6$ per mouse), followed by p.t. administration of Fc–IL-4 (20 μg per mouse) or PBS control every other day for four doses. Tumours were collected and digested, and tumour-infiltrating PMEL T cells were enriched and sorted with flow cytometry. Sorted T cells were subjected to single-cell isolation and scRNA-seq library building using GEXSCOPE Single Cell RNA Library Kit Cell V2 reagents (Singleron Biotechnologies GmbH) according to the manufacturer's instructions. Briefly, the cell suspension was loaded into the microfluidic chip and cells were allowed to settle into the microwells. Following the removal of cells that did not settle into the wells, beads containing cell identifying tags (cell barcodes) and unique molecular identifiers (UMI) were flowed into the chip and allowed to settle in the wells on top of the cells. The cells were then lysed and the messenger RNA (mRNA) from each cell hybridized to the barcode sequences on the bead in the same well. After retrieving the beads, the hybridized mRNA was reverse-transcribed into complementary DNA (cDNA). The resulting cDNA was amplified by a minimal number of PCR steps, fragmented, ligated to adaptors and PCR amplified to construct a sequencing library. The gene expression libraries generated were sequenced using an Illumina HiSeq 4000 with a sequencing depth of 50,000 paired-end reads per cell.

**scRNA-seq data processing**

The raw fastq files were generated and de-multiplexed by CeleScope rna from Singleron (v.3.0.1) and primary data analysis was performed with CeleScope (v.1.10.0) using a custom reference package based on the reference genome (Mus_musculus_ensembl_92). Downstream data analysis was performed with the Seurat v.4 pipeline[38]. Cells were first filtered on the basis of two metrics: (1) the number of genes detected per cell must be between 200 and 5,000 and (2) the proportion of mitochondrial gene counts (UMIs from mitochondrial genes/total UMIs) must be less than 10%. Next, the gene expression data were normalized using Seurat sctransform[39]. No major batch effects were observed between the two samples. Finally, the SCT data assay was reduced to two dimensions using uniform manifold approximation and projection (UMAP) for visualization, with 30 computed PCs as input. DEGs were identified using the function 'FindMarkers' for pairwise comparison between two conditions. A log fold-change threshold of 0.25 was applied to select genes as differentially expressed. The function 'AddModuleScore' was used to calculate the module scores of each cluster on the basis of the aggregated expression of defined gene sets. To identify metabolic subpopulations using scRNA-seq data, we performed an unsupervised clustering analysis and UMAP visualization based on the 1,667 genes involved in KEGG-defined metabolic pathways listed in Supplementary Table 2.

**Signalling pathway and upstream regulator analysis**

Ingenuity pathway analysis (Qiagen)[40] was used to reveal the underlying signalling pathways regulated by the DEGs distinguishing each identified cluster or condition. The DEG list and the corresponding fold-change value, *P* value and adjusted *P* value of each gene were loaded into the dataset. The Ingenuity Knowledge Base (genes only) was used as a reference set to perform core expression analysis. T cell-related signalling was selected from the identified canonical pathways to represent the major functional profile of each group. The *z* score was used to determine activation or inhibition level of specific pathways. Conceptually, the *z* score is a statistical measure of how closely the actual expression pattern of molecules in our DEG dataset compares to the pattern that is expected on the basis of the literature for a particular annotation. $z > 0$, activated/upregulated; $z < 0$, inhibited/downregulated; $z \geq 2$ or $z \leq -2$ can be considered significant. The *P* value of each identified signalling pathway was calculated by a right-tailed Fisher's exact test. The significance indicates the probability of association of molecules from the scRNA-seq dataset with the canonical pathway reference dataset. Ingenuity pathway upstream regulator analysis was used to identify upstream regulators, which refers to any molecules

that can affect the expression, transcription or phosphorylation of another molecule, and predict whether they are activated or inhibited given the observed gene expression changes in our DEG dataset. The analysis examines the known targets of each upstream regulator in our dataset, compares the targets' actual direction of change to expectations derived from the literature compiled in the Ingenuity Knowledge Base, and then issues a prediction for each upstream regulator.

### Ex vivo-induced CD8$^+$ $T_{TE}$ cells

Activated PMEL CD8$^+$ T cells in resting phase (day 6 or 7 in culture after collection from spleens) were re-stimulated with dimeric anti-CD3 antibody (0.5 μg ml$^{-1}$ of anti-CD3 antibody or as indicated), which was prepared by mixing anti-CD3 antibody (17A2, BioXcell) and goat anti-rat IgG (Invitrogen/Thermo Fisher Scientific) at a molar ratio of 2:1, in complete RPMI medium supplemented with IL-2 (10 ng ml$^{-1}$) and IL-7 (10 ng ml$^{-1}$) for 2 days. Collected cells were phenotyped with flow cytometry on the basis of the expression level of surface inhibitory receptors (PD-1 and TIM-3). The PD-1$^+$TIM-3$^+$CD8$^+$ T cell subset was sorted as ex vivo-induced CD8$^+$ $T_{TE}$ cells for in vitro and in vivo use.

### In vitro coculture of PMEL T cells and tumour cells

B16F10 tumour cells were cultured in complete DMEM as described above. B16F10 tumour cells ($1.6 \times 10^5$ per well) were seeded in a six-well plate at 37 °C overnight. Following aspiration of tumour culture medium, activated PMEL CD8$^+$ T cells were added to the tumour cell culture at an effector/target (E/T) ratio of 1:2 in the presence or absence of Fc–IL-4 (20 ng ml$^{-1}$). All cells were collected for flow cytometry analyses after 48 h or the indicated time. To determine the lysis of target cells, the cell viability of tumour cells from the coculture was measured with DAPI staining and flow cytometry. Tumour cells cultured alone or with cytokine only, or PMEL CD8$^+$ T cells only, served as controls.

### In vitro coculture of human CD19-CAR-T cells and tumour cells

Human CAR-T cells generated as described above were thawed and suspended in FBS-free medium for 2 h followed by positive purification for CD19-CAR-T cells using a magnetic cell separation kit (Miltenyi Biotec) according to the manufacturer's instructions. Purified CD19-CAR positive CAR-T cells were re-stimulated with K562 cells (E/T = 1/10) for 2 weeks before in vitro use. In a coculture assay, CD19-CAR-T cells were cocultured with Nalm6-luciferase cells (E/T = 1/8) in the presence or absence of human Fc–IL-4 (20 ng ml$^{-1}$). All cells were collected for flow cytometry analyses after 4 days. To determine the lysis of target cells, the cell viability of tumour cells from the coculture was measured with DAPI staining and flow cytometry. Tumour cells cultured alone or CAR-T cells only served as controls.

### Seahorse assay

Seahorse assay was performed to measure the OCR and ECAR of T cells. Ex vivo-induced CD8$^+$ $T_{TE}$ cells ($3 \times 10^5$ per well) with different treatment conditions were seeded in a Seahorse culture plate (Seahorse Bioscience) in a non-$CO_2$ incubator at 37 °C for 40 min. OCR and ECAR were measured by an XF96 Seahorse Extracellular Flux Analyzer (Seahorse Bioscience) following the manufacturer's instructions. In a typical Seahorse assay, cells were treated with oligomycin (1 μM, Sigma-Aldrich), carbonyl cyanide-4-(trifluoromethoxy)phenylhydrazone (FCCP, 1 μM, Sigma-Aldrich), rotenone (0.5 μM, Sigma-Aldrich), antimycin A (0.5 μM, Sigma-Aldrich), glucose (10 mM, Sigma-Aldrich) and 2-DG (50 mM, Sigma-Aldrich). Each condition was performed with 3–6 replicates in a single experiment.

### Assay of single-cell ATAC + gene coprofiling of ex vivo-induced CD8$^+$ $T_{TE}$ cells

Single-cell coprofiling of epigenomic landscape and gene expression in the same single nuclei was performed using the Chromium Next GEM Single Cell Multiome ATAC + Gene Expression kit (10x Genomics). Initially, ex vivo-induced CD8$^+$ $T_{TE}$ cells in the presence or absence of IL-4 (20 ng ml$^{-1}$, Biolegend) underwent washing, counting and nuclei isolation, with an optimized lysis time of 3 min. Subsequently, isolated nuclear suspensions were incubated in a transposition mix containing a transposase enzyme, facilitating preferential fragmentation of DNA in open chromatin regions while introducing adaptor sequences to DNA fragment ends. Roughly 9,250 nuclei were loaded onto a Chromium Next GEM Chip J to target a final recovery of roughly 6,000 nuclei. During GEM generation, gel beads introduced a poly(dT) sequence for barcoded, full-length cDNA production from mRNA for gene expression profiling, along with a spacer sequence for barcode attachment to transposed DNA fragments for ATAC profiling. Following GEM incubation, purification and pre-amplification PCR, separate ATAC and gene libraries were constructed using the standard protocol. Both libraries underwent quality assessment before paired-end reads of 150 bp sequencing on an Illumina NovaSeq 6000 sequencing system.

### Data processing and analysis for the single-cell ATAC + gene coprofiling

The Cell Ranger ARC v.2.0.2 (10x Genomics) was used to perform sample de-multiplexing, barcode processing, identification of open chromatin regions and simultaneous counting of transcripts and peak accessibility in single cells from the sequenced data. Output matrices per barcode underwent joint RNA and ATAC analysis using Signac v.1.12.0 (ref. 41) and Seurat v.4 (ref. 38). Per-cell quality control metrics, including nucleosome banding pattern (stored as nucleosome_signal) and transcriptional start site enrichment score for the ATAC component, were computed, with cells retained on the basis of default settings. Subsequently, peak identification accuracy was enhanced using MACS2 (ref. 42) with the 'CallPeaks' function. We constructed a joint neighbour graph representing both gene expression and DNA accessibility measurements using weighted nearest neighbour methods in Seurat v.4 and investigated potential regulatory elements for genes of interest using the 'LinkPeaks' function. To prepare for motif analyses, we integrated DNA sequence motif information into the dataset using the 'AddMotifs' function and computed a per-cell motif activity score using chromVAR[43].

### Treatment with pharmacological inhibitors

Ex vivo-induced CD8$^+$ $T_{TE}$ cells were re-stimulated with dimeric anti-CD3 antibody (0.5 μg ml$^{-1}$ or as indicated) in complete RPMI medium supplemented with IL-2 (10 ng ml$^{-1}$) and indicated inhibitors (2-DG, 10 mM; FX11, 16 μM; HY-10355, 1 μM; rapamycin, 100 nM; AS1517499, 50 nM or STAT5i, Bestellnummer 573108, 25 μM) for 48 h or as indicated in the presence or absence of Fc–IL-4 (20 ng ml$^{-1}$). Counts and markers for effector function of live CD8$^+$ T cells were determined by flow cytometry analyses.

### Antitumour therapy and rechallenge experiments

Mice bearing established tumours with a size of roughly 25–60 mm$^2$ (day 6 post-inoculation or as indicated) were treated with adoptive transfer of activated PMEL CD8$^+$ T cells, OT1 CD8$^+$ T cells, HER2-CAR-T cells or CD19-CAR-T cells ($5 \times 10^6$ per mouse or as indicated), followed by p.t. administration of Fc–IL-4 (20 μg per mouse) or PBS control every other day or as indicated starting from day 6 (four or eight doses in total as indicated). Mice receiving p.t. administration of PBS control only, Fc–IL-4 only or untransduced T cells served as controls. For therapy studies with immune checkpoint inhibitors, mice bearing established MC38 tumours with a size of roughly 25 mm$^2$ (day 6 post-inoculation) were treated with an i.p. injection of anti-PD-1 (RMP1-14, BioXcell, 100 μg per mouse) and anti-CTLA-4 (9H10, BioXcell, 100 μg per mouse) antibodies followed by p.t. administration of Fc–IL-4 (20 μg per mouse) or PBS control every other day starting from day 6 for four doses in total. Mice receiving PBS only, Fc–IL-4 only or anti-PD-1 plus

anti-CTLA-4 served as controls. Tumour area and body weight were measured every other day. Tumour area was calculated by the formula area = length × width from calliper measurements of two orthogonal diameters. Mice were euthanized when body weight loss was beyond 15%, the tumour area reached 150 $mm^2$ (as a predetermined endpoint) or other endpoints reached the requirements of the animal licences. In the rechallenge studies, B16F10 ($1 \times 10^5$ per mouse), YUMM1.7-OVA ($5 \times 10^5$ per mouse), MC38 ($1 \times 10^5$ per mouse) or MC38-HER2 ($1 \times 10^5$ per mouse) cells were s.c. implanted into the left flanks of cured mice from treatment groups on day 60 or 90 after primary tumour inoculation. Age-matched naive WT mice were s.c. inoculated with the same number of tumour cells as the control. The survival of rechallenged mice was monitored for at least another 60 days. For the treatment of the recurrent Nalm6 leukaemia model, mice bearing metastatic Nalm6-luciferase tumours were treated with adoptive transfer of CD19-CAR-T cells ($2 \times 10^6$ per mouse) followed by i.p. administration of human Fc–IL-4 (100 ng per mouse) or PBS control on day 7 and 11 (two doses in total). The survivor mice were i.v. rechallenged with Nalm6-luciferase ($1 \times 10^6$ per mouse) 17 days after the CAR-T infusion to mimic recurrent leukaemia. The tumour-bearing mice received i.p. administration of D-luciferin potassium salt (Abcam, 150 mg $kg^{-1}$, per mouse) to monitor tumour burden through the IVIS Spectrum In Vivo Imaging System (PerkinElmer). Mice bearing tumours were randomized into groups before treament.

### Measurement of liver enzymes

$CD45.2^+Thy1.2^+$ C57BL/6 mice bearing B16F10 tumours received i.v. adoptive transfer of activated PMEL $CD8^+$ T cells ($5 \times 10^6$ per mouse), followed by p.t. administration of Fc–IL-4 (20 μg per mouse) or PBS control every other day for four doses. On day 14, mice were killed and serum samples were collected for analysis. The levels of ALT and AST in serum were measured using Stanbio Chemistry Reagents (Stanbio) according to the manufacturer's instructions. Healthy mice of the same age without tumours were used as a negative control.

### Immune cell depletion study

Mice bearing established B16F10 tumours with a size of roughly 25 $mm^2$ (day 6 post-inoculation) received adoptive transfer of activated PMEL $CD8^+$ T cells ($5 \times 10^6$ per mouse), followed by p.t. administration of Fc–IL-4 (20 μg per mouse) as described above. Mice were i.p. injected with the anti-CD8 (YTS 169.4, BioXcell, 400 μg per mouse), anti-CD4 (YTS 177, BioXcell, 400 μg per mouse), anti-NK1.1 (PK136, BioXcell, 400 μg per mouse), anti-Ly6G (NIMP-R14, BioXcell, 400 μg per mouse) or IgG (LTF-2, BioXcell, 400 μg per mouse) antibodies 1 day before the treatment and received another two injections of the antibodies during the treatment to deplete the corresponding immune cells. Tumour area and body weight were measured every other day.

### Blockade of T cell egress

Mice bearing B16F10 tumours were treated with adoptive transfer of $CD90.1^+$ PMEL T cells ($5 \times 10^6$ T cells per mouse) followed by administration of Fc–IL-4 (20 μg, p.t.) every other day for six doses in total and FTY720 (40 μg, i.p.) every day for nine doses in total to inhibit T cell egress from peripheral lymphoid organs[44]. Blood was collected every 3 days to monitor peripheral lymphocytes, and mice were euthanized on day 16 to collect tumour tissues for analysis by flow cytometry.

### Depletion of progenitor exhausted $CD8^+$ T cells in vivo

Progenitor exhausted $CD8^+$ T cells were deleted as previously reported[9]. Briefly, $CD45.1^+CD45.2^+$ C57BL/6 mice bearing established B16-gp33 tumours with a size of roughly 25–40 $mm^2$ (day 6 post-inoculation or as indicated) received adoptive transfer of activated $CD45.2^+$ *Tcf7*$^{DTR\text{-}GFP}$ transgenic P14 $CD8^+$ T cells 1 day after whole-body irradiation (4 Gy) for lymphodepletion. Diphtheria toxin (1 μg per mouse, Sigma-Aldrich) was i.p. injected twice to deplete the DTR-expressing cells before starting the Fc–IL-4 treatments.

### Cotransfer of naive OT1 and PMEL T cells

$CD45.2^+$ C57BL/6 mice were sublethally lymphodepleted (4 Gy) on day −4 and received adoptive cotransfer of $CD45.1^+$ naive OT1 T cells ($2 \times 10^6$, i.v.) and $CD90.1^+$ naive PMEL T cells ($2 \times 10^6$, i.v.) on day −3. The mice were then inoculated with B16F10 tumour cells on day 0. On day 7, the mice were treated with ACT of activated $CD90.2^+$ PMEL T cells ($5 \times 10^6$, i.v.), followed by administration of Fc–IL-4 (20 μg, p.t.) or PBS every other day for four doses. On day 15, mice were euthanized and tumour tissues were collected for flow cytometry analysis.

### Adoptive transfer of sorted PD-$1^+$TIM-$3^-$ and PD-$1^+$TIM-$3^+$ $CD8^+$ T cells

The PD-$1^+$TIM-$3^-$ and PD-$1^+$TIM-$3^+CD8^+$ T cell subsets were generated and sorted from ex vivo-induced $CD8^+$ $T_{TE}$ cells as described above. Mice bearing B16F10 tumours received adoptive transfer of PD-$1^+$TIM-$3^-$ ($1 \times 10^6$, i.v.) or PD-$1^+$TIM-$3^+$ PMEL T cells ($1 \times 10^6$, i.v.) 1 day after lymphodepletion, followed by treatment with Fc–IL-4 (20 μg, p.t.) or PBS every other day for four doses in total. Mice were euthanized on day 15 and tumour tissues were collected for analysis by flow cytometry.

### Neutralization of endogenous IL-4

$CD45.2^+Thy1.2^+$ C57BL/6 mice bearing B16F10 tumours received i.v. adoptive transfer of activated PMEL $CD8^+$ T cells ($5 \times 10^6$ per mouse), followed by administration of anti-IL-4 antibody (11B11, BioXcell, 200 μg, p.t.) or PBS control every other day for six doses. Tumour area was measured every other day and tumours were collected for analysis of tumour-infiltrating immune cells as described above.

### RNA extraction and real-time PCR analysis

Total RNA was extracted using Trizol reagent (Invitrogen) and reverse-transcribed into cDNA using the High-Capacity RNA-to-cDNA kit (Applied Biosystems). Real-time PCR was performed using SYBR Green Master Mix reagents (Applied Biosystems) in the QuantStudio 6 Flex quantitative PCR system. The expression of each gene was calculated on the basis of the cycle threshold, set within the linear range of DNA amplification. The relative expression was calculated by the cycle threshold method, with normalization of raw data to the housekeeping gene *Actb*.

### Metabolomic analysis

Ex vivo-induced $CD8^+$ $T_{TE}$ cells were re-stimulated with dimeric anti-CD3 antibody (0.5 μg $ml^{-1}$) in complete RPMI medium supplemented with IL-2 (10 ng $ml^{-1}$) for 48 h in the presence or absence of Fc–IL-4 (20 ng $ml^{-1}$), and then live $CD8^+$ T cells were sorted for metabolomic analyses. Samples ($0.5 \times 10^6$ $CD8^+$ T cells in 50 μl PBS) were pre-extracted and homogenized by the addition of 200 μl of methanol in the Cryolys Precellys 24 sample homogenizer (twice for 20 s at 10,000 r.p.m., Bertin Technologies) with ceramic beads. The bead beater was air-cooled at a flow rate of 110 L $min^{-1}$ at 6 bar. Homogenized extracts were centrifuged for 15 min at 4,000*g* at 4 °C (Hermle). The resulting supernatant was collected and evaporated to dryness in a vacuum concentrator (LabConco). Dried sample extracts were resuspended in methanol:$H_2O$ (4:1, v/v) according to the total protein content. The protein pellets were evaporated and lysed in 20 mM Tris HCl (pH 7.5), 4 M guanidine hydrochloride, 150 mM NaCl, 1 mM $Na_2EDTA$, 1 mM EGTA, 1% Triton, 2.5 mM sodium pyrophosphate, 1 mM β-glycerophosphate, 1 mM $Na_3VO_4$, 1 μg $ml^{-1}$ leupeptin using the Cryolys Precellys 24 sample homogenizer (2 × 20 s at 10,000 r.p.m., Bertin Technologies) with ceramic beads. The BCA Protein Assay Kit (Thermo Scientific) was used to measure (by absorbance at 562 nm) total protein concentration (Hidex). Extracted samples were analysed by hydrophilic interaction liquid chromatography coupled to tandem mass spectrometry in both positive and negative ionization modes using a 6495 Triple Quadrupole system interfaced with a 1290

UHPLC system (Agilent Technologies). Pooled quality control samples were analysed periodically throughout the overall analytical run to assess the quality of the data, correct signal intensity drift and remove peaks with poor reproducibility. In addition, a series of diluted quality controls were prepared by dilution with methanol: 100, 50, 25, 12.5 and 6.25% quality controls. Next, metabolites were selected also considering the linear response on the diluted quality control series. Raw liquid chromatography with tandem mass spectrometry data were processed using the Agilent Quantitative analysis software (v.B.07.00, MassHunter, Agilent Technologies). Relative quantification of metabolites was based on extracted ion chromatography areas for the multiple reaction monitoring transitions. The tables obtained (containing peak areas of detected metabolites in all samples) were exported to R software (http://cran.r-project.org/). Signal intensity drift correction and noise filtering was done within the MRM PROBS software. The preprocessed data with peak areas were imported into Metaboanalyst v.5.0 for further data analysis.

### Glucose uptake assay

Ex vivo-induced $CD8^+$ $T_{TE}$ cells were re-stimulated with dimeric anti-CD3 antibody (0.5 μg $ml^{-1}$) in complete RPMI medium supplemented with IL-2 (10 ng $ml^{-1}$) for 48 h in the presence or absence of Fc–IL-4 (20 ng $ml^{-1}$). The supernatant was collected to measure the glucose concentration using the Glucose Colorimetric Detection Kit (Invitrogen, EIAGLUC) according to the manufacturer's instructions. The glucose uptake capacity was calculated with the equation below:

$$\text{Glucose uptake capacity} = (1 - \text{supernatant glucose concentration}/\text{fresh medium glucose concentration}) \times 100\%$$

### Measurement of cellular $NAD^+$ and NADH

Ex vivo-induced $CD8^+$ $T_{TE}$ cells were re-stimulated with dimeric anti-CD3 antibody (0.5 μg $ml^{-1}$) in complete RPMI medium supplemented with IL-2 (10 ng $ml^{-1}$) for 48 h in the presence or absence of Fc–IL-4 (20 ng $ml^{-1}$). The cellular $NAD^+$ and NADH levels of $CD8^+$ $T_{TE}$ cells were measured using a $NAD^+$/NADH assay kit (Sigma-Aldrich, MAK460) according to the manufacturer's instructions.

### Nicotinamide riboside supplementation assay

Ex vivo-induced $CD8^+$ $T_{TE}$ cells were re-stimulated with dimeric anti-CD3 antibody (0.5 μg $ml^{-1}$) or cocultured with B16F10 at an E/T ratio of 0.5 in the complete RPMI medium supplemented with IL-2 (10 ng $ml^{-1}$) for 48 h in the presence or absence of the $NAD^+$ precursor nicotinamide riboside (100 μM). The cell viability, effector function and metabolic activity of $CD8^+$ T cells were measured using flow cytometry and Seahorse assay as described above.

### Statistical analysis

Unless stated otherwise, all statistical analyses were performed using GraphPad Prism v.10 (GraphPad Software). Data are presented as mean ± s.e.m. unless otherwise specified. Comparison of two groups was performed using a two-sided unpaired Student's *t*-test or Mann–Whitney test unless otherwise noted. Comparison of three or more groups was performed using one-way ANOVA with Tukey's test or two-way ANOVA and Sidak's multiple comparisons test unless otherwise indicated. Survival data were analysed using the log-rank test. No statistically significant differences were considered to be present when *P* values were larger than 0.05. No statistical methods were used to predetermine sample size.

### Ethics statement

Experiments and handling of mice were conducted under federal, state and local guidelines and with approval from the Swiss authorities (Canton of Vaud, animal protocol IDs VD3206, VD3533, VD3902, VD3912, VD3915 and VD3040x2d) and performed in accordance with the guidelines of Center of PhenoGenomics at EPFL and the animal facility of the University of Lausanne. Primary T lymphocytes from healthy donors were provided by the Cleveland Clinic's BioRepository Core in accordance with guidelines from Cleveland Clinic's BioRepository Review Committee.

### Reporting summary

Further information on research design is available in the Nature Portfolio Reporting Summary linked to this article.

## Data availability

All data generated and supporting the findings of this study are available within the article. Raw and processed single-cell sequencing data for this study can be accessed in the NCBI Gene Expression Omnibus database under the accession number GSE259409. Further information and materials will be made available upon reasonable request. Source data are provided with this paper.

## Code availability

Single-cell analysis code used in this study is available from the corresponding authors upon reasonable request.


35. Tzeng, A., Kwan, B. H., Opel, C. F., Navaratna, T. & Wittrup, K. D. Antigen specificity can be irrelevant to immunocytokine efficacy and biodistribution. *Proc. Natl Acad. Sci. USA* **112**, 3320–3325 (2015).
36. Milone, M. C. et al. Chimeric receptors containing CD137 signal transduction domains mediate enhanced survival of T cells and increased antileukemic efficacy in vivo. *Mol. Ther.* **17**, 1453–1464 (2009).
37. Levine, B. L. et al. Gene transfer in humans using a conditionally replicating lentiviral vector. *Proc. Natl Acad. Sci. USA* **103**, 17372–17377 (2006).
38. Hao, Y. et al. Integrated analysis of multimodal single-cell data. *Cell* **184**, 3573–3587 (2021).
39. Hafemeister, C. & Satija, R. Normalization and variance stabilization of single-cell RNA-seq data using regularized negative binomial regression. *Genome Biol.* **20**, 296 (2019).
40. Krämer, A., Green, J., Pollard, J. & Tugendreich, S. Causal analysis approaches in ingenuity pathway analysis. *Bioinformatics* **30**, 523–530 (2014).
41. Stuart, T., Srivastava, A., Madad, S., Lareau, C. A. & Satija, R. Single-cell chromatin state analysis with Signac. *Nat. Methods* **18**, 1333–1341 (2021).
42. Zhang, Y. et al. Model-based analysis of ChIP–seq (MACS). *Genome Bio.* **9**, R137 (2008).
43. Schep, A. N., Wu, B., Buenrostro, J. D. & Greenleaf, W. J. ChromVAR: inferring transcription-factor-associated accessibility from single-cell epigenomic data. *Nat. Methods* **14**, 975–978 (2017).
44. Von Scheidt, B. et al. Enterotoxins can support CAR T cells against solid tumors. *Proc. Natl Acad. Sci. USA* **116**, 25229–25235 (2019).



**Acknowledgements** We thank D. Trono (EPFL) and B. E. Correia (EPFL) for providing plasmids for Delta 8.9 and pVSV-G, S. Chen (Yale University) for providing the luciferase-positive Nalm6 cell line, D. J. Irvine (Massachusetts Institute of Technology) for providing the plasmid for mutant Fc and B16-OVA mouse melanoma cell line, P. Romero (University of Lausanne) for providing the MC38-HER2 colon cancer cell line, X. Li (EPFL) for assistance on metabolomics analysis and J. Auwerx (EPFL) for providing access to a Seahorse XFe96 Analyzer. We acknowledge the Center of PhenoGenomics, Flow Cytometry Core Facility, and Protein Production and Structure Core Facility at EPFL and the UNIL Centre of Metabolomics Platform for technical assistance. L.T. acknowledges the grant support from the Swiss National Science Foundation (grant nos. 315230_204202, IZLCZ0_206035, CRSII5_205930), European Research Council under European Research Council grant agreement MechanoIMM (grant no. 805337), Swiss Cancer Research Foundation (grant no. KFS-4600-08-2018), Kristian Gerhard Jebsen Foundation, Anna Fuller Fund, Xtalpi Inc. and EPFL. Y.L. was supported by the Chinese Scholarship Council (grant no. 202206340040). M.G. was supported by the Chinese Scholarship Council (grant no. 201808320453). W.H. was supported in part by a grant from the Swiss Cancer Research Foundation (grant no. KFS-5386-08-2021). R.F. was supported by a Stand Up to Cancer (SU2C) Convergence 2.0 grant and the Packard Fellowship for Science and Engineering (grant no. 2012-38215). Y.G. was supported in part by a grant from Shenzhen Science and Technology Program (grant no. KJZD20230923114101003) and Zhejiang University. All schematics were created with BioRender.com.


**Author contributions** B.F., Y.G. and L.T. conceived the study and designed the experiments. B.F., Z.B., X.Z., Y.Z., Y.-Q.X., X.H., Y.L., T.E., R.L., Y.W., M.G., L.B., M.-W.P., W.L., B.T., M.C., W.H., J.J.M. and Y.G. performed the experiments. B.F., Z.B., X.Z., W.H., R.F., Y.G. and L.T. analysed the data. B.F., Z.B., R.F., Y.G. and L.T. wrote the paper with input from all other authors.

**Competing interests** Y.G., L.T. and B.F. are inventors of the patents relevant to the findings reported here. L.T. and Y.G. are cofounders, share-holders and advisors for Leman Biotech. The interests of L.T. were reviewed and managed by EPFL. R.F. is scientific founder and adviser for IsoPlexis, Singleron Biotechnologies and AtlasXomics. The interests of R.F. were reviewed and managed by Yale University Provost's Office in accordance with the University's conflict of interest policies. J.J.M. hold patents related to CAR-T cell manufacturing and biomarker discovery. The remaining authors declare no competing interests.

**Additional information**
**Supplementary information** The online version contains supplementary material available at https://doi.org/10.1038/s41586-024-07962-4.
**Correspondence and requests for materials** should be addressed to Rong Fan, Yugang Guo or Li Tang.
**Peer review information** *Nature* thanks Justin Eyquem and the other, anonymous, reviewer(s) for their contribution to the peer review of this work. Peer reviewer reports are available.

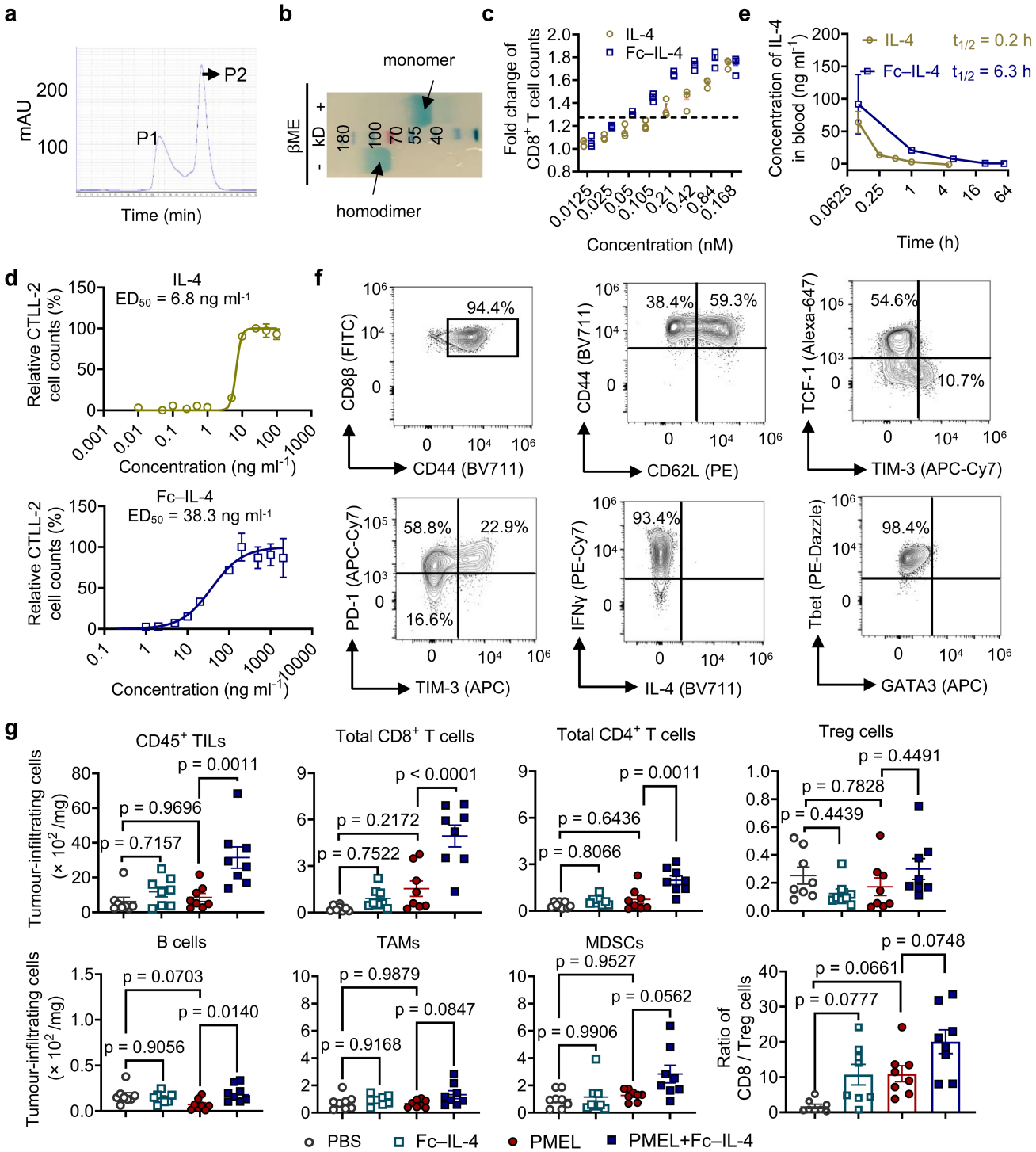


**Extended Data Fig. 1 | Characterizations of Fc–IL-4 and investigation of its impact on tumour-infiltrating immune cells. a**, Representative size-exclusion chromatographic traces of Fc–IL-4 fusion protein. Peak 2 (P2) was collected and analysed. **b**, SDS-PAGE analysis of purified Fc–IL-4. βME, β-mercaptoethanol (Image is one representative of two independent experiments). **c**, Fold change of PMEL T cell counts (normalized by that in PBS group) upon treatment of IL-4 or Fc–IL-4 at equivalent concentrations in vitro. **d**, Median effective dose ($ED_{50}$) of native IL-4 and Fc–IL-4 was determined using the CTLL-2 proliferation assay. **e**, The pharmacokinetics in plasma and half-life of IL-4 and Fc–IL-4 (n = 3 animals). **f**, The phenotype, cytokine production, and expression of transcription factors of activated PMEL T cells prior to transfer. **g**, Experimental setting was described in Fig. 1a. Shown are counts of various tumour-infiltrating immune cells. Treg, regulatory $CD4^+$ T cells; TAMs, tumour-associated macrophages; MDSCs, myeloid-derived suppressive cells. Data are one representative of three independent experiments with n = 3 biological replicates (**c**, and **d**) or one representative of two independent experiments with n = 8 animals (**g**). All data represent mean ± s.e.m. and are analysed by one-way ANOVA and Tukey's test.

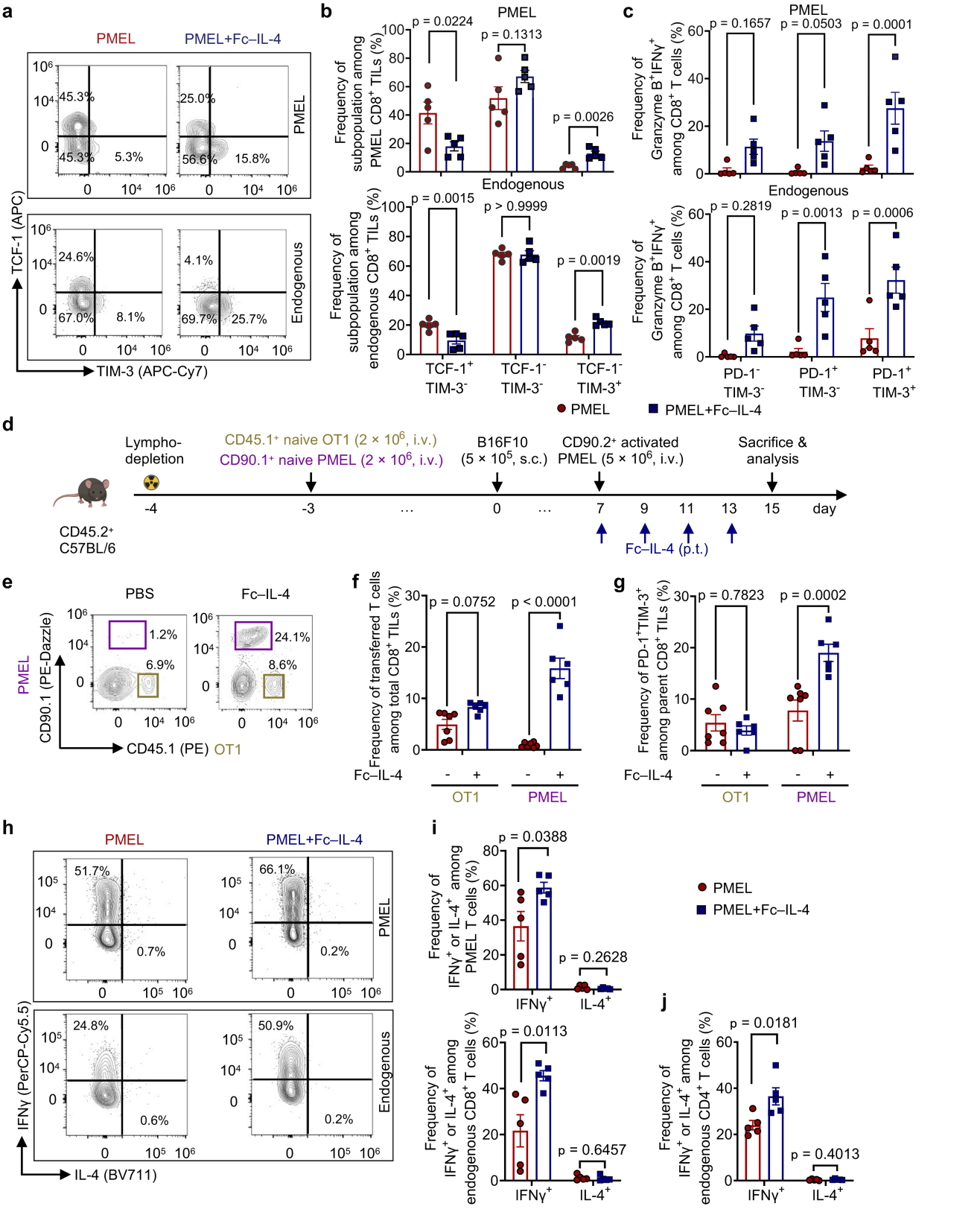


**Extended Data Fig. 2** | See next page for caption.

**Extended Data Fig. 2 | Fc–IL-4 enriches CD8$^+$ $T_{TE}$ cells in an antigen-dependent manner. a**-**c**, Experimental setting was similar to that described in Fig. 1a (n = 5 animals). Shown are the representative flow cytometry plots (**a**) and the frequencies (**b**) of CD8$^+$ $T_{TE}$ cells (TCF-1$^-$TIM-3$^+$) among PMEL or endogenous CD8$^+$ TILs, and frequencies of Granzyme B$^+$IFNγ$^+$ among different subpopulations of PMEL or endogenous CD8$^+$ TILs (**c**). **d**-**g**, CD45.2$^+$ C57BL/6 mice were sublethally lymphodepleted on day -4 and received adoptive co-transfer of CD45.1$^+$ naive OT1 T cells ($2 \times 10^6$, i.v.) and CD90.1$^+$ naive PMEL T cells ($2 \times 10^6$, i.v.) on day -3. The mice were then inoculated with B16F10 tumour cells on day 0. On day 7, the mice were treated with ACT of activated CD90.2$^+$ PMEL T cells ($5 \times 10^6$, i.v.) followed by administration of Fc–IL-4 (20 μg, p.t.) or PBS every other day for 4 doses. On day 15, mice were euthanized and tumour tissues were collected for flow cytometry analysis (n = 6 animals). Shown are the experimental timeline (**d**), representative flow cytometry plots (**e**), frequencies of transferred CD45.1$^+$ OT1 and CD90.1$^+$ PMEL T cells among total CD8$^+$ TILs (**f**), and frequencies of PD-1$^+$TIM-3$^+$ subpopulation among transferred CD45.1$^+$ OT1 or CD90.1$^+$ PMEL T cells (**g**). **h**-**j**, Experimental setting was similar to that described in Fig. 1a (n = 5 animals). Shown are representative flow cytometry plots (**h**) and frequencies of IFNγ$^+$ or IL-4$^+$ among PMEL and endogenous CD8$^+$ T cells (**i**), and frequencies of IFNγ$^+$ or IL-4$^+$ among endogenous CD4$^+$ T cells (**j**). All data represent mean ± s.e.m. and are analysed by two-way ANOVA and Sidak multiple comparisons test (**b**, and **c**), or two-sided unpaired Student's t-test (**f**-**j**). Schematic in **d** created using BioRender (https://Biorender.com).

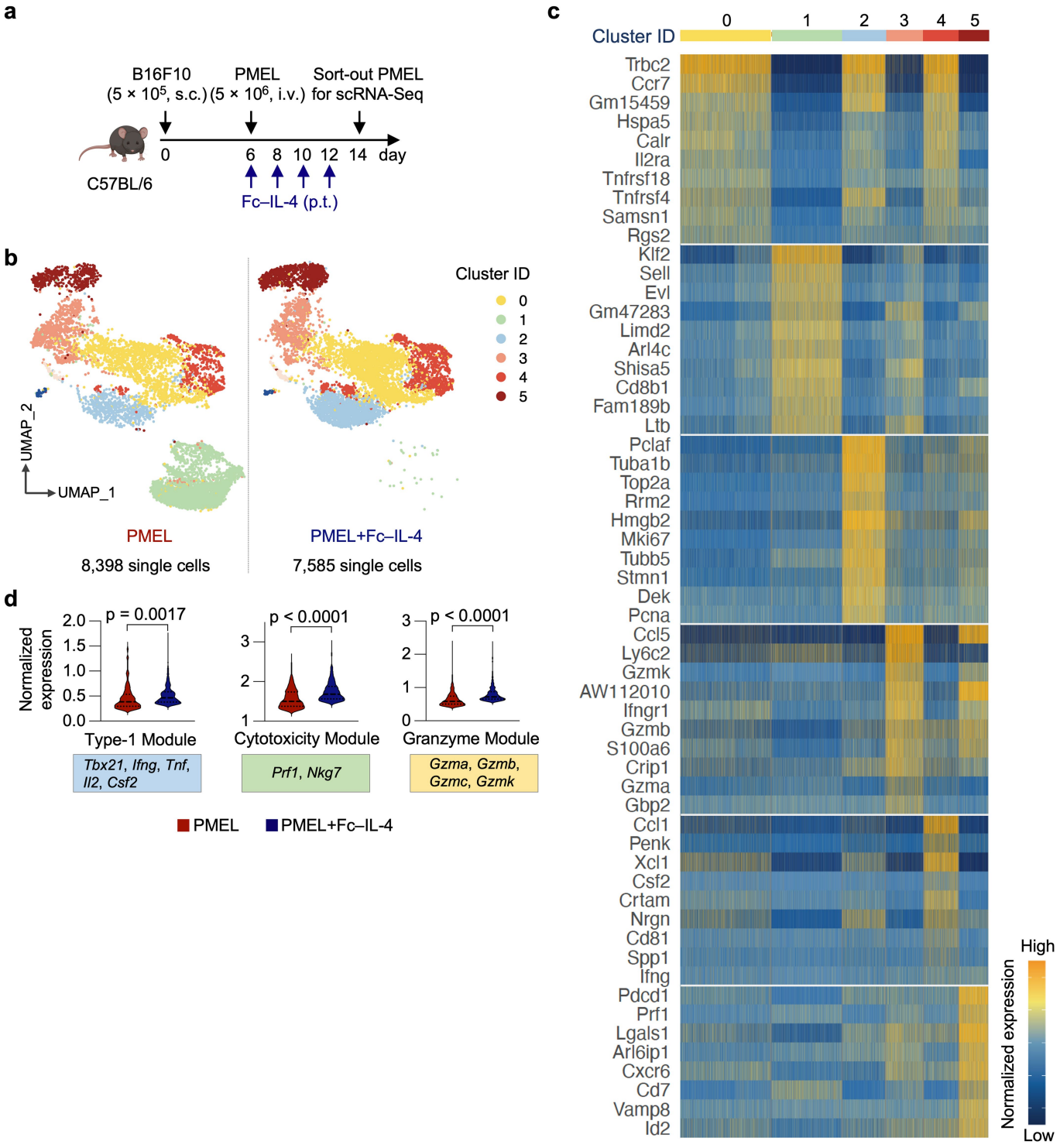


**Extended Data Fig. 3 | Single-cell RNA-seq analysis of antigen-specific CD8⁺ T cells treated with Fc–IL-4. a**, Schematic of the experimental setting (as described in Fig. 1g). **b**, UMAP clustering of all the antigen-specific PMEL CD8⁺ T cells, split by the treatment condition (PMEL or PMEL + Fc–IL-4). **c**, Heatmap of differentially expressed genes defining the top 6 identified clusters. **d**, Comparison of functional gene module expression of all the terminally exhausted-like cells from PMEL or PMEL + Fc–IL-4 group. Genes defining each group are listed below. Statistical analyses are performed using two-sided unpaired Student's t-test. Schematics in **a** created using BioRender (https://Biorender.com).

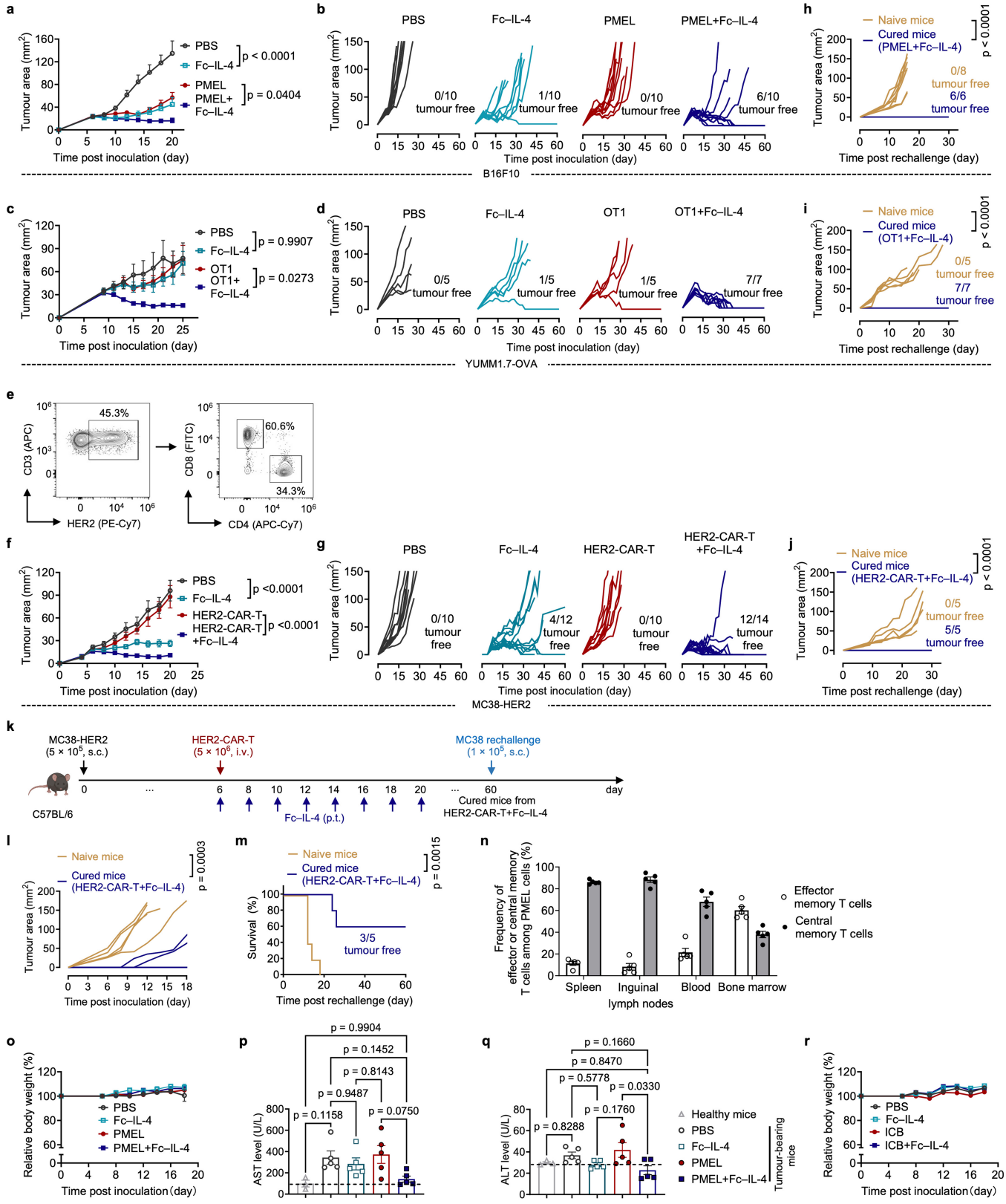


**Extended Data Fig. 4** | See next page for caption.

**Extended Data Fig. 4 | Fc–IL-4 potentiates ACT and ICB immunotherapies and induces long-term immune memory without overt toxicities.** **a**-**j**, Experimental setting was described in Fig. 2a. Shown are average and individual tumour growth curves of mice bearing B16F10 (**a**, and **b**) (n = 10 animals), YUMM1.7-OVA (**c**, and **d**) (n = 7 animals), and MC38-HER2 (**f**, and **g**) (n = 14 animals) tumours. HER2-CAR-T cells were analysed by flow cytometry for the frequency of $CD4^+$ and $CD8^+$ T cells prior to transfer (**e**). Shown are individual tumour growth curves of naive or cured mice re-challenged with B16F10 (**h**) (n = 6 animals), YUMM1.7-OVA (**i**) (n = 7 animals), and MC38-HER2 (**j**) (n = 5 mice) tumour cells. **k**-**m**, Experimental setting was similar to that described in Fig. 2a except that the surviving mice were rechallenged with the parental cell line, MC38. Shown are the experimental timeline (**k**), tumour growth curves (**l**), and survival curves (**m**) of the rechallenged mice (n = 5 animals). **n**, Experimental setting was described in Fig. 2a (n = 5 animals). Surviving mice from the combinatory treatment were euthanized 120 days post-treatment and various tissues were collected for flow cytometry analysis. Shown is the frequencies of effector memory (defined as $CD44^+CD62L^-$) and central memory (defined as $CD44^+CD62L^+$) T cells among PMEL T cells in different tissues. **o**, Experimental setting was described in Fig. 2a. Shown is the relative body weight of B16F10 tumour-bearing mice. **p**, **q**, Experimental setting was similar to that described in Fig. 1a and the peripheral blood was collected on day 14 for AST and ALT liver enzyme assays (n = 5 animals). Shown are serum AST (**p**) and ALT (**q**) levels of B16F10 tumour-bearing mice. **r**, Experimental setting was described in Fig. 2h (n = 5 animals). Shown is the relative body weight of MC38 tumour-bearing mice. Data are one representative of two independent experiments. All data represent mean ± s.e.m. and are analysed by one-way ANOVA and Tukey's test (**a**, **c**, **f**, **p**, and **q**), two-sided unpaired Student's t-test (**h**-**j**, and **l**), or log-rank test (**m**). Schematics in **k** created using BioRender (https://Biorender.com).

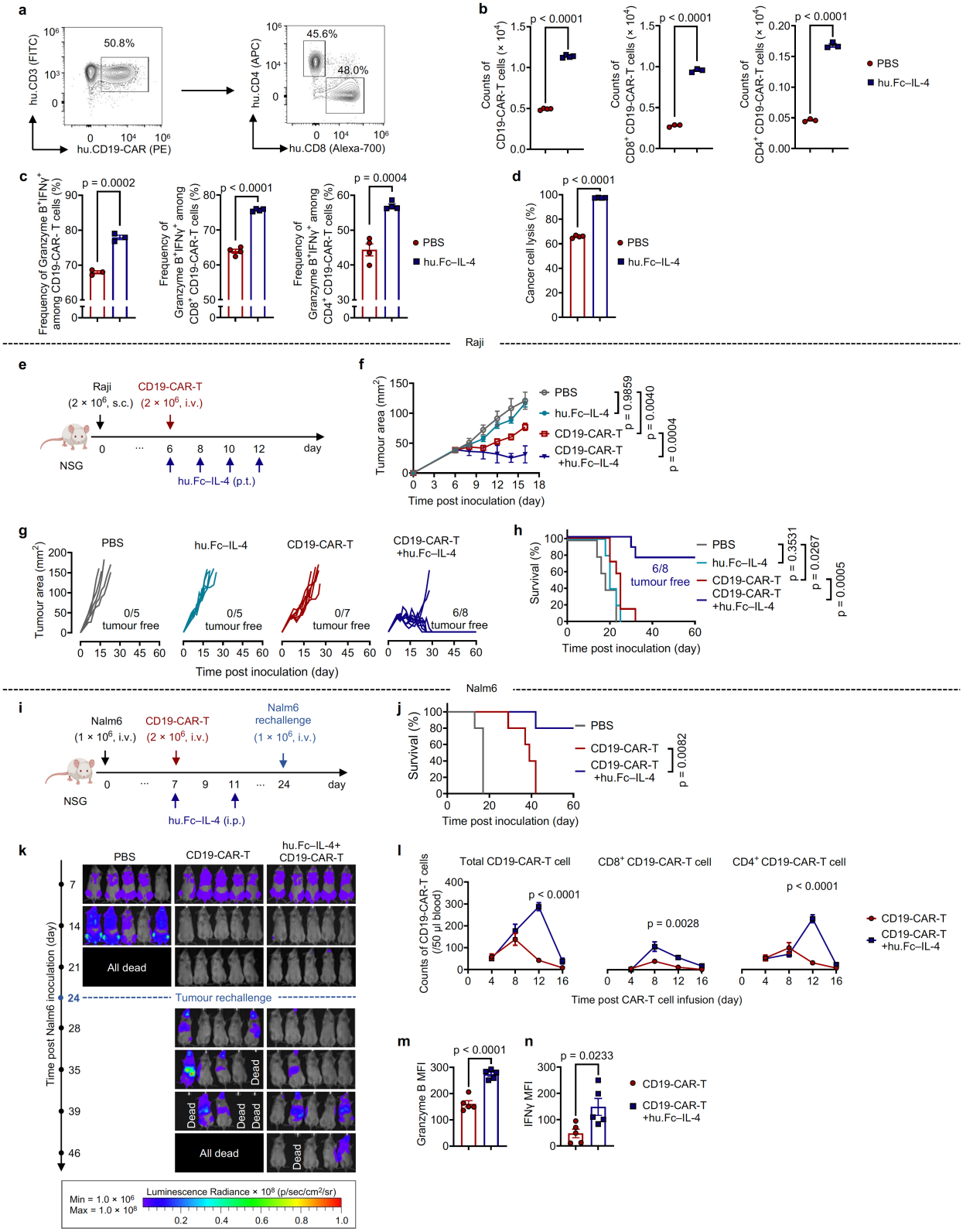


**Extended Data Fig. 5** | See next page for caption.

**Extended Data Fig. 5 | Fc–IL-4 enhances efficacy of human CD19-CAR-T cell therapy. a**, Representative flow cytometry plots showing the frequency of $CD4^+$ and $CD8^+$ T cells among CD19-CAR-T cells prior to transfer. **b**-**d**, Human CD19-CAR-T cells were co-cultured with Nalm6 cells at an effector/target (E/T) ratio of 1:8 for 4 days in the presence or absence of hu.Fc–IL-4 (20 ng $ml^{-1}$). Shown are the counts of total CD19-CAR-T cells (n = 4 biological replicates), $CD8^+$ and $CD4^+$ CD19-CAR-T cells (n = 3 biological replicates) (**b**), and frequencies of Granzyme $B^+IFN\gamma^+$ among total CD19-CAR-T cells (n = 3 biological replicates), $CD8^+$ and $CD4^+$ CD19-CAR-T cells (n = 4 biological replicates) (**c**), and percent of cancer cell lysis (**d**) (n = 4 biological replicates). **e**-**h**, NSG mice were inoculated with Raji cells ($2 \times 10^6$, s.c.) and received ACT of CD19-CAR-T cells ($2 \times 10^6$, i.v.) on day 6 followed by administration of hu.Fc–IL-4 (20 µg, p.t.) (n = 8 animals) or PBS (n = 7 animals) every other day for 4 doses. Mice receiving injections of PBS or hu.Fc–IL-4 only served as controls (n = 5 animals). Shown are the experimental timeline (**e**), average tumour growth curves (**f**), individual tumour growth curves (**g**), and Kaplan-Meier survival curves (**h**) of treated mice (n = 8 animals). **i**-**n**, NSG mice were inoculated with Nalm6-luciferase cells ($1 \times 10^6$, i.v.) and received ACT of CD19-CAR-T cells ($2 \times 10^6$, i.v.) on day 7 followed by administration of hu.Fc–IL-4 (100 ng, i.p.) or PBS. The survivor mice were rechallenged with Nalm6-luciferase cells ($1 \times 10^6$, i.v.) on day 24 (n = 5 animals). Shown are the experimental timeline (**i**), Kaplan-Meier survival curves (**j**), bioluminescence images representing the tumour burden (**k**), the counts of total CD19-CAR-T cells, $CD8^+$ and $CD4^+$ CD19-CAR-T cells in peripheral blood at various time points following CAR-T cell infusion (**l**), the MFI of Granzyme B (**m**) and IFNγ (**n**) of CD19-CAR-T cells in peripheral blood on day 12 post CAR-T cell infusion. All data represent mean ± s.e.m. and are analysed by two-sided unpaired Student's t-test (**b**-**d**, and **l**-**n**), one-way ANOVA and Tukey's test (**f**), or log-rank test (**h**, and **j**). Schematics in **e**,**i** created using BioRender (https://Biorender.com).

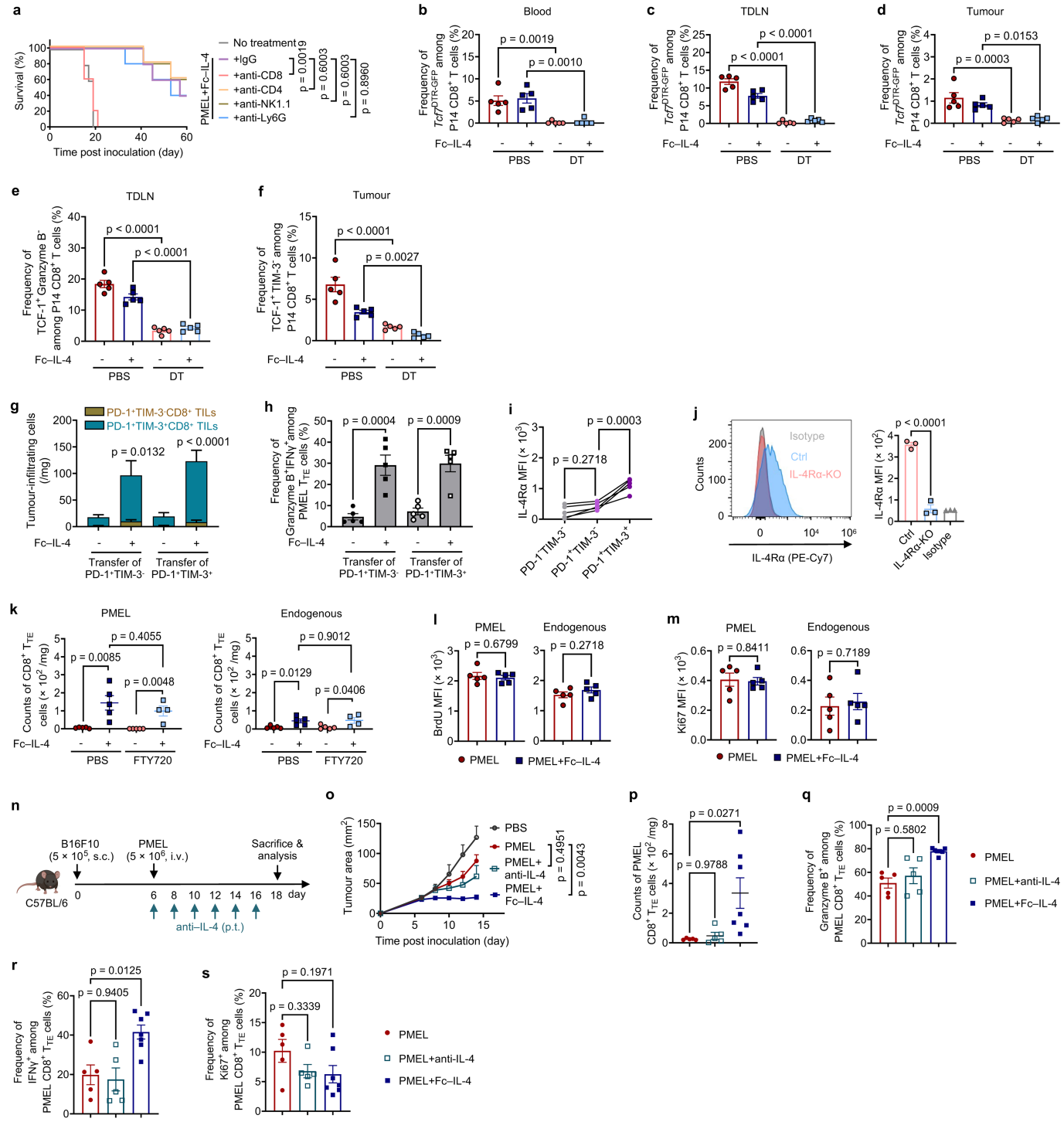


**Extended Data Fig. 6** | See next page for caption.

**Extended Data Fig. 6 | Fc–IL-4 directly acts on CD8$^+$ $T_{TE}$ cells through IL-4Rα for enhanced survival and effector function. a**, B16F10 tumour-bearing mice receiving treatment of ACT of PMEL T cells ($5 \times 10^6$, i.v.) were injected with IgG, anti-CD8, anti-CD4, anti-NK1.1, or anti-Ly6G antibodies (400 μg × 3, i.p.) to deplete the corresponding immune cells (n = 5 animals). Shown are the Kaplan-Meier survival curves of each treatment group. **b**-**f**, Experimental setting was similar to that described in Fig. 3a except that mice were euthanized on day 12 and the tumour-draining lymph node (TDLN), spleen, blood, and tumour tissues were collected for analysis by flow cytometry (n = 5 animals). Shown are the frequencies of *Tcf7*$^{DTR\text{-}GFP+}$ progenitor exhausted T cells among transferred P14 T cells in the peripheral blood (**b**), TDLN (**c**), and tumour (**d**), and frequencies of TCF-1$^+$Granzyme B$^-$ among transferred P14 T cells in the TDLN (**e**), and frequencies of TCF-1$^+$TIM-3$^-$ among transferred P14 T cells in the tumour (**f**). **g**, **h**, One day post-lymphodepletion, mice bearing B16F10 tumours received ACT of PD-1$^+$TIM-3$^-$ ($1 \times 10^6$, i.v.) or PD-1$^+$TIM-3$^+$ PMEL T cells ($1 \times 10^6$, i.v.) on day 7, which were sorted from ex vivo-induced PMEL T cells, followed by the treatment of Fc–IL-4 (20 μg, p.t.) or PBS every other day for 4 doses (n = 5 animals). Mice were euthanized on day 15 and the tumour tissues were collected for analysis by flow cytometry. Shown are the counts of PMEL T cells (**g**) and frequency of Granzyme B$^+$IFNγ$^+$ among PMEL CD8$^+$ $T_{TE}$ cells (**h**). **i**, MFI of IL-4Rα expression among different subsets of tumour-infiltrating CD8$^+$ T cells (n = 5 animals). **j**, IL-4Rα expression in OT1$^{IL\text{-}4Rα\text{-}KO}$ T cells examined by flow cytometry (n = 3 biological replicates). **k**, B16F10 tumour-bearing mice were treated with ACT of PMEL T cells ($5 \times 10^6$, i.v.) on day 6 followed by administration of Fc–IL-4 (20 μg, p.t.) or PBS every other day for 6 doses, and FTY720 (40 μg, i.p.) every day for 9 doses in total. Mice were euthanized on day 16 to collect the tumour tissues for flow cytometry analysis. Shown are counts of PMEL and endogenous CD8$^+$ $T_{TE}$ cells in the tumour (n = 5 animals). **l**, **m**, Experimental setting was described in Fig. 3k. Shown are BrdU MFI (**l**), and Ki67 MFI (**m**) of PMEL and endogenous CD8$^+$ $T_{TE}$ cells (n = 5 animals). **n**-**s**, B16F10 tumour-bearing mice received ACT of PMEL T cells ($5 \times 10^6$, i.v.) followed by administration of anti-IL-4 antibody (200 μg, p.t.), or Fc–IL-4 (20 μg, p.t.), or PBS every other day for 6 doses. Mice were euthanized on day 18 and the tumour tissues were collected for analysis by flow cytometry (n = 5 animals). Shown are the experimental timeline (**n**), average tumour growth curves (**o**), counts of tumour-infiltrating PMEL CD8$^+$ $T_{TE}$ cells (**p**), frequencies of Granzyme B$^+$ (**q**), IFNγ$^+$ (**r**), and Ki67$^+$ (**s**) among tumour-infiltrating PMEL CD8$^+$ $T_{TE}$ cells. Data are one representative of two independent experiments. All data represent mean ± s.e.m. and are analysed by log-rank test (**a**), one-way ANOVA and Tukey's test (**b**-**k**, and **o**-**s**), or two-sided unpaired Student's t-test (**l**, and **m**). Schematic in **n** created using BioRender (https://Biorender.com).

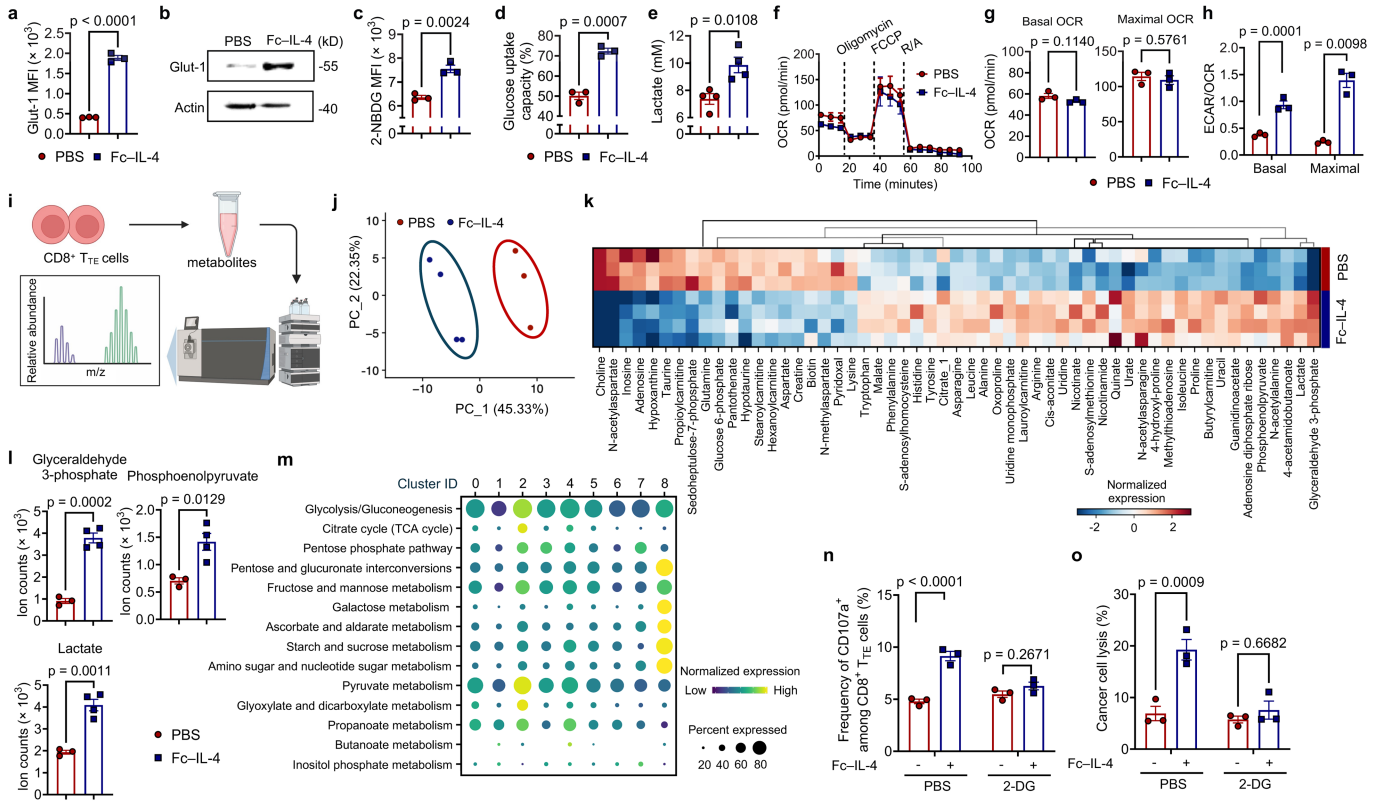


**Extended Data Fig. 7 | Fc–IL-4 enhances glycolytic metabolism of CD8$^+$ $T_{TE}$ cells in vitro and in vivo. a**-**e**, Ex vivo-induced CD8$^+$ $T_{TE}$ cells were re-stimulated by dimeric anti-CD3 antibody (0.5 μg ml$^{-1}$) for 48 h in the presence or absence of Fc–IL-4 (n = 3 biological replicates). Shown are the Glut-1 MFI (**a**), WB images of Glut-1 (**b**), glucose uptake capacity measured by the 2-NBDG assay (**c**) and the Glucose Colorimetric Detection Kit (Invitrogen™, EIAGLUC) (**d**), and extracellular lactate concentration (**e**). **f**, Real-time OCR analysis of ex vivo-induced CD8$^+$ $T_{TE}$ cells re-stimulated by dimeric anti-CD3 antibody (0.5 μg ml$^{-1}$) for 48 h in the presence or absence of Fc–IL-4 (n = 3 biological replicates). **g**, Average basal and maximal OCR calculated from **f**. pmol, pico mole. **h**, The ratio of basal and maximal ECAR to OCR. **i**-**l**, Ex vivo-induced CD8$^+$ $T_{TE}$ cells were re-stimulated by dimeric anti-CD3 antibody (0.5 μg ml$^{-1}$) and treated with Fc–IL-4 (n = 4 biological replicates) or PBS (n = 3 biological replicates). The metabolites were collected for metabolomics analysis. Shown are the schematic illustration of metabolomic analysis (**i**), Principal Component Analysis (PCA) of 120 metabolites of CD8$^+$ $T_{TE}$ cells (**j**), and heatmap showing the metabolic expression pattern of each sample in the Fc–IL-4 and PBS groups (**k**). The fold change between Fc–IL-4 vs. PBS was calculated for each metabolite, and only metabolites with significant differences ($p < 0.05$) were included. Shown are the cellular ion counts of glyceraldehyde 3-phosphate, phosphoenolpyruvate, and lactate in ex vivo-induced CD8$^+$ $T_{TE}$ cells (**l**). Multiple pathway targeted analysis results of metabolites are provided in Supplementary Table 1. **m**, Experimental setting was described in Fig. 1g. Shown is the systematic expression comparison of carbohydrate metabolisms across all identified clusters in Fig. 4d, with each metabolic pathway name indicated. The size of circle represents proportion of single cells expressing the pathway, and the colour shade indicates normalized expression level. Genes defining each pathway are provided in Supplementary Table 2. **n**, **o**, B16F10 tumour cells were co-cultured with ex vivo-induced CD8$^+$ $T_{TE}$ cells in the presence or absence of Fc–IL-4 with or without the treatment of 2-DG (10 mM) (n = 3 biological replicates). Shown are the frequencies of CD107a$^+$ among CD8$^+$ T cells (**n**) and percent of cancer cell lysis (**o**). Data are one representative of three independent experiments. All data represent mean ± s.e.m. and are analysed by two-sided unpaired Student's t-test. Schematic in **i** created using BioRender (https://Biorender.com).

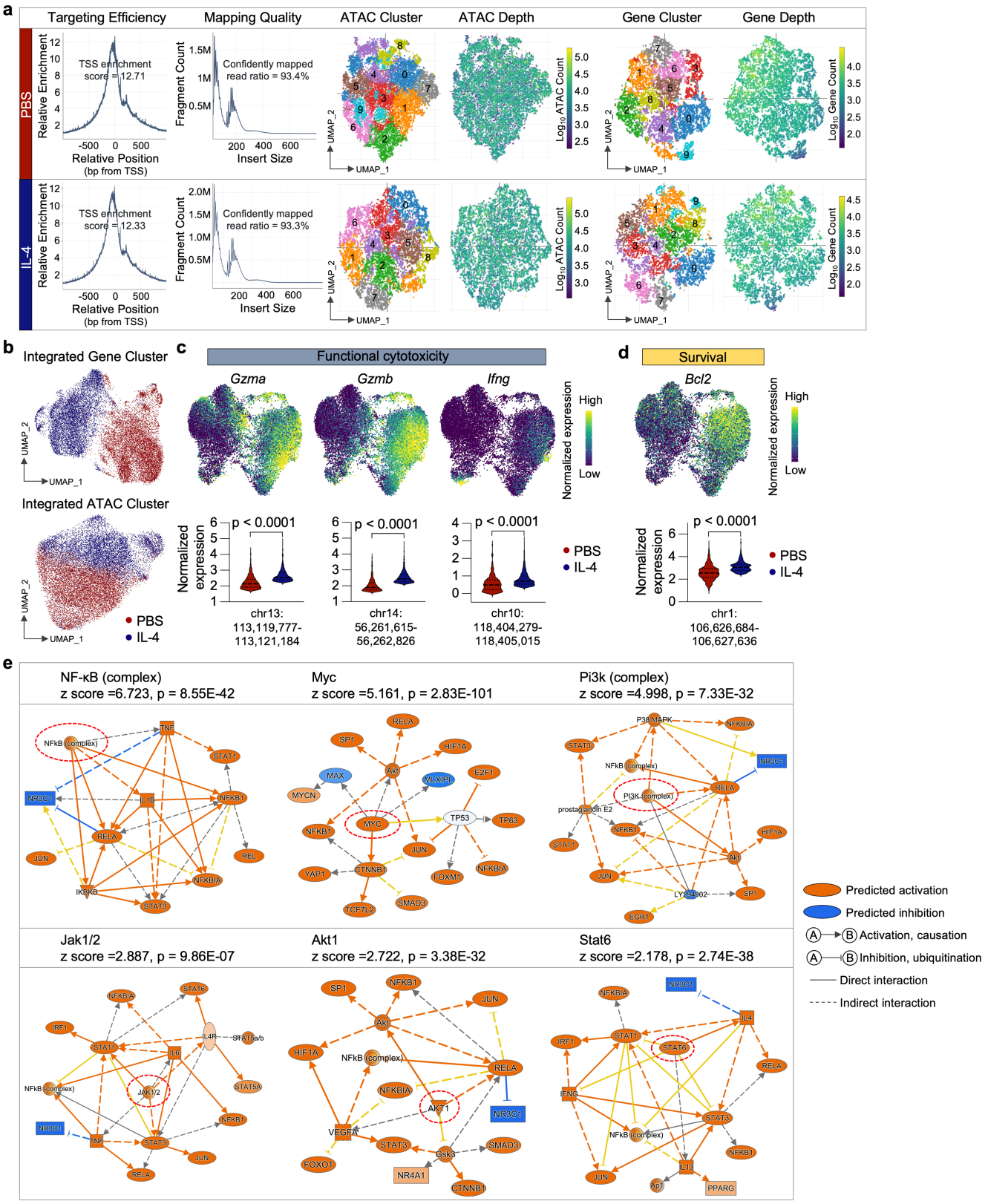


**Extended Data Fig. 8** | See next page for caption.

**Extended Data Fig. 8 | Single-cell ATAC and gene co-profiling analysis of IL-4 treated PMEL CD8$^+$ $T_{TE}$ cells and upstream regulator analysis based on scRNA-seq results. a**, Quality assessment of sequenced data from IL-4 or PBS conditions, featuring TSS enrichment score, insert size distribution, unsupervised clustering analysis of ATAC and gene datasets, and corresponding count distribution. Consistent performance is observed with negligible batch effect. **b**, Gene or ATAC expression UMAP of all the single cells color-coded by their respective conditions. **c**, **d**, Expression of functional cytotoxicity (**c**) and survival (**d**) gene markers on the joint UMAP in Fig. 4i, along with comparisons of corresponding accessible peaks between conditions. Statistical analyses were performed using two-sided unpaired Student's t-test. **e**, Experimental setting was described in Fig. 1g. Shown is the mechanistic networks associated with the significant activation of selected upstream regulators in Fc−IL-4 treated PMEL CD8$^+$ TILs relative to the PBS condition. z score is computed and used to reflect the predicted activation level ($z > 0$, activated/upregulated; $z < 0$, inhibited/downregulated; $z \geq 2$ or $z \leq -2$ can be considered significant). Statistical analyses are performed using right-tailed Fisher's Exact Test.

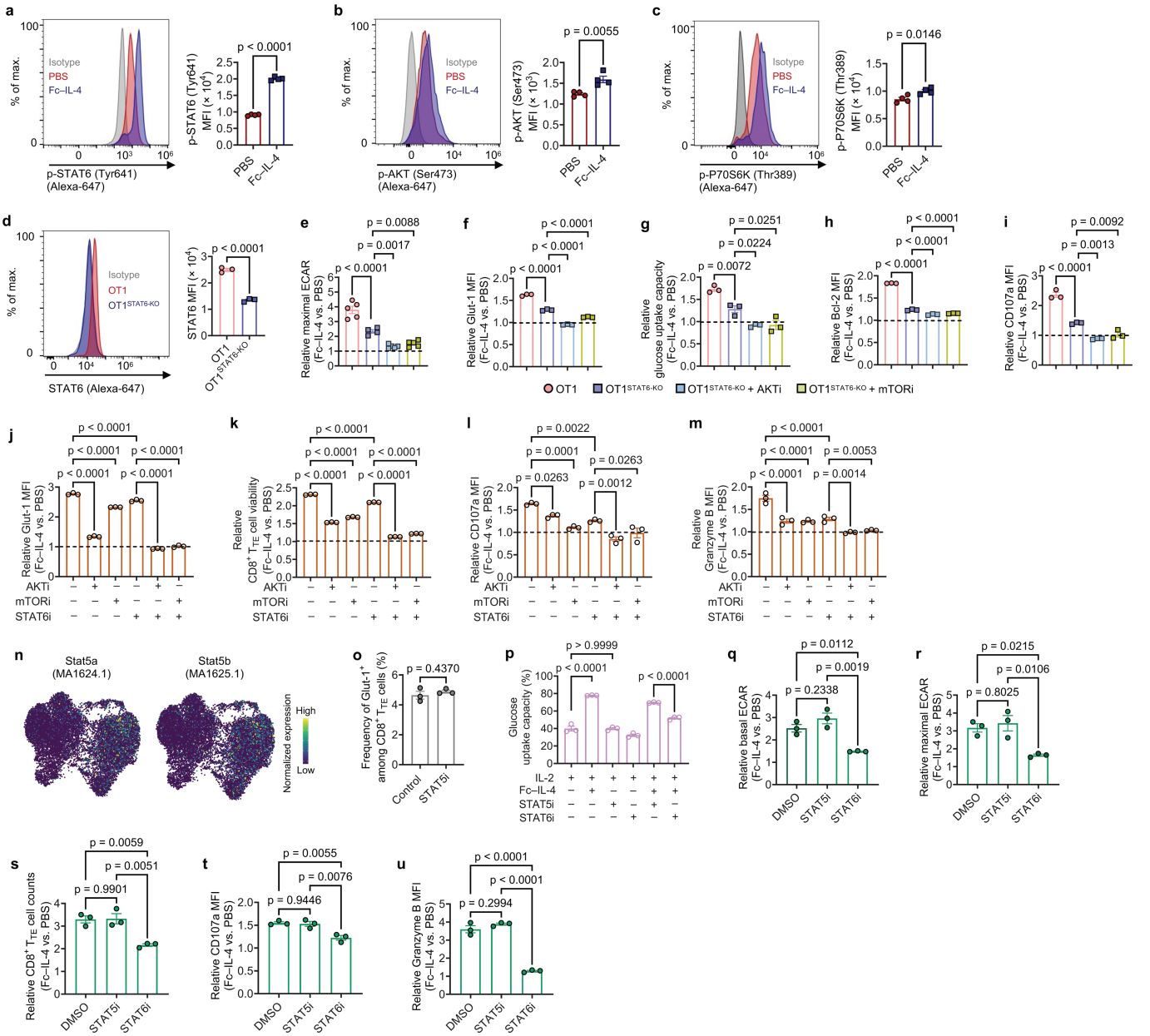


**Extended Data Fig. 9 | Fc–IL-4 enhances the glycolytic metabolism of CD8$^+$ $T_{TE}$ cells through STAT6 signalling and PI3K-AKT-mTOR axis. a**-**c**, Ex vivo-induced PMEL CD8$^+$ $T_{TE}$ cells were re-stimulated by dimeric anti-CD3 antibody (0.1 μg ml$^{-1}$) in the presence or absence of Fc–IL-4 (n = 4 biological replicates) for 0.5 h. Shown are the representative flow cytometry plots and MFI of p-STAT6 (**a**), p-AKT (Ser473) (**b**), p-P70S6K (Thr389) (**c**). **d**, STAT6 was knock-out in OT1 T cells using CRISPR-Cas9 gene editing (n = 3 biological replicates). Shown are representative flow cytometry plots and MFI of STAT6. **e**-**i**, Ex vivo-induced OT1 and OT1$^{STAT6\text{-}KO}$ CD8$^+$ $T_{TE}$ cells were re-stimulated by dimeric anti-CD3 antibody (0.5 μg ml$^{-1}$) with AKT inhibitor VIII (HY-10355, 1 μM), mTOR inhibitor (Rapamycin, 100 nM), or no inhibitors, in the presence or absence of Fc–IL-4 for 24 h (n = 3 biological replicates). Shown are relative maximal ECAR (**e**), Glut-1 MFI (**f**), glucose uptake capacity (**g**), Bcl-2 MFI (**h**), and CD107a MFI (**i**) in the Fc–IL-4 treatment group normalized by that in the PBS group. **j**-**m**, Ex vivo-induced PMEL CD8$^+$ $T_{TE}$ cells were re-stimulated by dimeric anti-CD3 antibody (0.5 μg ml$^{-1}$) and treated with AKT inhibitor VIII (HY-10355, 1 μM), mTOR inhibitor (Rapamycin, 100 nM), or STAT6 inhibitor (AS1517499, 50 nM) in the presence or absence of Fc–IL-4 for 24 h (n = 3 biological replicates). Shown are relative Glut-1 MFI (**j**), T cell viability (**k**), CD107a MFI (**l**), and Granzyme B MFI (**m**) in the Fc–IL-4 treatment group normalized by that in the PBS group. **n**, Visualization of motif activity expression for Stat5a (MA1624.1) and Stat5b (MA1625.1) on the joint UMAP in Fig. 4i. **o**-**u**, Ex vivo-induced PMEL CD8$^+$ $T_{TE}$ cells were re-stimulated by dimeric anti-CD3 antibody (0.5 μg ml$^{-1}$) and treated with inhibitors for STAT6 (AS1517499, 50 nM) or STAT5 (Bestellnummer 573108, 25 μM) in the presence or absence of Fc–IL-4 (n = 3 biological replicates). Shown are frequency of Glut-1$^+$ among PMEL CD8$^+$ $T_{TE}$ cells (**o**), glucose uptake capacity of PMEL CD8$^+$ $T_{TE}$ cells (**p**), and relative level of basal ECAR (**q**), maximal ECAR (**r**), T cell counts (**s**), CD107a MFI (**t**), and Granzyme B MFI (**u**) in the Fc–IL-4 treatment group normalized by that in the PBS group. Data are one representative of three independent experiments. All data represent mean ± s.e.m. and are analysed by two-sided unpaired Student's t-test (**a**-**d**, and **o**), or by one-way ANOVA and Tukey's test (**e**-**m**, and **p**-**u**).

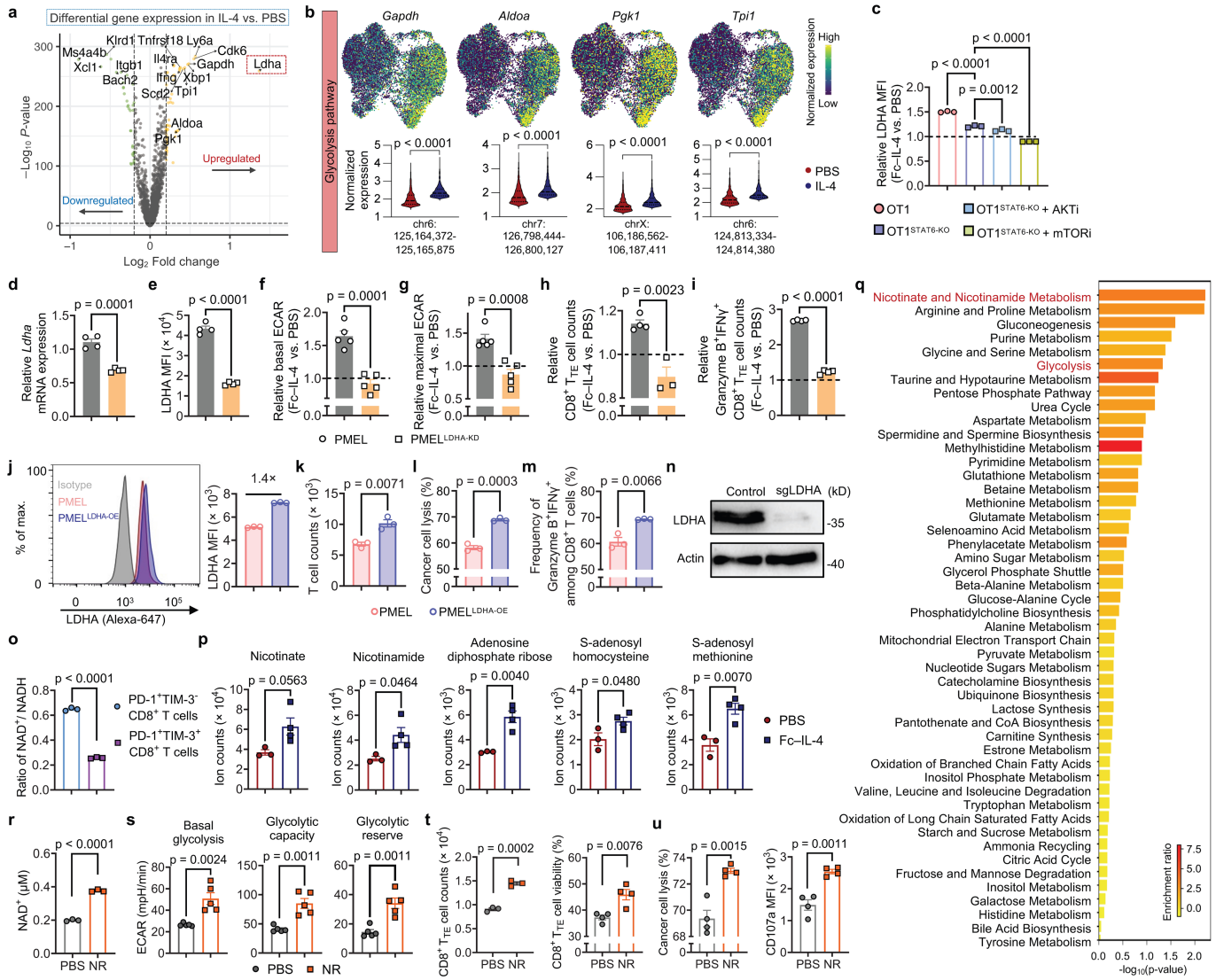


**Extended Data Fig. 10 | Fc–IL-4 reinvigorates CD8⁺ $T_{TE}$ cells by enhancing LDHA-dependent glycolysis and promoting the cellular NAD⁺ level.** **a**, **b**, Experimental setting was described in Fig. 4i. Shown is a volcano plot showing differential gene expression between IL-4 vs. PBS-treated PMEL CD8⁺ $T_{TE}$ cells (**a**), and expression of glycolysis pathway gene markers on the joint UMAP along with comparisons of corresponding accessible peaks between conditions (**b**). **c**, Relative expression of LDHA in Fc–IL-4-treated ex vivo-induced OT1 and OT1$^{STAT6\text{-}KO}$ CD8⁺ $T_{TE}$ cells (normalized by that in PBS group) with or without indicated inhibitors (n = 3 biological replicates). **d**-**i**, WT PMEL or PMEL$^{LDHA\text{-}KD}$ T cells were re-stimulated by dimeric anti-CD3 antibody (0.5 μg ml$^{-1}$) in the presence or absence of Fc–IL-4 (n = 4 biological replicates). Shown are the relative transcriptome level (**d**) and MFI of LDHA (**e**) in WT PMEL and PMEL$^{LDHA\text{-}KD}$ T cells, and the relative basal (**f**) and maximal (**g**) ECAR, and relative counts of CD8⁺ $T_{TE}$ cells (**h**) and Granzyme B⁺IFNγ⁺ polyfunctional CD8⁺ $T_{TE}$ cells (**i**) in the Fc–IL-4 treatment group normalized by that in the PBS group. **j**-**m**, WT PMEL or PMEL$^{LDHA\text{-}OE}$ T cells were co-cultured with B16F10 for 48 h (n = 3 biological replicates). Shown are representative flow cytometry plots and LDHA MFI (**j**), T cell counts (**k**), percent of cancer cell lysis (**l**), and frequencies of Granzyme B⁺IFNγ⁺ (**m**) among WT PMEL and PMEL$^{LDHA\text{-}OE}$ T cells. **n**, WB images of LDHA showing the LDHA knock-out in OT1$^{LDHA\text{-}KO}$ T cells. **o**, PD-1⁺TIM-3⁻ and PD-1⁺TIM-3⁺ PMEL T cells were sorted from ex vivo-induced PMEL T cells. The cellular level of NAD⁺ and NADH was assessed in both cell subsets. Shown is the ratio of NAD⁺ to NADH in the two cell subsets (n = 3 biological replicates). **p**, **q**, Experimental setting was described in Extended Data Fig. 7i. Shown are the cellular ion counts of metabolites engaged in nicotinate and nicotinamide metabolic pathways (**p**), and metabolic pathways enriched in Fc–IL-4 treated cells vs. PBS control group using metabolite set enrichment analysis (**q**). **r**, The cellular NAD⁺ level of ex vivo-induced CD8⁺ $T_{TE}$ cells with supplementation of a NAD⁺ precursor, nicotinamide riboside (NR) (100 μM) (n = 3 biological replicates). **s**, Ex vivo-induced CD8⁺ $T_{TE}$ cells were re-stimulated by dimeric anti-CD3 antibody (0.5 μg ml$^{-1}$) for 48 h in the presence or absence of NR (100 μM). Shown are average basal glycolysis, glycolytic capacity, and glycolytic reserve analysed from Fig. 5m (n = 5 biological replicates). **t**, Ex vivo-induced CD8⁺ $T_{TE}$ cells were re-stimulated by dimeric anti-CD3 antibody (0.5 μg ml$^{-1}$) for 48 h in the presence or absence of NR (100 μM). Shown are the counts (n = 3 biological replicates) and viability (n = 4 biological replicates) of CD8⁺ $T_{TE}$ cells. **u**, Ex vivo-induced CD8⁺ $T_{TE}$ cells were co-cultured with B16F10 tumour cells for 48 h in the presence or absence of NR (100 μM) (n = 4 biological replicates). Shown are the percent of cancer cell lysis and CD107a MFI of CD8⁺ $T_{TE}$ cells. Data are one representative of three independent experiments. All data represent mean ± s.e.m. and are analysed by two-sided unpaired Student's t-test (**b**, **d**-**m**, and **o**-**u**), or one-way ANOVA and Tukey's test (**c**).

nature portfolio

Corresponding author(s): Li Tang, Yugang Guo, and Rong Fan

Last updated by author(s): Jul 19, 2024

# Reporting Summary

Nature Portfolio wishes to improve the reproducibility of the work that we publish. This form provides structure for consistency and transparency in reporting. For further information on Nature Portfolio policies, see our Editorial Policies and the Editorial Policy Checklist.

## Statistics

For all statistical analyses, confirm that the following items are present in the figure legend, table legend, main text, or Methods section.

| n/a | Confirmed | |
|---|---|---|
| ☐ | ☒ | The exact sample size (*n*) for each experimental group/condition, given as a discrete number and unit of measurement |
| ☐ | ☒ | A statement on whether measurements were taken from distinct samples or whether the same sample was measured repeatedly |
| ☐ | ☒ | The statistical test(s) used AND whether they are one- or two-sided<br>*Only common tests should be described solely by name; describe more complex techniques in the Methods section.* |
| ☐ | ☒ | A description of all covariates tested |
| ☐ | ☒ | A description of any assumptions or corrections, such as tests of normality and adjustment for multiple comparisons |
| ☐ | ☒ | A full description of the statistical parameters including central tendency (e.g. means) or other basic estimates (e.g. regression coefficient) AND variation (e.g. standard deviation) or associated estimates of uncertainty (e.g. confidence intervals) |
| ☐ | ☒ | For null hypothesis testing, the test statistic (e.g. *F*, *t*, *r*) with confidence intervals, effect sizes, degrees of freedom and *P* value noted<br>*Give P values as exact values whenever suitable.* |
| ☒ | ☐ | For Bayesian analysis, information on the choice of priors and Markov chain Monte Carlo settings |
| ☒ | ☐ | For hierarchical and complex designs, identification of the appropriate level for tests and full reporting of outcomes |
| ☒ | ☐ | Estimates of effect sizes (e.g. Cohen's *d*, Pearson's *r*), indicating how they were calculated |

*Our web collection on statistics for biologists contains articles on many of the points above.*

## Software and code

Policy information about availability of computer code

| | |
|---|---|
| Data collection | 1. Flow cytometry data collection was performed with an Attune NxT Flow Cytometer with Attune NxT Software v.3 (Invitrogen / Thermal Fischer Scientific).<br>2. The generated gene expression libraries were sequenced using an Illumina HiSeq 4000 with a sequencing depth of 50,000 paired-end reads per cell.<br>3. The gRNAs were designed using the publicly available online gRNA design tool CRISPick (https://portals.broadinstitute.org/gppx/crispick/public).<br>4. Single-cell co-profiling of epigenomic landscape and gene expression in the same single nuclei was performed using the Chromium Next GEM Single Cell Multiome ATAC + Gene Expression kit (10×Genomics, Cat# PN-1000283).<br>5. In vivo Bioluminescence data was obtained through IVIS Spectrum In Vivo Imaging System (PerkinElmer).<br>6. Metabolomic data was collected using Agilent Quantitative analysis software (version B.07.00, MassHunter Agilent technologies). |
| Data analysis | 1. Flow cytometry data were analyzed using FlowJo (version 10.6.1,Tree Star, Oregon, USA).<br>2. Statistical analysis was performed using GraphPad Prism (version 10.1.2, GraphPad software, Inc, La Jolla, CA, USA).<br>3. The raw fastq files were generated and demultiplexed by CeleScope rna from Singleron (version 3.0.1) and primary data analysis was performed with CeleScope (version 1.10.0) using a custom reference package based on reference genome (Mus_musculus_ensembl_92). Downstream data analysis was performed with the Seurat v4 pipeline. Cells were first filtered based on two metrics: 1) the number of detected genes per cell must be between 200 to 5000; 2) the proportion of mitochondrial gene counts (UMIs from mitochondrial genes / total UMIs) must be less than 10%. Then, the gene expression data was normalized using Seurat sctransform. No major batch effects were observed between the two samples. Finally, the "SCT" data assay was reduced to two dimensions using UMAP for visualization, with 30 computed PCs as input. Differentially expressed genes (DEGs) were identified using the function "FindMarkers" for pairwise comparison between two conditions. A log fold-change threshold of 0.25 was applied to select genes as differentially expressed. The function |

"AddModuleScore" was used to calculate the module scores of each cluster based on the aggregated expression of defined gene sets.
4. Raw LC-MS/MS data was processed using the Agilent Quantitative analysis software (version B.07.00, MassHunter Agilent technologies). Relative quantification of metabolites was based on EIC (Extracted Ion Chromatogram) areas for the monitored MRM transitions. The obtained tables (containing peak areas of detected metabolites across all samples) were exported to "R" software ( version 4.2.1, http://cran.r-project.org/). Signal intensity drift correction and noise filtering was done within the MRM PROBS software. The preprocessed data with peak areas were imported into Metaboanalyst 5.0 for further data analysis.
5. Single-cell ATAC+Gene co-profiling data processing and analysis: The Cell Ranger ARC v2.0.2 (10x Genomics) was utilized to perform sample demultiplexing, barcode processing, identification of open chromatin regions, and simultaneous counting of transcripts and peak accessibility in single cells from the sequenced data. The output per barcode matrices underwent joint RNA and ATAC analysis using Signac v1.12.0 and Seurat v4. Quality filtering criteria adhered to default settings. Specifically, cells were retained if they exhibited an ATAC peak count ranging from 1,000 to 100,000, a gene count ranging from 1,000 to 25,000, a nucleosome_signal below 2, and a TSS enrichment score exceeding 1. To enhance the accuracy of peak identification, we employed MACS2 v2.2.9.1 with the "CallPeaks" function.

For manuscripts utilizing custom algorithms or software that are central to the research but not yet described in published literature, software must be made available to editors and reviewers. We strongly encourage code deposition in a community repository (e.g. GitHub). See the Nature Portfolio guidelines for submitting code & software for further information.

## Data

Policy information about availability of data

All manuscripts must include a data availability statement. This statement should provide the following information, where applicable:

- Accession codes, unique identifiers, or web links for publicly available datasets
- A description of any restrictions on data availability
- For clinical datasets or third party data, please ensure that the statement adheres to our policy

All data generated and supporting the findings of this study are available within the paper. Raw and processed single-cell sequencing data for this study can be accessed in the NCBI Gene Expression Omnibus (GEO) database under the accession number GSE259409. Additional information and materials will be made available upon reasonable request.

## Research involving human participants, their data, or biological material

Policy information about studies with human participants or human data. See also policy information about sex, gender (identity/presentation), and sexual orientation and race, ethnicity and racism.

| | |
|---|---|
| Reporting on sex and gender | Sex and/or gender was not considered in this study. |
| Reporting on race, ethnicity, or other socially relevant groupings | Race, ethnicity, or other socially relevant groupings were not considered in this study. |
| Population characteristics | Population characteristics were not considered as a variable in this study. |
| Recruitment | Primary T lymphocytes from healthy donors were provided by the Cleveland Clinic's BioRepository Core. |
| Ethics oversight | Cleveland Clinic's BioRepository Review Committee provided insight. |

Note that full information on the approval of the study protocol must also be provided in the manuscript.

# Field-specific reporting

Please select the one below that is the best fit for your research. If you are not sure, read the appropriate sections before making your selection.

☒ Life sciences ☐ Behavioural & social sciences ☐ Ecological, evolutionary & environmental sciences

For a reference copy of the document with all sections, see nature.com/documents/nr-reporting-summary-flat.pdf

# Life sciences study design

All studies must disclose on these points even when the disclosure is negative.

| | |
|---|---|
| Sample size | Group sizes for in vivo validation experiments were selected empirically based on previous results of the intra-group variation of tumor growth upon similar treatments. For in vitro experiments, group sizes were selected on the basis of previous publication and prior knowledge of variation and were replicated at least for 3 individual and independent experiments. Ref: Nat Immunol 2021 Jun; 22 (6): 746-756 |
| Data exclusions | Rout outlier tests were run with default parameters (Q = 1%) in Prism on all mouse experimental data due to inherent variability within the model system. |
| Replication | All presented results were repeatable. Replicates were used in all experiments as noted in figure legend or methods. |
| Randomization | Age and sex-matched animals were used for each experiment. Mice were randomized prior to treatment. For the experiments without mice, |

| | |
|---|---|
| Randomization | there is no randomization for samples because these in vitro experiments were observational and replicated at least for 3 individual, independent experiments. |
| Blinding | In vivo tumor engraftment and grouping was conducted randomly before treatment. Fully blinded experiments were not performed due to insufficient personnel availability to accommodate such situation and requirements for cage labeling and staffing needs. |

# Reporting for specific materials, systems and methods

We require information from authors about some types of materials, experimental systems and methods used in many studies. Here, indicate whether each material, system or method listed is relevant to your study. If you are not sure if a list item applies to your research, read the appropriate section before selecting a response.

## Materials & experimental systems

| n/a | Involved in the study |
|---|---|
| ☐ | ☒ Antibodies |
| ☐ | ☒ Eukaryotic cell lines |
| ☒ | ☐ Palaeontology and archaeology |
| ☐ | ☒ Animals and other organisms |
| ☒ | ☐ Clinical data |
| ☒ | ☐ Dual use research of concern |
| ☒ | ☐ Plants |

## Methods

| n/a | Involved in the study |
|---|---|
| ☒ | ☐ ChIP-seq |
| ☐ | ☒ Flow cytometry |
| ☒ | ☐ MRI-based neuroimaging |

## Antibodies

Antibodies used

The following antibodies or staining reagents were purchased from BioLegend:
CD16/32 (93, 101302), Thy1.1 (OX-7, 202529), Thy1.2 (30-H12, 105343), CD45.1 (A20, 110707), CD45.2 (104, 109814), CD8α (53-6.7, 100714), CD8β (YTS256.7.7, 126606), CD4 (RM4-5, 100526), NK1.1 (PK136, 108740), F4/80 (BM8,123108), CD3ε (17A2, 100306), CD19 (6D5,115520), CD44 (IM7, 103006), CD11c (N418, 117348), I-A/I-E (MHC-II, M5/114.15.2, 107643), Siglec-F (S17007L, 155508), CD80 (16-10A1, 104734), CD86 (GL-1, 105006), Foxp3 (MF-14, 126406), CD11b (M1/70, 101228), Granzyme B (GB11, 515403), IFN-γ (XMG1.2, 505826), TNF-α (MP6-XT22, 506308), IL-2 (JES6-5H4, 503822), IL-4Rα (I015F8, 144806), CD69 (H1.2F3, 104512), Gr-1 (RB6-8C5, 108423), CD107a (1D4B, 121626), CD95 (SA367H8, 152608), CD178 (MFL3, 106605), PD-1 (29F.1A12, 135216), TIM-3 (RMT3-23, 119706), TIM-3 (RMT3-23, 119737), HRP-Actin (2F1-1, 643808), GATA3 (16E10A23, 653805), Tbet (4B10, 644827), anti-rabbit IgG (minimal x-reactivity) Antibody (Poly4064, 406414), anti-mouse IgG1 Antibody (RMG1-1, 406617), STAT6 (16G12A08, 657902), Zombie Aqua™ Fixable Viability Kit (423102), human CD3 (OKT3, 317306), human CD4 (OKT4, 317416), human CD8 (SK1, 344724), human IFN-γ (B27, 506516), and human TNF-α (MAb11, 502940).

The following antibodies or staining reagents were purchased from BD Biosciences:
Anti-TCF-7/TCF-1(S33-966, 566693), anti-phospho-Akt (pT308) (J1-223.371, 558275), anti- phospho-Akt (pS473) (M89-61, 560404), anti-Akt (7/Akt/PKBα, 610836), anti-active Caspase-3 (C92-605.rMAb, 570334)

The following antibodies or staining reagents were purchased from BioXcell:
Anti-CD8 (YTS 169.4, BE0117), anti-CD4 (YTS 177, BE0288), anti-NK1.1 (PK136, BP0036), anti-Ly6G (NIMP-R14, BE0320), anti-lgG (LTF-2, BP0090) and anti-IL-4 (11B11, BE0045), anti-mouse CD3 (17A2, BE0002), anti-mouse CD28 (PV-1, BE0015-5), anti-mouse PD-1 (RMP1-14, BE0146), and anti-mouse CTLA-4 (9H10, BE0131)

The following antibodies or staining reagents were purchased from Invitrogen:
Goat anti-Rat IgG Fc Secondary Antibody (31226) and eBioscience™ Cell Stimulation Cocktail (00-4970-03), and anti-phospho-STAT6 (Tyr641) (46H1L12, 700247)

The following antibodies or staining reagents were purchased from Cell Signaling Technology: Anti-rabbit HRP-IgG (7074), and anti-Glut-1 (73015)

The following antibodies or staining reagents were purchased from Proteintech: Anti-P70S6K (14485-1-AP), Anti-LDHA (19987-1-AP)

The following antibodies or staining reagents were purchased from Antibodies: Anti-phospho-P70S6K (pThr389) (ABIN7265266)

The following antibodies or staining reagents were purchased from ACRO Biosystems: Anti-FMC63 scFv (CAR19) (FM3-HPY53)

Antibodies for surface staining were used at a 1:100 dilution, for intracellular staining at a 1:50 dilution, and for WB at a 1:1000 staining.

Validation

For antibodies used in flow cytometry, each antibody has been validated by the manufacturer for use to detect mouse or human species targets. These antibodies are further validated and routinely used in our lab with good reproducibility. Detailed validation information for each antibody is available at the following websites:

1. CD16/32 (93, 101302), https://www.biolegend.com/en-us/products/purified-anti-mouse-cd16-32-antibody-190
2. Thy1.1 (OX-7, 202529), https://www.biolegend.com/en-us/products/brilliant-violet-421-anti-rat-cd90-mouse-cd90-1-thy-1-1-antibody-7307
3. Thy1.2 (30-H12, 105343), https://www.biolegend.com/en-us/products/brilliant-violet-605-anti-mouse-cd90-2-thy1-2-

antibody-13864
4. CD45.1 (A20, 110707), https://www.biolegend.com/en-ie/products/pe-anti-mouse-cd45-1-antibody-199?GroupID=BLG1933
5. CD45.2 (104, 109814), https://www.biolegend.com/en-ie/products/apc-anti-mouse-cd45-2-antibody-2759
6. CD8α (53-6.7, 100714), https://www.biolegend.com/en-ie/products/apc-cyanine7-anti-mouse-cd8a-antibody-2269
7. CD8β (YTS256.7.7, 126606), https://www.biolegend.com/en-ie/products/fitc-anti-mouse-cd8b-antibody-4475
8. CD4 (RM4-5, 100526), https://www.biolegend.com/en-ie/products/apc-cyanine7-anti-mouse-cd4-antibody-1937
9. NK1.1 (PK136, 108740), https://www.biolegend.com/en-ie/products/brilliant-violet-605-anti-mouse-nk-1-1-antibody-8665
10. F4/80 (BM8,123108), https://www.biolegend.com/en-ie/products/fitc-anti-mouse-f4-80-antibody-4067
11. CD3ε (17A2, 100306), https://www.biolegend.com/en-ie/products/fitc-anti-mouse-cd3epsilon-antibody-23
12. CD19 (6D5,115520), https://www.biolegend.com/en-ie/products/pe-cyanine7-anti-mouse-cd19-antibody-1907
13. CD44 (IM7, 103006), https://www.biolegend.com/en-ie/products/fitc-anti-mouse-human-cd44-antibody-314
14.CD11c (N418, 117348), https://www.biolegend.com/en-ie/products/pe-dazzle-594-anti-mouse-cd11c-antibody-9846
15. I-A/I-E (MHC-II, M5/114.15.2, 107643), https://www.biolegend.com/en-ie/products/brilliant-violet-711-anti-mouse-i-a-i-e-antibody-12086
16. Siglec-F (S17007L, 155508), https://www.biolegend.com/en-ie/products/apc-anti-mouse-cd170-siglec-f-antibody-16373
17. CD80 (16-10A1, 104734), https://www.biolegend.com/en-ie/products/pe-cyanine7-anti-mouse-cd80-antibody-9320
18. CD86 (GL-1, 105006), https://www.biolegend.com/en-ie/products/fitc-anti-mouse-cd86-antibody-254
19. Foxp3 (MF-14, 126406), https://www.biolegend.com/en-ie/products/alexa-fluor-488-anti-mouse-foxp3-antibody-4661
20. CD11b (M1/70, 101228), https://www.biolegend.com/en-ie/products/percp-cyanine5-5-anti-mouse-human-cd11b-antibody-4257
21. Granzyme B (GB11, 515403), https://www.biolegend.com/en-ie/products/fitc-anti-human-mouse-granzyme-b-antibody-6066
22. IFN-γ (XMG1.2, 505826), https://www.biolegend.com/en-ie/products/pe-cyanine7-anti-mouse-ifn-gamma-antibody-5865
23. TNF-α (MP6-XT22, 506308), https://www.biolegend.com/en-ie/products/apc-anti-mouse-tnf-alpha-antibody-975
24. IL-2 (JES6-5H4, 503822), https://www.biolegend.com/en-ie/products/percp-cyanine5-5-anti-mouse-il-2-antibody-4441
25. IL-4Rα (I015F8, 144806), https://www.biolegend.com/en-ie/products/pe-cyanine7-anti-mouse-cd124-il-4ralpha-11769
26. CD69 (H1.2F3, 104512), https://www.biolegend.com/en-ie/products/pe-cyanine7-anti-mouse-cd69-antibody-3168
27. Gr-1 (RB6-8C5, 108423), https://www.biolegend.com/en-ie/products/apc-cyanine7-anti-mouse-ly-6gly-6c-gr-1-antibody-3935
28. CD107a (1D4B, 121626), https://www.biolegend.com/en-ie/products/percp-cyanine5-5-anti-mouse-cd107a-lamp-1-antibody-13079
29. CD95 (SA367H8, 152608), https://www.biolegend.com/en-ie/products/pe-anti-mouse-cd95-fas-antibody-13907
30. CD178 (MFL3, 106605), https://www.biolegend.com/en-ie/products/pe-anti-mouse-cd178-fasl-antibody-391
31. PD-1 (29F.1A12, 135216), https://www.biolegend.com/en-ie/products/pe-cyanine7-anti-mouse-cd279-pd-1-antibody-7005
32. TIM-3 (RMT3-23, 119706), https://www.biolegend.com/en-ie/products/apc-anti-mouse-cd366-tim-3-antibody-8238
33. TIM-3 (RMT3-23, 119737), https://www.biolegend.com/en-ie/products/apcfire-750-anti-mouse-cd366-tim-3-antibody-17871
34. HRP-Actin (2F1-1, 643808), https://www.biolegend.com/en-ie/products/direct-blot-hrp-anti-beta-actin-antibody-12776
35. GATA3 (16E10A23, 653805), https://www.biolegend.com/en-ie/products/apc-anti-gata3-antibody-9104
36. Tbet (4B10, 644827), https://www.biolegend.com/en-ie/products/pe-dazzle-594-anti-t-bet-antibody-11891
37. anti-rabbit IgG (minimal x-reactivity) Antibody (Poly4064, 406414), https://www.biolegend.com/en-ie/products/alexa-fluor-647-donkey-anti-rabbit-igg-minimal-x-reactivity-9379
38. anti-mouse IgG1 Antibody (RMG1-1, 406617), https://www.biolegend.com/en-ie/products/alexa-fluor-647-anti-mouse-igg1-9685
39. STAT6 (16G12A08, 657902), https://www.biolegend.com/en-ie/products/purified-anti-stat6-antibody-9066
40. Zombie Aqua™ Fixable Viability Kit (423102), https://www.biolegend.com/en-ie/products/zombie-aqua-fixable-viability-kit-8444
41. human CD3 (OKT3, 317306), https://www.biolegend.com/en-ie/products/fitc-anti-human-cd3-antibody-3644
42. human CD4 (OKT4, 317416),https://www.biolegend.com/en-us/products/apc-anti-human-cd4-antibody-3657
43. human CD8 (SK1, 344724), https://www.biolegend.com/en-us/products/alexa-fluor-700-anti-human-cd8-antibody-9062
44. human IFN-γ (B27, 506516), https://www.biolegend.com/en-us/products/alexa-fluor-700-anti-human-ifn-gamma-antibody-3445
45. human TNF-α (MAb11, 502940),https://www.biolegend.com/en-us/products/brilliant-violet-711-anti-human-tnf-alpha-antibody-9034

Anti-mouse CD3 (17A2, BE0002) and anti-mouse CD28 (PV-1, BE0015-5) were used to stimulate the proliferation and cytokine production of mouse T cells. Detailed validation information for each antibody is available at the following sites:
1. Anti-mouse CD3 (17A2, BE0002), https://bioxcell.com/invivomab-anti-mouse-cd3-be0002
2. anti-mouse CD28 (PV-1, BE0015-5), https://bioxcell.com/invivomab-anti-mouse-cd28-be0015-5

Anti-CD8 (YTS 169.4, BE0117), anti-CD4 (YTS 177, BE0288), anti-NK1.1 (PK136, BP0036), anti-Ly6G (NIMP-R14, BE0320), anti-lgG (LTF-2, BP0090) and anti-IL-4 (11B11, BE0045), anti-mouse PD1 (RMP1-14, BE0146), and anti-mouse CTLA4 (9H10, BE0131) were used in vivo to deplete corresponding cells or blockade signals. Detailed validation information for each antibody is available at the following sites:
1. Anti-CD8 (YTS 169.4, BE0117), https://bioxcell.com/invivomab-anti-mouse-cd8-alpha-be0117
2. anti-CD4 (YTS 177, BE0288), https://bioxcell.com/invivomab-anti-human-cd4-be0288
3. anti-NK1.1 (PK136, BP0036), https://bioxcell.com/invivoplus-anti-mouse-nk1-1-bp0036
4. anti-Ly6G (NIMP-R14, BE0320), https://bioxcell.com/invivomab-anti-mouse-ly6g-ly6c-be0320
5. anti-lgG (LTF-2, BP0090), https://bioxcell.com/invivoplus-rat-igg2b-isotype-control-anti-keyhole-limpet-hemocyanin
6. anti-IL-4 (11B11, BE0045), https://bioxcell.com/invivomab-anti-mouse-il-4-be0045
7. anti-mouse PD1 (RMP1-14, BE0146), https://bioxcell.com/invivomab-anti-mouse-pd-1-cd279-be0146
8. anti-mouse CTLA4 (9H10, BE0131), https://bioxcell.com/invivomab-anti-mouse-ctla-4-cd152-be0131

Anti-phospho-STAT6 (Tyr641) (46H1L12, 700247), anti-Glut-1 (73015) , Anti-P70S6K (14485-1-AP), Anti-LDHA (19987-1-AP) , and Anti-phospho-P70S6K (pThr389) (ABIN7265266) were used for WB. Detailed validation information for each antibody is available at the following sites:
1. Anti-phospho-STAT6 (Tyr641) (46H1L12, 700247), https://www.thermofisher.com/antibody/product/Phospho-STAT6-Tyr641-Antibody-clone-46H1L12-Recombinant-Monoclonal/700247
2. anti-Glut-1 (73015) , https://www.cellsignal.com/products/primary-antibodies/glut1-e4s6i-rabbit-mab/73015
3. Anti-P70S6K (14485-1-AP), https://www.ptglab.com/products/p70(S6K)-Antibody-14485-1-AP.htm
4. Anti-LDHA (19987-1-AP) , https://www.ptglab.com/products/LDHA-Specific-Antibody-19987-1-AP.htm

5. Anti-phospho-P70S6K (pThr389) (ABIN7265266), https://www.biocompare.com/Search-Antibodies/?search=ABIN7265266

## Eukaryotic cell lines

Policy information about cell lines and Sex and Gender in Research

| | |
|---|---|
| Cell line source(s) | B16F10, YUMM1.7 melanoma cells, Raji lymphoma cells, MC38 colon cancer cells,Nalm6 cells, CTLL-2 cells, K562 cells, HEK293T cells, and Phoenix-Eco cells were originally purchased from the American Type Culture Collection. OVA-transduced B16F10 (B16F10-OVA) mouse melanoma cell lines were provided by Prof. Darell J. Irvine (Massachusetts Institute of Technology). gp33-transduced B16F10 (B16F10-gp33) and OVA-transduced YUMM1.7 (YUMM1.7-OVA) mouse melanoma cell lines were provided by Werner Held (University of Lausanne). HER2-transduced MC38 mouse colon cancer cell lines (MC38-HER2) were provided by Prof. Pedro Romero (University of Lausanne). Luciferase positive Nalm6 cell lines (Nalm6-Luciferase) were provided by Prof. Sidi Chen (Yale University). |
| Authentication | None of the cell lines were authenticated in these studies. In all related studies, cell lines with low passage number were used. |
| Mycoplasma contamination | All cell lines were confirmed mycoplasma negative. |
| Commonly misidentified lines (See ICLAC register) | No commonly misidentified cell lines were used. |

## Animals and other research organisms

Policy information about studies involving animals; ARRIVE guidelines recommended for reporting animal research, and Sex and Gender in Research

| | |
|---|---|
| Laboratory animals | Six-to-eight-week-old female CD45.2+Thy1.2+ C57BL/6 (C57BL/6J) mice, CD45.1+ mice (B6.SJL-Ptprca Pepcb/BoyCrl), and NOD.Cg-Prkdcscid Il2rgtm1Wjl/SzJ (NSG) mice were purchased from Charles River Laboratories (Lyon, France). CD45.1+CD45.2+ mice were generated by crossing CD45.1+ mice with CD45.2+ C57BL/6 mice. TCR-transgenic Thy1.1+ pmel-1 (PMEL) mice (B6.Cg-Thy1a/Cy Tg(TcraTcrb)8Rest/J) and TCR-transgenic OT-I mice (C57BL/6-Tg(TcraTcrb)1100Mjb/J), CD45.2+ background Rosa26-Cas9 knock-in mice (B6J.129(Cg)-Gt(ROSA)26Sortm1.1(CAG-cas9*,-EGFP)Fezh/J) were originally purchased from the Jackson Laboratory and maintained at the EPFL's pathogen-free facility. OT1 mice were crossed with CD45.1+ mice to generate CD45.1+ OT1 mice. CRISPR–Cas9 knock-in CD45.2+ mice were crossed with CD45.1+ OT1 mice to generate CRISPR–Cas9 knock-in OT1 TCR-transgenic mice. Tcf7DTR-GFP P14 mice on a CD45.2 background were generated as described before (Ref: Immunity. 2019 Jan 15;50(1):195-211). All mice were housed in the EPFL Center of PhenoGenomics or a conventional animal facility of the University of Lausanne and were kept in individually ventilated cages, at 19-23 °C, with 45-65% humidity, and with a 12 h dark/light cycle. |
| Wild animals | Study did not involve wild animals. |
| Reporting on sex | Sex is not relevant in this study, and most animals used were female mice. |
| Field-collected samples | Study did not involve field-collected samples. |
| Ethics oversight | Experimental procedures in mouse studies were approved by the Swiss authorities (Canton of Vaud, animal protocol IDs VD3206, VD3533, VD3902, VD3912, VD3915, and VD3040x2d) and performed in accordance with the guidelines from the Center of PhenoGenomics of the EPFL and the animal facility of the University of Lausanne. Mice were euthanized when body weight loss was beyond 15%, or the tumor area reached 150 mm2 (as a predetermined endpoint), or other ending points reach the requirements of the animal licenses. |

Note that full information on the approval of the study protocol must also be provided in the manuscript.

## Plants

| | |
|---|---|
| Seed stocks | Plants or seed stocks were not used in this study. |
| Novel plant genotypes | Plant genotypes are not relevant in this study |
| Authentication | Plant authentication is not performed in this study |

# Flow Cytometry

## Plots

Confirm that:

☒ The axis labels state the marker and fluorochrome used (e.g. CD4-FITC).

☒ The axis scales are clearly visible. Include numbers along axes only for bottom left plot of group (a 'group' is an analysis of identical markers).

☒ All plots are contour plots with outliers or pseudocolor plots.

☒ A numerical value for number of cells or percentage (with statistics) is provided.

## Methodology

| | |
|---|---|
| Sample preparation | Tumors were collected, weighed, mechanically minced, and stirred at 1,000 r.p.m. in RPMI-1640 medium with collagenase Type IV (1 mg ml−1, Thermo Fisher Scientific), dispase 2 (100 μg ml−1, Sigma-Aldrich), hyaluronidase (100 μg ml−1, Sigma-Aldrich) and DNase I (100 μg ml−1, Sigma-Aldrich) for 60 min at 37 °C for digestion. Red blood cells (RBC) in the digested tumor samples were lysed with ACK lysing buffer for 3 min at room temperature. Tumor-infiltrating leukocytes were then enriched by density gradient centrifugation against Percoll (GE Healthcare), resuspended in PBS with BSA albumin (0.2%, wt/v, Sigma-Aldrich), stained with indicated antibodies, and analyzed with flow cytometry. Similarly, spleens and lymph nodes were collected and mechanically minced through strainers (70 μm) and then RBC inside were lysed with ACK lysing buffer for 5 min at room temperature before antibody staining and flow cytometry analysis. Blood samples were collected and resuspended immediately in the EDTA-PBS buffer (10 mM, EDTA) and RBC inside were lysed with ACK lysing buffer for 5 min at room temperature and then the leukocytes were enriched by density gradient centrifugation against Percoll (GE Healthcare) as above. Bones were crushed in EDTA-PBS buffer (10 mM, EDTA) and the bone marrow cells were collected after filtering through the strainer, remaining RBC was lysed with ACK lysing buffer as above. |
| Instrument | Data was collected using Attune NxT Flow Cytometer (Invitrogen / Thermal Fischer Scientific). T cell sorting was performed with FACS Aria II (BD Biosciences) or SH800S Cell Sorter (SONY). |
| Software | Flow cytometry data were analyzed using FlowJo 10.6.1 (Tree Star, Oregon, USA). Flow cytometry data collection was performed using Attune NxT Software version 3 (Invitrogen / Thermal Fischer Scientific). |
| Cell population abundance | For a typical analysis, >50k leukocytes were collected for further gating. Purity was determined by flow cytometry for PD1+TIM-3+ T cells (> 95%) and CAR-T cells (> 95%). |
| Gating strategy | We used standard gating strategies: gating on the typical lymphocyte population based on FSC-SSC signals, doublet exclusion based on FSC-H and FSC-A comparison, Live / Dead discrimination based on DAPI or fixable Aqua dye signals. Cell populations were identified based on the expression markers listed below. CD4 T cells: CD45+/CD3+/CD4+; CD8 T cells: CD45+/CD3+/CD8+; Tregs: CD45+/CD3+/CD4+/FoxP3+; B cells: CD45+/CD3-/CD19+; NK cells: CD45+/CD3-/NK1.1+; DC: CD45+/Gr-1-/CD11b+/CD11c+/MHCII+; Tumor-associated macrophages: CD45+/Gr-1-/CD11b+/F4/80+/MHCII+; MDSC: CD45+/Gr-1+/CD11b+; Eosinophils: CD45+/CD11b+/Siglec-F+. |

☒ Tick this box to confirm that a figure exemplifying the gating strategy is provided in the Supplementary Information.